Air-sea Interaction at Contrasting Sites in the Eastern Tropical Pacific: mesoscale variability and atmospheric convection at 10°N

by

J. Thomas Farrar

B.S., Physics and B.A., Philosophy, 2000
The University of Oklahoma
S.M., Physical Oceanography, 2003
The Massachusetts Institute of Technology and the Woods Hole Oceanographic Institution

Submitted in partial fulfillment of the requirements for the degree of
Doctor of Philosophy
at the
MASSACHUSETTS INSTITUTE OF TECHNOLOGY
and the
WOODS HOLE OCEANOGRAPHIC INSTITUTION
February 2007

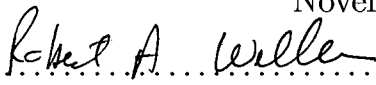Author .... *[signature]* ....
Joint Program in Oceanography/Applied Ocean Science and Engineering
Massachusetts Institute of Technology
Woods Hole Oceanographic Institution
November 15, 2006

Certified by .... *[signature]* ....
Robert Weller
Senior Scientist, Woods Hole Oceanographic Institution
Thesis Supervisor

Accepted by .... *[signature]* ....
Carl Wunsch
Chairman, Joint Committee for Physical Oceanography
Massachusetts Institute of Technology
Woods Hole Oceanographic Institution

Air-sea Interaction at Contrasting Sites in the Eastern Tropical Pacific: mesoscale variability and atmospheric convection at 10°N

by

J. Thomas Farrar

Abstract

The role of ocean dynamics in driving air-sea interaction is examined at two contrasting sites on 125°W in the eastern tropical Pacific Ocean using data from the Pan American Climate Study (PACS) field program. Analysis based on the PACS data set and satellite observations of sea surface temperature (SST) reveals marked differences in the role of ocean dynamics in modulating SST. At a near-equatorial site (3°S), the 1997-1998 El Niño event dominated the evolution of SST and surface heat fluxes, and it is found that wind-driven southward Ekman transport was important in the local transition from El Niño to La Niña conditions. At a 10°N site near the summertime position of the Inter-tropical Convergence Zone, oceanic mesoscale motions played an important role in modulating SST at intraseasonal (50- to 100-day) timescales, and the buoy observations suggest that there are variations in surface solar radiation coupled to these mesoscale SST variations. This suggests that the mesoscale oceanic variability may influence the occurrence of clouds.

The intraseasonal variability in currents, sea surface height, and SST at the northern site is examined within the broader spatial and temporal context afforded by satellite data. The oscillations have zonal wavelengths of 550-1650 km and propagate westward in a manner consistent with the dispersion relation for first baroclinic mode, free Rossby waves in the presence of a mean westward flow. The hypothesis that the intraseasonal variability and its annual cycle are associated with baroclinic instability of the North Equatorial Current is supported by a spatio-temporal correlation between the amplitude of intraseasonal variability and the occurrence of westward zonal flows meeting an approximate necessary condition for baroclinic instability.

Focusing on 10°N in the eastern tropical Pacific, the hypothesis that mesoscale oceanic SST variability can systematically influence cloud properties is investigated using several satellite data products. A statistically significant relationship between SST and columnar cloud liquid water (CLW), cloud reflectivity, and surface solar radiation is identified within the wavenumber-frequency band corresponding to oceanic Rossby waves. Analysis of seven years of CLW data and 20 years surface solar radiation data indicates that 10-20% of the variance of these cloud-related properties at intraseasonal periods and wavelengths on the order of 10° longitude can be ascribed to SST signals driven by oceanic Rossby waves.

Thesis Supervisor: Robert Weller
Title: Senior Scientist, Woods Hole Oceanographic Institution

Acknowledgments

Most importantly, I would like to express my gratitude to my wife, Shelly, for her support, patience, and good humor during my graduate studies. Shelly's presence in my life has played an immeasurable role in my academic success and general well-being.

My parents, John and Ann, have done a great deal to instill in me the qualities that have allowed me to complete this research. Now that Shelly and I have our own son, John Oliver, I appreciate the efforts of my parents more than ever, and I hope that Shelly and I can do as well for John as my parents have done for me.

My advisor, Bob Weller, is a very busy scientist, but he has never been too busy to offer guidance when I have needed it. I feel lucky to have had the opportunity to have learned from Bob about the many important aspects of doing science, and I appreciate the special efforts he has made in this respect.

When fellow oceanographers ask who is on my thesis committee and I answer "Raf Ferrari, Jim Price, and John Toole", I am invariably told something to the effect of "Well, that's a good group". They certainly are a good group, and I feel very fortunate to have had the chance to interact with each of them. Besides being knowledgable scientists, each one is a kind person that I look up to. I am pleased to have received their advice on my research, but I am equally pleased to have been able to learn from them ways of talking about and conducting scientific research.

I am grateful to the many scientists and students at WHOI and MIT who gave me valuable input during the course of this work.

Contents

Chapter 1

Introduction

1.1 Motivation

There are fundamental differences in the way the ocean and atmosphere influence one another. The ocean responds strongly to the atmospheric temperature, humidity, and winds at the surface, and the amount radiation impinging on the ocean surface depends strongly on clouds as well as water vapor and other aerosols. In contrast, the atmosphere responds primarily to the ocean's sea surface temperature (SST) field, which together with the atmosphere's surface properties, controls the flux of heat and water vapor across the sea surface.

There is also a marked contrast in adjustment timescales of the ocean and atmosphere. In part because of the relatively large heat capacity and slow currents in the ocean, SST anomalies tend to evolve slowly in comparison to atmospheric temperature anomalies and can persist for months. Thus, understanding the processes that cause variations in SST is a high priority for those wishing to understand and simulate the evolution of the atmosphere at seasonal to climate timescales.

Air-sea interaction at large scales in the tropical Pacific has received a great deal of attention in the last several decades. The tropical oceans are recognized as an important component in setting the large scale atmospheric circulation. Solar heating of the ocean is maximal near the equator, and a substantial portion of this heat is transferred from the ocean to the atmosphere through latent, sensible, and longwave heat fluxes. The ascent of warm, moist surface air results in atmospheric deep convection in the Inter-tropical Convergence Zone (ITCZ) and constitutes a key part of the large scale meridional circulation in the

atmosphere. In addition, the zonal gradient of SST in the equatorial Pacific Ocean, because of its role in setting the basin scale atmospheric pressure gradient, is important to the maintenance of the trade winds. It is widely appreciated that fairly modest changes in tropical SST can lead to dramatic, planetary scale shifts in weather and the atmospheric circulation. El Niño, which is characterized by an anomalous warming of the upper ocean of the eastern equatorial Pacific, is associated with a virtual shut-down of the trade winds and has profound impacts on global weather patterns.

Air-sea interaction at the oceanic mesoscale is less well understood, but there has been much recent interest, partly as a result of satellite platforms that allow the long-term, high-resolution measurements required to adequately sample the oceanic mesoscale motions that occur on timescales of months and spatial scales on the order of 100 km. Since early observations of mesoscale SST variability from space (e.g., Stumpf and Legeckis, 1977), it is now widely appreciated that SST signals and air-sea interaction at the oceanic mesoscale occur worldwide (e.g., Hill et al., 2000; Leeuwneburgh and Stammer, 2001; Xie, 2004; Small et al., 2005). Although satellite observations have been important in the realization of the global extent of oceanic mesoscale SST variability and associated air-sea interaction, in situ observations, though limited in time and space, have been instrumental in demonstrating that the air-sea interactions observed from satellites are not artifacts of the remote measurement techniques. For example, the identification of a relationship between the SST signal of tropical instability waves and surface wind speed in buoy data (Hayes et al., 1989) lent confidence to subsequent studies of this relationship using satellite data.

The sea surface temperature field in the eastern tropical Pacific, with its strong asymmetry about the equator, energetic variability spanning weekly to interannual timescales, and links to climate is of great interest to those working to understand coupled ocean-atmosphere variability and the role of the tropical ocean in weather and climate variability. The eastern tropical Pacific is a prolific region of tropical cyclone generation, and recent studies suggest that the tropical Pacific SST distribution plays a crucial role in global climate anomalies (Cane, 1998; Shukla, 1998). The major oceanic and atmospheric circulations in the eastern tropical Pacific are strongly interdependent and are linked through the SST field. The strong meridional temperature gradient in the region spanning the eastern Pacific warm pool and the equatorial cold tongue is believed to influence the strength and location of the ITCZ (Lindzen and Nigam, 1987), and variability in the ITCZ may in turn influence the location

of the jet stream and precipitation over North America (Montroy, 1997). At the same time, the surface winds convergent on the ITCZ create an upwelling favorable wind stress pattern that exerts considerable influence on the strength and location of the North Equatorial Current/North Equatorial Counter Current current system (Kessler, 2002).

Our understanding of the processes that control SST in the eastern tropical Pacific is lacking due to sparse and incomplete observations, to uncertainties in identifying the relative roles of the various air-sea interaction and upper ocean processes, and to large errors in existing climatologies and gridded re-analyses of the surface heat flux, wind stress, and precipitation that might be used to drive ocean models. An important goal of field programs in the eastern tropical Pacific such as the Pan American Climate Study, the Eastern Pacific Investigation of Climate experiment, and the Tropical Atmosphere Ocean mooring array is to improve understanding of the processes that govern the evolution of SST with the ultimate goal of improving skill in prediction of the local and remote atmospheric variability driven by the SST field. Thus, there is strong motivation for understanding how ocean dynamics and ocean-atmosphere interactions and heat exchange work together to set the SST field in the eastern tropical Pacific. Of particular interest is identification and understanding of systematic relationships between SST, surface heat flux, and ocean dynamics.

The overarching goal of the Pan American Climate Study (PACS) cooperative field campaign has been to gain understanding of the relationship between SST variability in the tropical oceans and the climate of the American continents in order to improve the skill of seasonal-to-interannual climate forecasts. A thorough understanding of the processes governing SST evolution in the region requires an account of the relative roles of local surface heat flux, freshwater flux, turbulent heat flux, and advection in determining SST and understanding of how and why these factors vary through time.

As part of the PACS field program, two moorings were deployed on 125°W in the eastern tropical Pacific from May, 1997 to September, 1998 (Figure 1-1). One was placed at 10°N in the eastern Pacific warm pool, near the northernmost climatological location of the ITCZ. The other mooring was placed at 3°S in the Equatorial Cold Tongue. The primary goal of the PACS mooring deployment was to improve understanding of the processes that govern the evolution of sea surface temperature at two contrasting sites in the eastern tropical Pacific Ocean. The mooring time series have high vertical and temporal resolution of upper ocean temperature, salinity, and velocity and thus provide a unique opportunity to examine air-sea
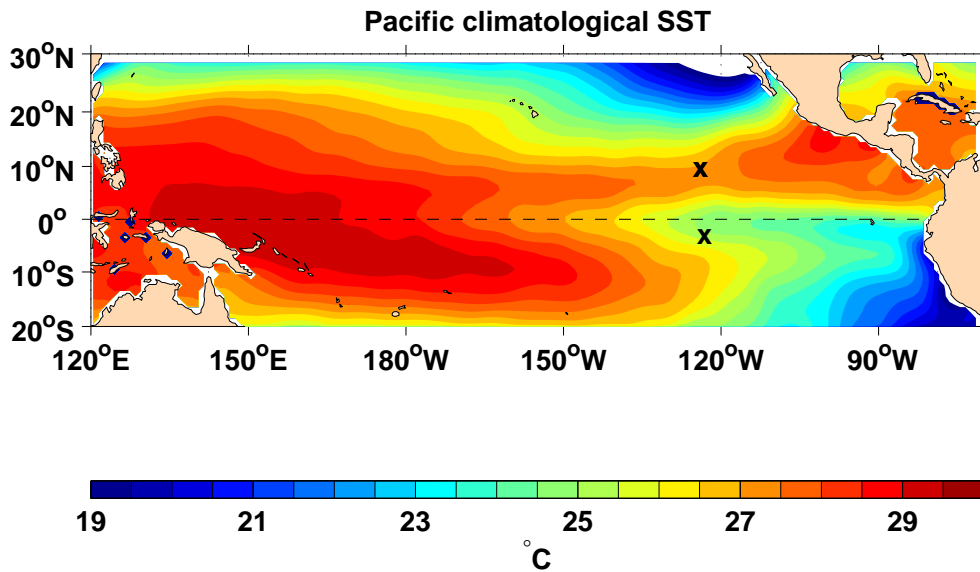
Figure 1-1: The locations of the two PACS moorings. (Each mooring is indicated by an 'x'.) The climatological mean SST is also shown (Levitus and Boyer, 1994).

interaction and other processes that govern the evolution of the upper ocean.

1.2   Thesis overview and driving questions

This thesis uses data from the PACS moorings and satellite data to understand the relative importance of surface heat flux and ocean dynamics in setting SST during 1997-1998 and to examine the role of ocean dynamics in driving air-sea interaction. An initial goal in this thesis was to quantify the relative roles of surface heat fluxes, horizontal advection, and vertical mixing processes in setting SST at two contrasting sites in the eastern tropical Pacific using the high-quality PACS mooring data. The results of this initial effort led to further questions with interesting implications. The research path followed in this thesis is perhaps most clearly understood when the motivating questions are presented alongside with the results of the research motivated by those questions:

1. **What are the relative roles of surface heat fluxes, horizontal advection, and vertical mixing processes in setting SST at the two PACS mooring sites? (Chapter 3)**

At the southern site (near 3°S, 125°W), the evolution of SST and surface heat flux was dominated by a strong El Niño event. The El Niño event of 1997-1998 was, by some measures, the strongest one ever recorded (McPhadden, 1999), and it is unquestionably the most intensively studied El Niño event. The upper-ocean temperature balance at the southern site allows some new insight into the role of wind-driven currents in the local establishment of the equatorial cold tongue at an off-equatorial site during the transition from El Niño to La Niña.

At the northern site (near 10°N, 125°W), the largest signal in the rate of change of SST at timescales longer than a few weeks was associated with quasi-periodic mesoscale motions at intraseasonal periods (∼40-100 days), and the temperature balance analysis suggested that the SST signal driven by these mesoscale motions may systematically affect air-sea heat exchange and atmospheric convection. While the buoy measurements of SST and solar radiation were suggestive of a causal relationship, the 17-month time-series from the mooring contained only a few cycles of the intraseasonal signal in velocity, SST, and heat flux. The questions below were prompted by closer examination of the strong intraseasonal variations in meridional velocity, SST, and surface solar radiation in this region, where few well-resolved in situ time series have been collected.

2. **What is the dynamical nature of the quasi-periodic intraseasonal velocity signal observed at the 10°N site? (Chapter 4)**

The wavelike signal observed at the mooring site propagated westward and had a wavelength of about 550 km. Analysis of intraseasonal velocity variability on 10°N in the broader spatial and temporal context afforded by satellite observations of sea surface height indicated that similar variability is characteristic of the region. The variability has previously been investigated from several different perspectives, and several distinct hypotheses have been put forward for its existence. This motivated a comprehensive study of the intraseasonal variability and an effort to resolve some of the contradictions between earlier studies.

The analysis shows that the intraseasonal variability tends to be strongest in the first part of each year, but its amplitude varies interannually. The intraseasonal velocity variability can be interpreted as being due to first baroclinic-mode Rossby waves under the influence of Doppler shifting by the mean westward flow. There is some evidence that baroclinic instability of the North Equatorial Current contributes energy to these westward-propagating

mesoscale disturbances, though the disturbances often appear to originate from the coastal regions near the Gulfs of Tehuantepec and Papagayo.

3. **The buoy observations at the northern site further indicate that there is variability in solar radiation coupled to the mesoscale intraseasonal SST signal, which suggests that the oceanic mesoscale signal may modulate atmospheric convection. Is there a systematic relationship between the SST expression of these mesoscale motions and atmospheric convection? (Chapter 5)**

Yes, there is a systematic relationship between mesoscale SST fluctuations within the Rossby wave band and some properties of clouds. Cross-spectral analysis of SST against satellite estimates of cloud liquid water and surface solar radiation indicates a statistically significant relationship at the wavelengths and periods corresponding to oceanic Rossby waves (identified in addressing Question 2). Analysis of seven years of CLW data and 20 years of surface solar radiation data indicates that 10-20% of the variance of these cloud-related properties at intraseasonal periods and wavelengths on the order of $10°$ longitude can be ascribed to SST signals driven by oceanic Rossby waves.

A relationship between cloud properties and mesoscale SST variations has been previously noted in the time-mean fields in the Agulhas Return Current region (near $45°$S; O'Neill et al., 2005) and in association with tropical instability waves (Deser et al., 1993; Hashizume et al., 2001). This analysis extends those results by examining the relationship in wavenumber-frequency space, showing a broadband relationship (as opposed to a narrowband relationship associated with a particular wave or the time mean). In addition, this work shows that a common and widespread phenomenon, Rossby waves acting on a meridional SST gradient, can affect atmospheric convection. This study is also carried out in one of the worlds most active and important convective regions, and some work is done to show how mesoscale variability in SST (more precisely, variability in surface heat and moisture fluxes) can modulate deep convection.

1.3 Organization

To the extent possible, each chapter is written so that it is a self-contained unit that can be understood without reference to the other chapters. The organization of this thesis is as follows.

The PACS mooring data are briefly described in Chapter 2. Readers not interested in the details of the mooring data collection and processing can skip Chapter 2. Several data sets derived from satellite observations are used in this thesis; these are described in the chapters in which they are used.

In Chapter 3, the observed evolution of SST and surface heat fluxes is presented, and the relative influence of surface heat fluxes, horizontal advection, and other processes in determining the evolution of upper ocean temperature is examined. Discussion focuses on the different roles of ocean dynamics at the two sites in contributing to horizontal advection and on the apparent coupling of surface heat fluxes with the local SST variability at the northern site.

In Chapter 4, the intraseasonal signal in meridional velocity is examined in its broader spatial and temporal context, and some important characteristics of the variability are quantified. The leading hypotheses for the variability are discussed and examined in light of these new insights into the characteristics of the variability.

In Chapter 5, the relationship between mesoscale SST variability and atmospheric convection, suggested by the buoy data at 10°N, is examined over a broader spatial and temporal domain using satellite-derived data. The interpretation of this relationship is discussed, and a hypothesis is advanced about how the resulting signal in solar radiation might feed back onto the upper-ocean temperature.

Chapter 6 summarizes the work presented in this thesis and its significance.

Chapter 2

Data and Processing

While this thesis utilizes several data sets, essential to this study are the high-quality moored measurements of upper ocean and surface meteorological properties that were collected as part of the NOAA-funded Pan American Climate Study (PACS) field project. This chapter addresses the collection and processing of the mooring data. Other data sets used in this thesis are described in the chapter in which they are used.

2.1   Mooring Deployment

From April 1997 through September 1998, air-sea interaction moorings were deployed near 10°N, 125°W and 3°S, 125°W as part of the PACS field project (Figure 1-1). The northern mooring location was chosen because of its proximity to the climatological position of the ITCZ. The 3°S, 125°W mooring site is within the region where the equatorial cold tongue normally appears, but the site was chosen to be south of the equator, which is routinely sampled by TAO moorings instrumented with current meters. The instrumentation on these moorings was selected to provide accurate time series of air-sea fluxes, surface meteorology, and upper ocean temperature, velocity, and salinity.

The initial deployment cruise was conducted aboard the *R/V Roger Revelle* from April 9 to May 5, 1997 (Way et al., 1998). A mid-term cruise was undertaken aboard the *R/V Thomas Thompson* to recover, service, and re-deploy the moorings between November 28 and December 26, 1997 (Trask et al., 1998). Finally, the moorings were recovered from the *R/V Melville* during September 6 to September 30, 1998 (Ostrom et al., 1999).

17
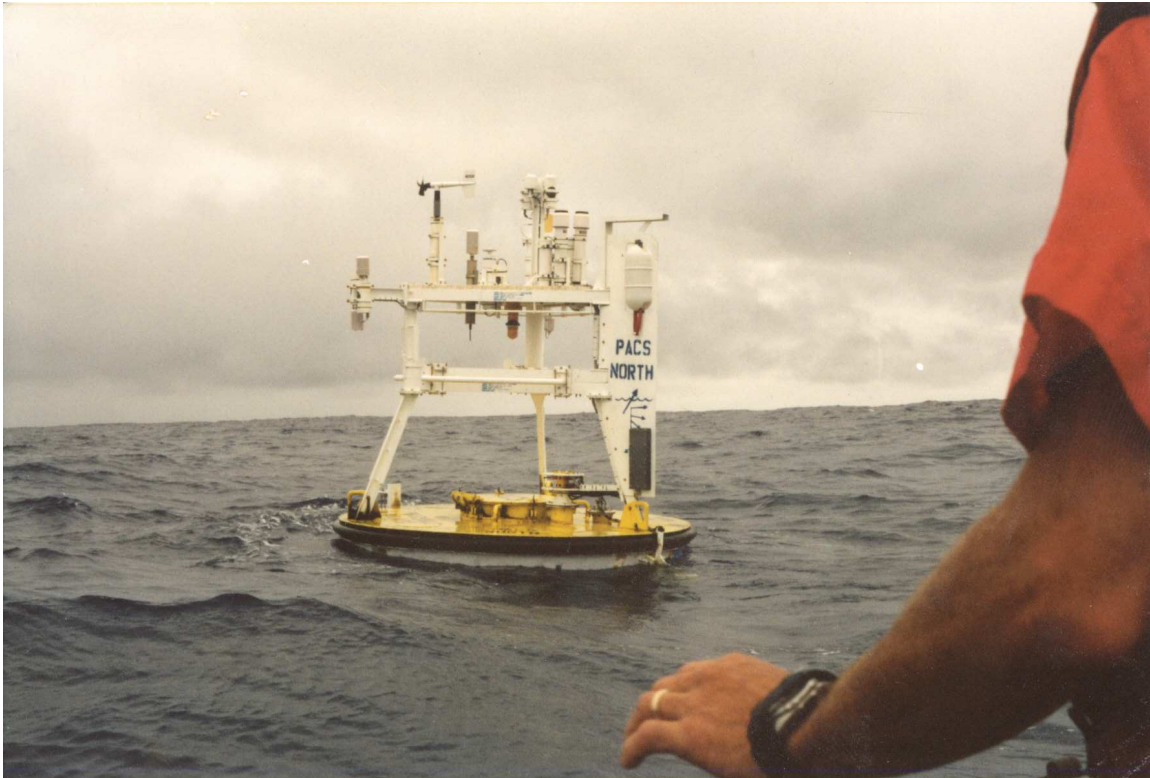
Figure 2-1: The PACS North buoy after deployment.

2.2 Instrumentation

The various sensors carried on the PACS buoys and mooring lines are described in detail by Anderson et al. (2000). The PACS moorings were heavily instrumented, often redundantly, both above and below the sea surface. On the buoy, an IMET (Improved METeorological) package provided measurements of wind velocity, air temperature, barometric pressure, relative humidity, precipitation, incoming short-wave radiation, and incoming long-wave radiation. Redundantly, a Vector Averaging Wind Recorder (VAWR) measured the same quantities. Below the surface, but mounted to the buoy in the upper 3 m of the ocean (Figure 2-2), there were seven independent temperature sensors and a SEACAT conductivity/temperature sensor. In addition, sea surface temperature was measured using a floating temperature sensor. In the second phase of the field program, there were also stand-alone instruments to provide independent measurements of precipitation, relative humidity, and air temperature. Table 2.2 gives some details about the specific types of sensors used, their accuracy, and the averaging interval for the measurements.

The mooring line was also heavily instrumented. Generally, there were temperature
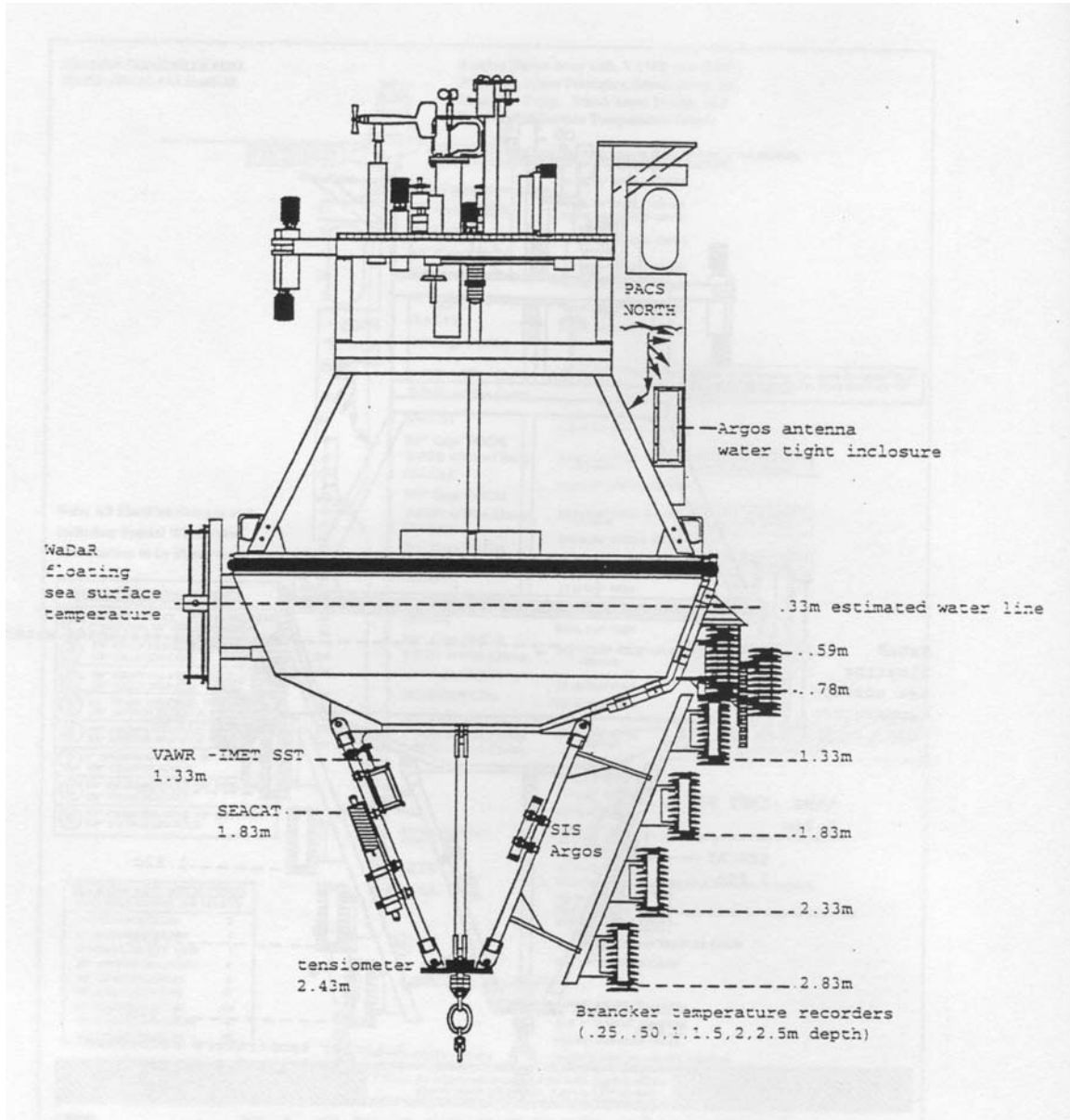
Figure 2-2: Schematic showing the near surface instrumentation for the second phase of the field program (from Anderson, et al., 2000).

Parameter	Sensor type	Nominal accuracy	Averaging interval
Wind speed	3-cup Anemometer[+]	±2%	15 min
	R.M. Young 3-cup[+]	±5%	15 min
Wind direction	Integral vane w/ vane follower[+]	± 1 bit (5.6 deg)	15 min
Insolation	pyranometer[+]	± 3%	15 min
Incoming long-wave radiation	pyrgeometer[+]	± 10%	15 min
Relative humidity	Variable dielectric conductor[+]	± 2%	15 min
	stand-alone/ASIMET[*]	± 3%/± 2%	3.75 min
Barometric pressure	Quartz crystal[+]	± 0.2 mbar when wind ≤ 20 m/s	15 min
SST	Thermistor[+]	± 0.005°C	15 min
Air temperature	Thermistor (unaspirated)[+]	± 0.2°C for wind ≥ 5 m/s	15 min
	stand-alone/ASIMET[*]	0.05 deg C	3.75 min
Subsurface temperature	SEACAT	0.005°C[@]	7.5 min
	MicroCAT	0.005°C[@]	3.75 min
	Brancker	0.005°C[@]	30 min
	VMCM	0.005°C[@]	7.5 min
Conductivity	SEACAT	0.01 psu	7.5 min
	MicroCAT	0.01 psu	3.75 min
Vector current	VMCM	1 cm/s	7.5 min
Precipitation	RM Young rain guage	0.1 mm/hr	3.75 min

Table 2.1: Table of measurement accuracies. [+]Part of VAWR package. [*]The stand-alone unit was deployed during phase 1 of the field study, while the ASIMET package was deployed during phase 2. [@]In the laboratory, the accuracy is considerably higher, but this is the nominal accuracy that we estimate for field measurements.

sensors down to 200 m depth, Vector Measuring Current Meters (VMCMs; Weller and Davis, 1980) down to 110 m, and SEACAT conductivity sensors down to 80 m. For all sensors, vertical resolution was weighted toward the surface. The temperature sensors had the best vertical resolution, with about 30 sensors on the upper 200 m. At deployment, salinity and velocity measurements had comparable resolution, with 8-10 sensors. Figure 2-3 depicts a typical mooring configuration for the PACS field program; there were differences in the sensor locations for each deployment at the two sites. (In this thesis, instrument depths will be noted as appropriate.)

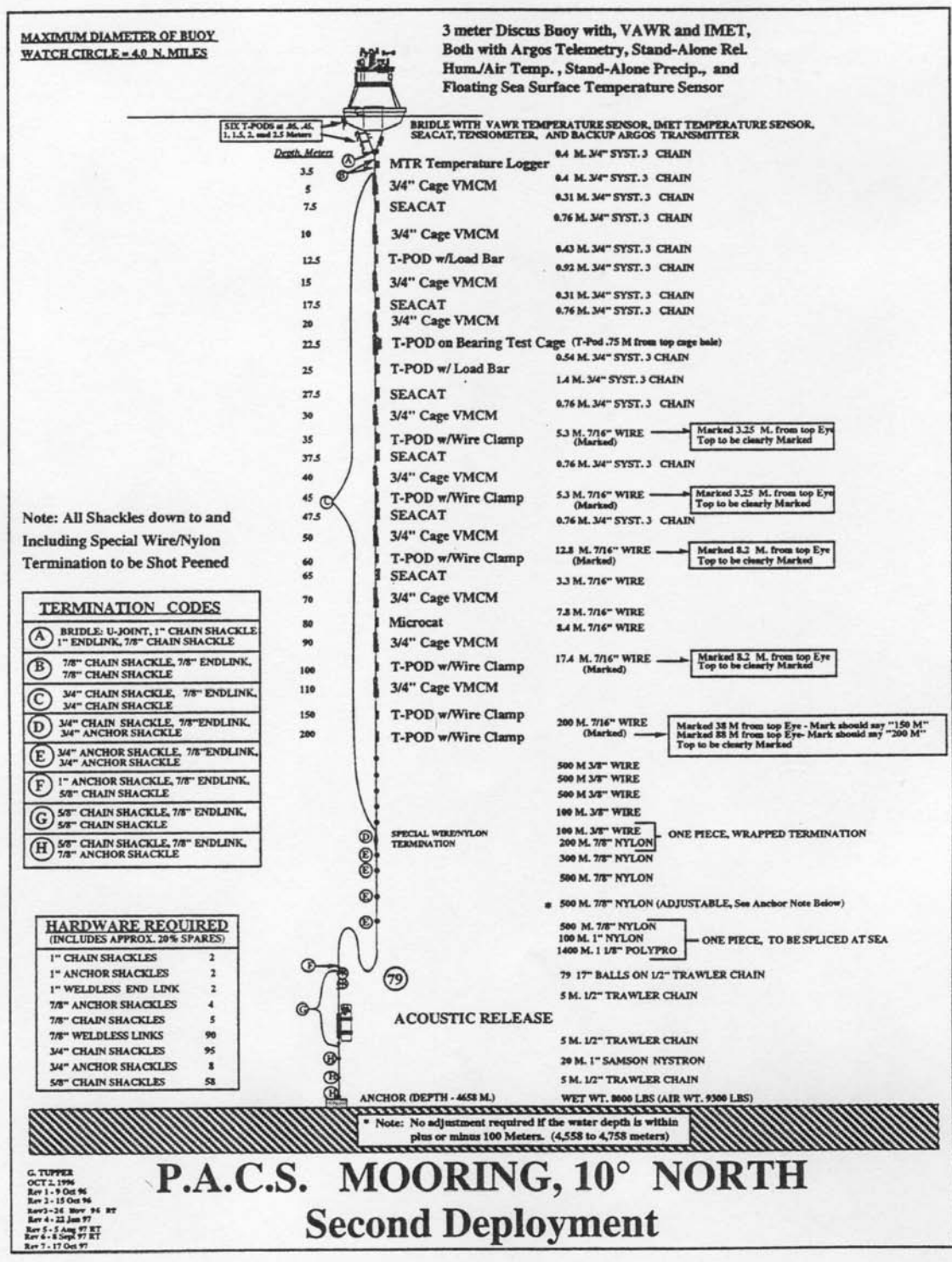Figure 2-3: Schematic showing the mooring configuration for the second phase of the field program (from Anderson, et al., 2000).

2.3 Data Processing and Data Return

Details of the quality control and data processing can be found in Anderson et al. (2000), but some relevant aspects are presented here. The surface meteorological and current meter measurements were processed using software developed by the WHOI Upper-Ocean Processes (UOP) Group and pre-deployment calibrations were applied to each instrument. When redundant measurements were available, inter-sensor comparisons were carried out, and efforts were made to determine which record was more reliable. Post-deployment calibrations were used when they produced better agreement in comparisons between redundant instrumentation. All compass readings (surface and subsurface) were rotated as appropriate (by about 10°) to correct for local magnetic deviation from true north. The processed data were visually inspected for sensor failure or gross errors. Sampling intervals for all instruments (including the meteorological packages) were 15 minutes or less. All of the data was averaged to a common 15 minute time base, and the data used here were further averaged to a 1-hour time base. In addition to post-processing carried out by Steven Anderson and others, a slight bias error ($\sim 0.1°C$) in the 3.5 m subsurface temperature record during the second deployment at the northern site was identified (and corrected) by sensor inter-comparison during times when the temperature was believed to be vertically uniform.

Northern site

Two of the VMCMs ceased to produce meaningful data when the rotors failed on October 14, 1997 (20 and 40 m). The near simultaneous failure combined with the 20 m vertical separation between the two current meters suggests that a fishing vessel near the buoy ensnared the mooring with its lines. The problem was solved during the recovery and redeployment cruise on December 19, 1997 when the mooring was replaced.

Two of the Sea-bird SEACAT temperature and conductivity sensors also failed to produce data during the first phase of the field study (22.5 and 32.5 m). One was lost at sea, and the other was severely damaged. These two sensors were located between the two damaged current meters, and it seems likely that all four sensors were damaged by the same fishing vessel.

The floating SST sensor was also damaged during the first phase of the field program. The sensor was designed to follow the sea surface by floating up and down along stainless

steel rods. Upon recovery, one of the rods was bent, causing the sensor to remain out of the water. We believe that the rod was bent when a fishing vessel tied up to the buoy, possibly in order to pull the buoy to one side in order to catch fish that congregate around the mooring. The float functioned properly immediately after deployment and for the duration of the second leg of the field study.

Southern site

During the first deployment, two Brancker TPODs, a Sherman current meter, and a FSI acoustic current meter failed to return any meaningful data (depths of 35, 150, 120, and 130 m, respectively).

During the second deployment, two Seabird SEACAT (temperature and conductivity) sensors (1.5 m and 7.5 m) returned only partial records, extending to September 5, 1998 and July 2, 1998, respectively. In addition, three Brancker TPODs (0.5, 2.5, and 60 m), a Sherman current meter (120 m), and a VMCM returned no data.

Salinity estimation

Some of the calculations in this thesis require knowledge of salinity at depths where salinity was not measured. At the northern site, damaged sensors during the first deployment limited the useful salinity information to only three depths in the upper 80 m. At the southern site, the 1997-98 El Niño caused the pycnocline to be deeper than anticipated during the first deployment, and thus the salinity measurements did not always span the pycnocline. Nonetheless, a large amount of salinity data was collected at each site; there were about 73,000 hourly estimates of salinity at the southern site and about 63,000 hourly estimates at the northern site. This subsection describes the procedure to estimate salinity at depths where it was not measured by taking advantage of the fairly close relationship observed between coincident measurements of temperature and salinity.

Scatter plots of salinity versus temperature (Fig. 2-4) suggest that salinity can be predicted from temperature within 0.5 psu for temperatures less than about 26° (northern site) or 27°C (southern site). Temperatures higher than these thresholds correspond to temperatures from the mixed layer during the rainy seasons, as indicated by the large range (up to 3 psu) of salinity observed at these temperatures. The anomalously large thermocline
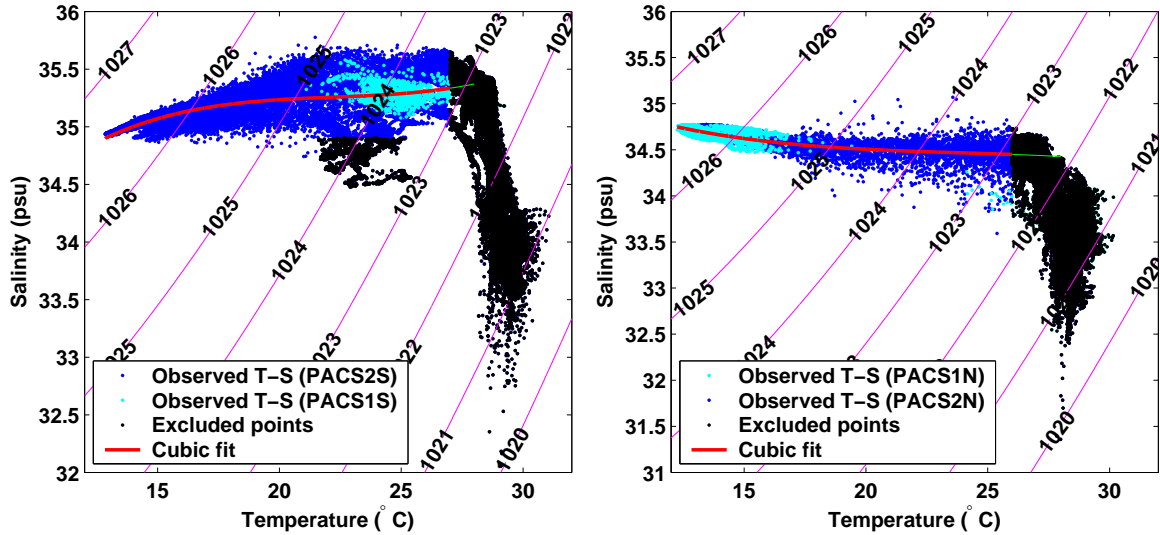
Figure 2-4: Observed temperature-salinity relationship (points) and cubic least-squares fit (red line). Left panel: southern mooring site. Right panel: northern mooring site. The black points were not used in the fit, and the rationale for their exclusion is explained in the text. Isopycnals, computed for a pressure of 50 db, are overlaid for reference (pink lines).

excursions associated with ENSO proved fortunate for this purpose, since this allowed sampling of a wide range of T-S values by a limited number of temperature-conductivity sensors. To take advantage of the relatively close T-S relationship at deeper levels, salinity was estimated by a cubic least squares regression approach. Before performing the regression, some "outliers" were removed from the southern record (near 23°C, 34.5 psu in Fig. 2-4) because inspection of the data revealed that these points were associated with an extreme shoaling of the thermocline (to about 17 m depth) during the La Niña event and that the T-S relation during this time was clearly anomalous. In addition, temperatures exceeding 26 and 27°C were excluded from the regression for the northern and southern sites, respectively. The resulting regression curves are indicated in Fig. 2-4.

One may question the usefulness of a cubic regression of salinity against temperature when the relationship shows appreciable scatter and a weak dependence of salinity on temperature. For example, would an assumption of constant salinity work just as well? One way to quantitatively measure of the utility of the fit is to assess the distribution of salinity values at a given temperature about the estimated regression curve, which allows an estimate of the likely error in salinity estimates inferred from the regression. Toward this end, T-S pairs were binned in 0.2°C by 0.02 psu bins to produce a histogram of the number of samples as a function of T and S. To obtain a normalized distribution of salinity values at a given

24
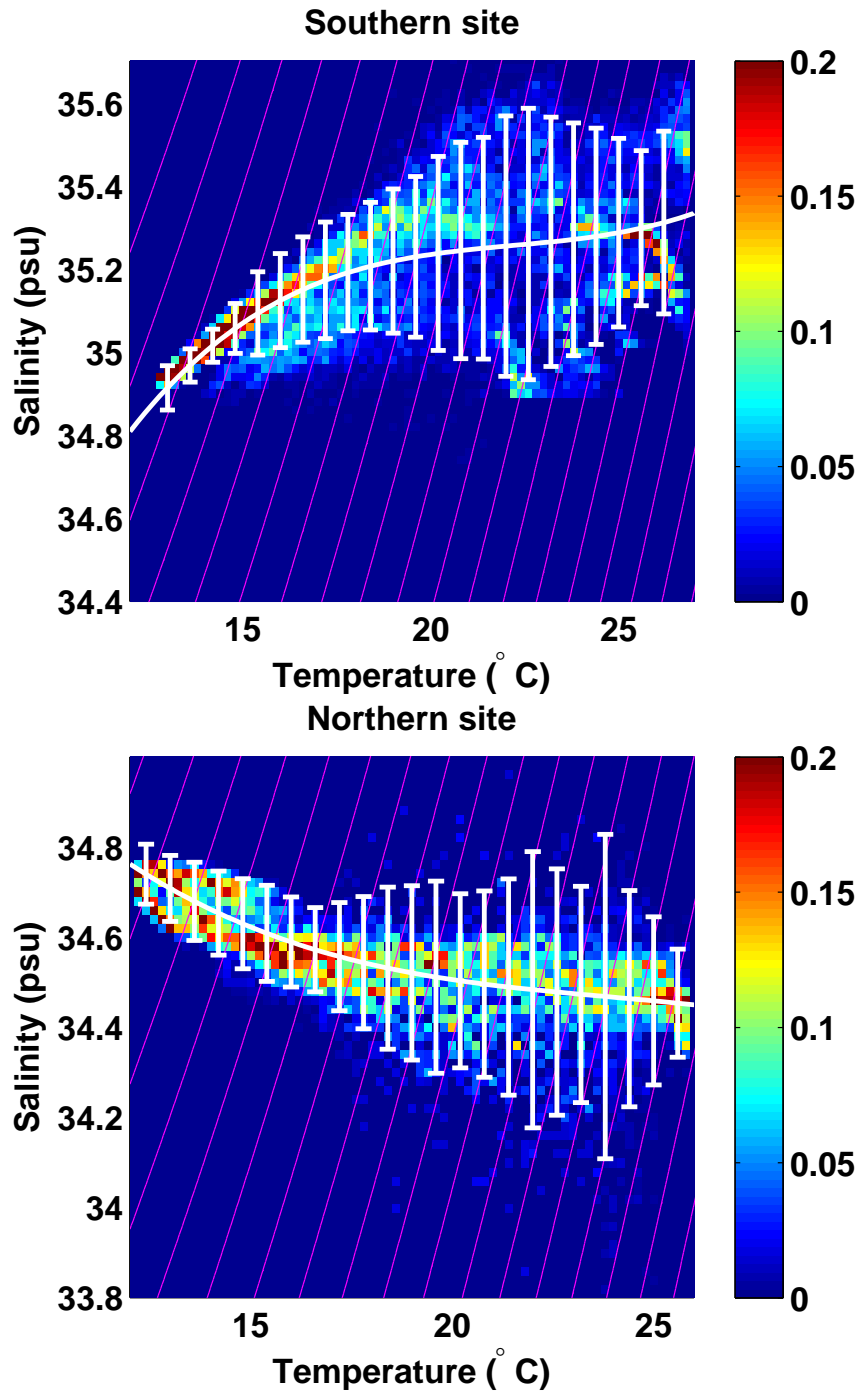
Figure 2-5: Colored fields: Fraction of the total salinity observations within each temperature class (0.2°C bins) accounted for by each salinity class (0.02 psu bins). In other words, the total number of observations in each T-S bin has been normalized by the total number of observations within each temperature bin. Upper panel: southern mooring site. Lower panel: northern mooring site. The white line shows the cubic fit described in the text, and the error bars encompass 85% of the salinity observations at within each temperature bin (see text for details). Isopycnals, computed for a pressure of 50 db, are overlaid at 0.25 kg/m^3 intervals (pink lines) to allow visual assessment of the error in density associated with errors in salinity inferred from the regression.

temperature about the estimated regression curve, the number of samples in each bin was normalized by the total number of samples at each temperature (Figure 2-5). Then, the likely error in inferred salinity was assessed by computing the range of salinity about the regression curve that accounts for some fraction (85% was chosen here) of the total number of samples. The range of salinity values about the regression curve accounting for 85% of the observed salinity values is a function of temperature, and the maximum range is about 0.3 psu at both sites (Figure 2-5). (Note that the error bars in Figure 2-5 have been averaged over three adjacent temperature bins for clarity of presentation.) For these maximum errors, this corresponds to an uncertainty in density of about ±0.25 kg/m^3 (Figure 2-5). The estimated errors are considerably smaller at other temperatures, typically ±0.2 psu or about ±0.125 kg/m^3, and some of the error bars do not overlap, indicating that the cubic regression is a quantitative improvement on an assumption of constant salinity. Regression estimates of salinity are clearly inferior to estimates from direct measurements, but for calculations in this thesis, the resulting uncertainty in density is acceptable. Calculations using this regression (Chapter 3) will take account of the error inherent in this approach when assessing the significance of the results obtained.

2.4   Estimation of Air-sea Fluxes

The WHOI UOP Group used the surface meteorological and near-surface oceanographic measurements to determine the air-sea fluxes according to the TOGA COARE[1] bulk flux algorithm of Fairall et al. (1996a). Although the algorithm includes corrections for 'cool skin' and 'warm layer' effects (cooling of the upper few millimeters and warming of the upper few meters of the ocean due to heat exchange), only the cool skin correction was employed in the flux calculations because the warm-layer correction is expected to be small as a result of the shallow (5 cm) measurement depth of the surface temperature.. The wind speed relative to the sea surface was calculated as the difference between the measured vector winds and the near surface current meter record. Full details of the air-sea flux calculations are given in Anderson et al. (2000).

The outgoing long-wave radiation (O($10\mu m$)) was estimated using the Stephan-Boltzmann

---

[1]TOGA COARE stands for the Coupled Ocean-Atmosphere Response Experiment of the Tropical Ocean-Global Atmosphere research program.

law, which can be expressed as $\frac{power}{area} = \epsilon\sigma T^4$, where ϵ is the sea surface emissivity ($\epsilon = 0.97$), σ is the Stefan-Boltzmann constant, and T is the sea surface skin temperature in degrees Kelvin. The skin temperature is used because long-wave radiation depends on the interfacial temperature, which is slightly less than the temperature found about a millimeter below the surface (Saunders, 1967).

The precipitation rate was estimated by first-differencing measured accumulation in time. The R.M. Young rain gauge measures accumulated precipitation using a capacitance technique to determine the amount of water in a collection chamber. Due to limited sample volume, the gauge siphons off the accumulated precipitation when the chamber is full. This process leads to spurious negative spikes in the precipitation rate, and these spikes were identified and replaced with zeros. Some additional noise in the precipitation rate was identified, and we believe that this noise may be produced by electro-magnetic interference with nearby sensors (perhaps the Argos telemetry). The first-difference derivative may have also contributed to this noise. The noise appears to be about 0.1 mm/hr based on the noise about 0.0 mm/hr during times when the precipitation rate was known to be zero. Consequently, we rejected signals in the precipitation rate that were smaller than the estimated noise by setting precipitation rates less than 0.1 mm/hr to zero. The accumulated precipitation was then estimated as the time integral of the corrected precipitation rate.

The accuracy and applicability of the TOGA COARE bulk flux algorithm has been demonstrated in many contexts. The algorithm development involved simultaneous measurements from land stations, buoys, six research vessels, and 267 low-level airplane fly-overs (Weller et al., 2004). As a result of this intensive inter-comparison and inter-calibration campaign, measurement techniques and the bulk flux formulae were substantially improved, allowing the TOGA COARE Flux group to meet their goal of closing the monthly-average ocean heat and freshwater budgets to within 10 W/m^2 and 20%, respectively (Weller et al., 2004). Since the TOGA COARE program, the Flux group has continued the coordinated effort to refine the bulk formulae and measurement techniques. Now, IMET surface fluxes, computed using the COARE flux algorithm, are being used for validation of other flux products (e.g. Shinoda et al., 1998; Shinoda and Hendon, 1998). Combined with accurate measurements of bulk surface meteorological properties, the TOGA COARE algorithm provides the best possible estimate of air-sea fluxes of heat, freshwater and momentum when direct covariance measurements of the fluxes are not available.

Chapter 3

Observed Surface Layer Temperature Balance

In this chapter, the temperature balance of the surface layer is examined at each mooring site in order to allow quantitative estimates of the role of surface heat fluxes and horizontal advection in setting the temperature of the mixed layer on timescales longer than three weeks. Inferences are also made about the importance of vertical heat fluxes at the base of the mixed layer. Results regarding horizontal advection and surface heat fluxes at the northern site serve as the foundation for the remainder of the thesis.

The observed evolution of SST and surface heat flux is described in Section 3.1. Section 3.2 describes the method by which the surface layer temperature balance is estimated. Section 3.3 presents the results and is followed by a discussion (Section 3.4).

3.1   Observed evolution of SST and surface heat flux

The surface temperature record at the southern site was dominated by the El Niño/La Niña signal. SST was within about 1°C of climatological values during during May 1997 but remained nearly steady during the boreal summer months when SST would normally be cooling (Figure 3-1). The largest deviation of SST from climatological conditions occurred in December of 1997, but temperatures continued to rise through April 1998. Peak El Niño temperatures at the site exceeded 29°C during March and April of 1998, and temperatures sometimes exceeded 31°C during this time in association with the diurnal cycle (Figure 3-1).

29

Figure 3-1: Southern site (3°S, 125°W). Upper panel: surface heat flux (3-week running average). Lower panel: SST (5 cm depth, hourly data) and Levitus and Boyer (1994) climatological SST.

This warm period was followed by a period of steadily decreasing surface temperatures; SST fell to about 24°C by mid-July of 1998.

As SST decreased in association with La Niña (e.g., McPhaden, 1999), the net heat flux to the ocean increased markedly, reaching values in excess of 180 W/m² by August of 1998 (Figure 3-1). Examination of the contributions to the net heat flux from latent, sensible, and radiative heat fluxes (Figure 3-2) reveals that this increase of the net heat flux during 1998 was due primarily to a marked decrease of evaporative heat loss as SST decreased. This tendency of surface heat flux variations to damp interannual SST anomalies in the eastern equatorial Pacific has been noted previously (Wang and McPhaden, 2001).

El Niño did not have an obvious impact on the evolution of SST at the northern site. SST was relatively warm in the the summers of 1997 and 1998, and it was coolest during January-May of 1998, as might be expected from the climatological seasonal cycle (Figure 3-3). The tendency for warm SST during the summer is closely linked with the presence of the ITCZ, which is associated with frequent precipitation and weak winds. When the ITCZ is south of the mooring site (roughly December 1997 through June 1998), the northeasterly

Figure 3-2: Surface heat flux components at the southern site. All quantities have been smoothed by a 3-week running average. Noteworthy features are: (1) latent and solar heat fluxes are the dominant contributions to the total heat flux, (2) the very warm El Niño SST between December 1997 and May 1998 was accompanied by decreased (and variable) solar radiation and increased net-longwave radiation associated with enhanced atmospheric convection near the equator during that time, and (3) the contrast of El Niño and La Niña can be seen clearly in the difference in the latent heat flux between the summers of 1997 and 1998.
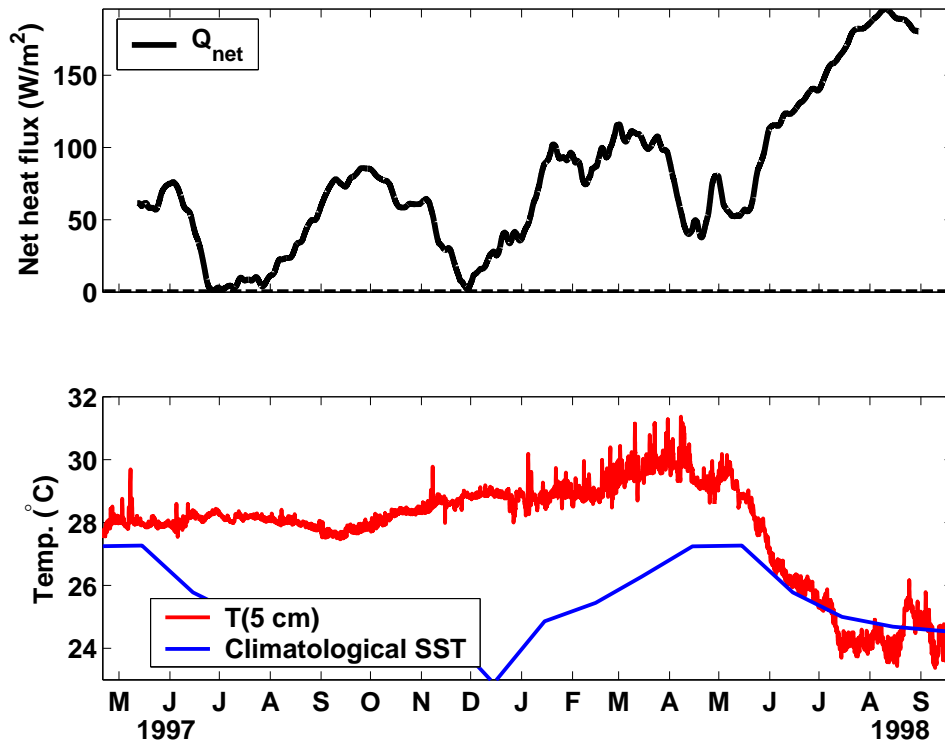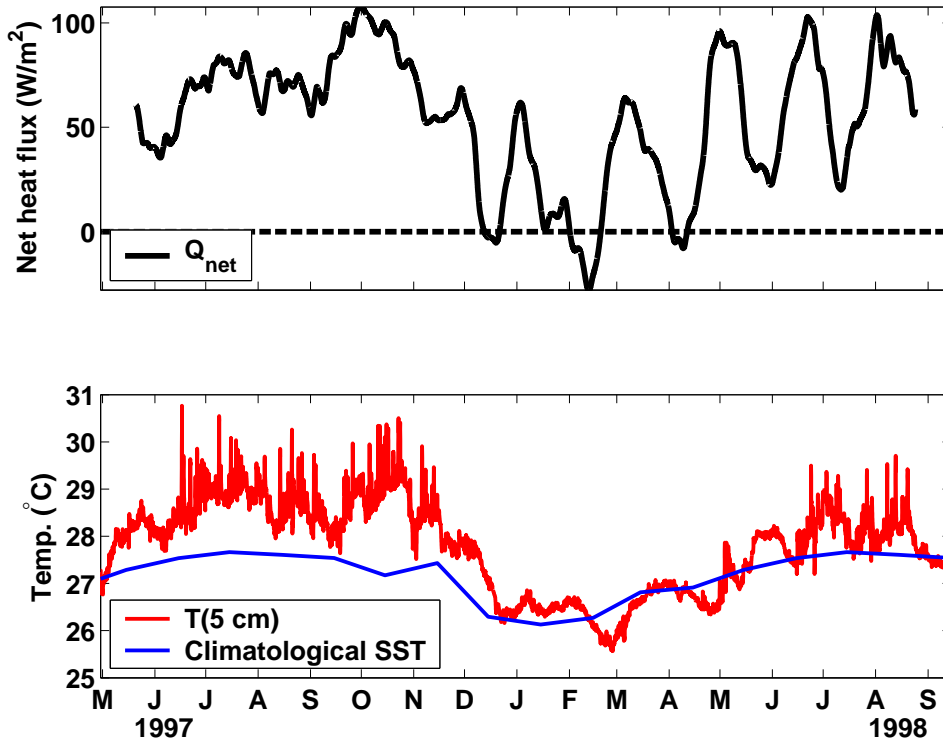
Figure 3-3: Northern site (10°N, 125°W). Upper panel: surface heat flux (3-week running average). Lower panel: SST (5 cm depth, hourly data) and Levitus and Boyer (1994) climatological SST.

trade winds are present at the site, contributing to strong, steady winds and enhanced evaporation. This seasonal variation of wind speed associated with the meridional migration of the ITCZ contributes to seasonal variations in the size of the diurnal cycle of SST. The decrease of wind speed and short wave radiation associated with the presence of the ITCZ represent competing effects on the size of the diurnal SST signal, but since the amount of diurnal warming depends more sensitively on the wind-stress magnitude than on surface heat flux (Fairall et al., 1996b), the diurnal cycle of SST is larger during the weaker winds of the ITCZ season.

One might expect the frequent convection and cloud cover within the ITCZ to block incoming solar radiation and reduce the net heating of the ocean, but the 17-month time series of net heat flux at the site shows that the heat flux was larger when the ITCZ was over the mooring site. Inspection of the individual components that make up the net heat flux suggests that the 21-day averaged solar heating is modulated by the presence of the ITCZ (Figure 3-4), but the increase in solar heating at the site associated with the southward migration of the ITCZ is no more than 50 W/m². This effect is overwhelmed by an increase

of evaporative heat loss from the sea surface as the humid, low-wind conditions of the ITCZ season give way to the drier, windier trade-wind season. The associated change in latent heat flux between August-October 1997 and January-April 1998 was roughly 100 W/m^2.

One feature that stands out during inspection of the net heat flux at the northern site is the presence of strong intraseasonal variability with a period of 40-70 days (Figures 3-3 and 3-4). This variability is present from January 1998 through the end of the record, and it has a magnitude comparable to that of the annual cycle. There are variations in SST at similar time scales. Contributions to this variability in the net heat flux come from variations in latent, sensible, and solar heat fluxes (Figure 3-4).

While inspection of the time series of SST and heat flux indicates that both sites exhibited coherent variability in SST and surface heat flux, better understanding of this relationship requires a quantitative measure of the importance of the surface heat flux in setting SST. Examination of the mixed-layer temperature balance (below) allows quantitative understanding of the relative roles of surface heat fluxes, advection, and entrainment in setting SST, which, in turn, gives insight into the extent to which variations in heat fluxes are the cause or the result of the variations in SST.

3.2 Temperature balance approach

Excluding solar heating, heat that passes across the thin (O(1 mm)) diffusive-conductive boundary layer at the sea surface is carried to or away from the surface (depending on the sign of the surface flux) primarily by turbulent transport in the ocean boundary layer and serves to heat or cool the (typically) weakly stratified upper ocean. In part because it is difficult to measure a time series of the near-surface vertical turbulent heat transport, the role of the surface fluxes in setting upper-ocean temperature is usually assessed by comparing the rate of change of upper-ocean temperature, integrated from the surface to some depth, to the surface heat flux. Vertical integration across the boundary layer excludes from consideration the vertical turbulent heat flux within the boundary layer and places more emphasis on the role of turbulent transport at the integration depth.

The vertical integration of temperature (or heat) in the upper ocean can be carried out to a fixed depth (e.g., Emery, 1976; Merle, 1980) or to a depth that varies through time to track a physically meaningful surface like an isopycnal or the base of the mixed-layer
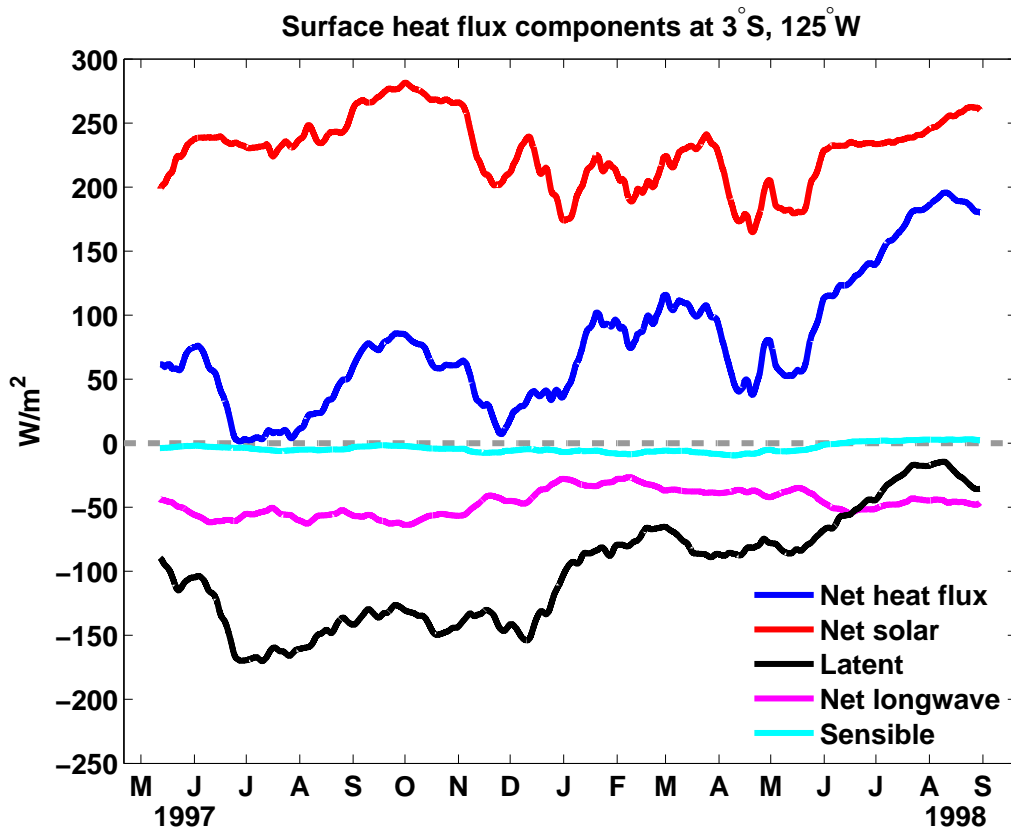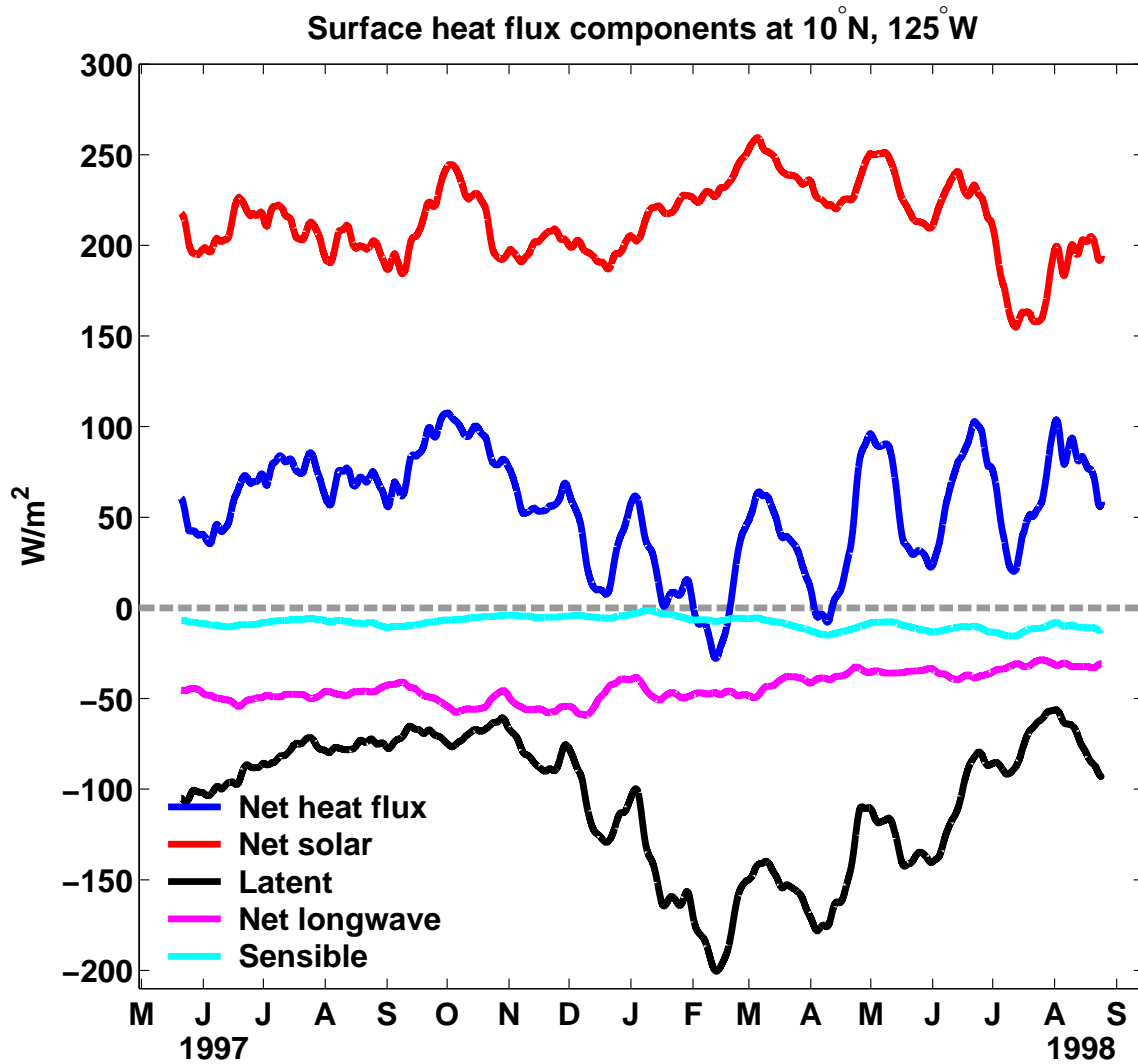
Figure 3-4: Surface heat flux components at the northern site. All quantities have been smoothed by a 3-week running average. Noteworthy features are: (1) latent and solar heat fluxes are the dominant contributions to the total heat flux, (2) the influence of the meridional migration of the ITCZ, which is near the mooring during the summer and fall months, can be seen clearly in the latent heat flux, and (3) intraseasonal variability (nominally 40- to 100- day periods) can be seen in every quantity except the longwave heat flux.

(e.g., McPhaden, 1982; Niiler and Stevenson, 1982). The fixed integration depth is often chosen to be below a strong thermocline so that the unknown vertical turbulent flux at the base of the integration volume can be assumed negligible (e.g., Price et al., 1978; Fischer et al., 2002; Weller et al., 2002). As discussed by Stevenson and Niiler (1983), carrying out the integration to a fixed depth below the thermocline does reduce the size of the typically unknown turbulent flux term, but, if the goal is to understand the evolution of SST, this approach has the potential disadvantage that the vertically averaged temperature may merely be a measure of the depth of the thermocline and may not be representative of SST. This is a concern in the tropical Pacific, where the thermocline is particularly strong. For example, consider an idealized case where the vertical thermal structure is represented by two layers with a thermocline at 50 m depth (meant to be representative of the eastern tropical Pacific). If the temperature change across the thermocline is 13°C, then a 1° change in mixed layer temperature changes the vertically averaged temperature less than a 5 m change in thermocline depth. The seasonal variation of SST over much of the eastern tropical Pacific is 1-3°C while changes in thermocline depth are 10-40 m, so the temperature integrated to a fixed depth below the thermocline is expected to be dominated by variations in the depth of the thermocline. Thus, examination of the factors affecting temperature integrated to a fixed depth below the thermocline may not be the best approach for understanding the factors affecting SST.

In contrast, when the integration is carried out to a time-variable depth that tracks the base of the surface layer, the vertically averaged temperature should be a better measure of SST, to the extent that vertical variations in temperature are small above the integration depth. This approach is often employed for examination of the processes influencing tropical SST and upper-ocean heat content (e.g., Smyth et al., 1996; Cronin and McPhaden, 1997; Wang and McPhaden, 1999, 2001; Toole et al., 2004), and it is the approach employed here. This section describes the approach to estimation of the surface layer temperature balance at the two mooring sites.

3.2.1 Theory

A clear and complete derivation of the "heat storage rate equation" used for the temperature balance computation is given by Moisan and Niiler (1998); only a sketch of the derivation will

be given here. The derivation starts with the approximate equations governing conservation of heat and mass, i.e.,

$$\rho c_p \left(\frac{\partial T}{\partial t} + u \frac{\partial T}{\partial x} + v \frac{\partial T}{\partial y} + w \frac{\partial T}{\partial z} \right) = \frac{\partial Q}{\partial z}, \tag{3.1}$$

$$\frac{\partial u}{\partial x} + \frac{\partial v}{\partial y} + \frac{\partial w}{\partial z} = 0, \tag{3.2}$$

where the density (ρ) and the specific heat (c_p) are treated as constants. The derivation proceeds by combining equations 3.1 and 3.2 and integrating vertically from some spatially and temporally variable depth h to the surface. Without further approximation, the equation governing the depth-average temperature between the surface and the depth h can be shown to be

$$\underbrace{\frac{\partial T_a}{\partial t}}_{A} + \underbrace{\mathbf{u}_a \cdot \nabla T_a}_{B} + \underbrace{\frac{1}{h} \nabla \cdot \int_{-h}^{0} \hat{\mathbf{u}} \hat{T} dz}_{C} + \underbrace{\frac{T_a - T_{-h}}{h} \left(\frac{\partial h}{\partial t} + \mathbf{u}_{-h} \cdot \nabla h + w_{-h} \right)}_{D} = \underbrace{\frac{Q_o - Q_{-h}}{\rho c_p h}}_{E} \tag{3.3}$$

where the subscript a indicates the vertical average to depth h, e.g.,

$$T_a = \frac{1}{h} \int_{-h}^{0} T dz, \tag{3.4}$$

and the 'hats' indicate deviations from the vertical average, so that, e.g., $T(z) = \hat{T}(z) + T_a$. Equation 3.3 states that the rate of change of vertically averaged temperature (term A) is influenced by horizontal advection of the layer-average temperature gradient by the layer-average velocity (term B), vertical entrainment (term D), and the net vertical divergence of vertical heat fluxes over the layer (term E). There is also a contribution to the vertically averaged temperature from a term associated with correlated vertical variations of temperature and velocity (term C), which has the form of the divergence of a Reynolds correlation (or 'eddy flux'). (Term C is not an 'eddy flux' in the conventional meaning of the term; that is, it is not associated with mesoscale or turbulent fluctuations, per se.)

Although Equation 3.3 follows mathematically from Equations 3.1-3.2 for any choice of $h(t)$, physical considerations suggest that if the "entrainment term" is to have its conventional interpretation as being associated with mixing, then h should be chosen to follow an isotherm or an isopycnal rather than, for example, a mixed-layer depth chosen by a ΔT criterion.

When h is chosen as an isopycnal depth, the part of term D in parentheses is a diapycnal velocity (e.g. Pedlosky, 1998, pp. 100-102) and is nonzero only when there is mixing across the depth h.

Only some of the terms in Equation 3.3 can be directly estimated from available data. Thus it is helpful to manipulate Equation 3.3 further to explicitly separate the terms that can be directly estimated from those that cannot. The quantity Q_{-h} (the heat flux across the depth h) contains contributions from penetrating solar radiation and from vertical turbulent heat fluxes, which can be made explicit by writing $Q_{-h} = Q_{pen} + Q_{turb}$. Equation 3.3 can then be rewritten as,

$$\frac{\partial T_a}{\partial t} + \mathbf{u}_a \cdot \nabla T_a = \frac{Q_o - Q_{pen}}{\rho c_p h} + R, \tag{3.5}$$

where Q_{pen} is the amount of solar radiation that penetrates below the depth h, and

$$R = \frac{-1}{h} \nabla \cdot \int_{-h}^{0} \hat{\mathbf{u}} \hat{T} dz + \frac{\hat{T}_{-h}}{h} \left(\frac{\partial h}{\partial t} + \mathbf{u}_{-h} \cdot \nabla h + w_{-h} \right) + \frac{-Q_{turb}}{\rho c_p h}. \tag{3.6}$$

In the temperature balance calculation below, R will be inferred as a residual, and the other terms in Equation 3.5 will be estimated directly from data. The mixed-layer temperature balance equation (3.5) serves as the principal tool for analysis in this chapter.

3.2.2   Estimation of terms

This section describes the estimation of terms in Equation 3.5 for each mooring site. Many aspects of the estimation procedure are the same for the two sites, but differences in the evolution of upper-ocean temperature at the two sites requires the choice of the isopycnal defining h at each site to be considered individually. Thus, common aspects of the estimation procedure are described first, and then the choice of h is described for each site.

Aspects of estimation procedure common to both sites

At both sites, the horizontal gradient of T_a was estimated by a 4th-order accurate finite difference scheme applied to multi-channel SST data from the Advanced Very High Resolution Radiometer (AVHRR) on the NOAA polar orbiting satellites (Brown et al., 1993). This data set has 18 km spatial resolution, but the data were averaged to 54 km resolution prior to computation of the gradients. The resulting estimate of the horizontal temperature gradient

was linearly interpolated from the spatial grid of the satellite observations to obtain a time series at each mooring location. This type of approach to estimating ∇T_a is believed to provide a reasonably accurate estimate of the mixed layer horizontal temperature gradient (Wang and McPhaden, 1999, 2001). To suppress noise in the ∇T_a estimate due to measurement error and unresolved variability in the SST field and its subsequent amplification in the discretized derivative, the ∇T_a estimates were smoothed in time with a 7-point (49-day) running average filter. As such, only the contributions of the low-frequency ∇T_a are included in the calculation. This implies that eddy flux divergences associated with timescales less than about 50 days will be included in the residual term of the temperature balance.

Salinity at depths where only temperature data were available (e.g., due to sensor failures or, when required, at depths below the deepest conductivity sensor) was estimated by a cubic least squares fit between measured salinity and temperature as described in Chapter 2.

The decay of solar radiation with depth was modeled using a double-exponential decay profile, with decay constants corresponding to Jerlov Type IA water type (Paulson and Simpson, 1977). That is, the solar radiation profile is taken to be

$$I(z) = I(0)(Ae^{\gamma_1 z} + (1 - A)e^{\gamma_2 z}) \tag{3.7}$$

where A=0.62, γ_1=1.67 m^{-1}, γ_2=0.05 m^{-1}, and $I(0)$ is the net solar radiation at the surface. As discussed by Ohlmann (2003), for example, there are significant drawbacks to using such a simplistic parameterization of the solar decay profile since the transmission is dependent on chlorophyll biomass, solar zenith angle, and other factors. When the integration depth h is more than about 20 meters, the decay profile becomes less important since most of the radiation is absorbed above this depth. However, the solar heating is large in comparison to other contributions to the surface heat flux, and even small fractional errors in the amount of solar radiation penetrating below the depth h could exceed 10's of W/m^2. Therefore, the error budget (in appendix) explicitly accounts for both random and systematic errors in the decay parameterization, allowing for large random errors (60% in the decay depths, γ_1 and γ_2, and 25% in A, the proportion of shortwave and long-wave components) and systematic errors that almost completely cover the range of parameters given by Paulson and Simpson (1977) for Jerlov Types I, IA, IB, and II waters.

After estimation of the terms in the Equation 3.5, all terms were smoothed to suppress

variability at periods less than three weeks. This was done by applying a 3-day running average filter to suppress diurnal and other high-frequency variability, followed by a 21-day (504-point) running average filter. The error in each estimated term from Equation 3.5 was then estimated as described in the appendix. All figures and descriptions of the terms in the temperature balance equation are of these smoothed estimates.

Choice of h, Southern Site

At the southern site, the transition from El Niño to La Niña conditions led to a large variation in the temperature and density of the mixed layer, and there is no single isopycnal that tracks the base of the mixed layer for the duration of the record (e.g. Figure 3-5). Propagation of errors in the mixed layer temperature balance (in appendix) suggests that use of the shallowest non-outcropping isopycnal as a lower boundary for the vertical integration would lead to unacceptably large errors during the part of the record dominated by El Niño conditions. Thus, two different isopycnals are used for the calculation at 3°S: the 1023 kg/m^3 isopycnal is used until it outcrops in June of 1998, and the 1024 kg/m^3 isopycnal is used after that time (Figure 3-5).

The vertically averaged temperature, T_a, gives a fairly faithful representation of the SST (Figure 3-6). During the peak SSTs associated with El Niño around April 1998, T_a is least representative of SST as a result of the shallow stratification that is present during that time (as indicated by the 1022 kg/m^3 isopycnal in Figure 3-5). Still, even during this time of relatively poor agreement, T_a differs from the nighttime SST values by less than 1°C. (Daytime values of SST and T_a sometimes differ by more than 1°C in association with the extreme diurnal cycle of SST during this time that was associated with the weak surface winds at the peak of the El Niño event.)

The value of temperature at the depth h is important in the mixed layer temperature balance calculation, in part because the largest contribution to the error in T_a is proportional to $\hat{T}|(-h)$ (Equation 3.9 in appendix). The influence of the regression estimate of salinity on $T(-h)$ during June 1997 to January 1998 is evident (Figure 3-6); during this time when the 1023 kg/m^3 isopycnal was deeper than the deepest conductivity sensor, the isopycnal is nearly isothermal because of the one-to-one temperature-salinity relationship inherent in the regression estimate. Values at times when there were salinity measurements spanning the

Figure 3-5: Depth-time plot of (gridded) observed temperature at 3°S, 125°W. Temperature sensor locations during the two mooring deployments are indicated by yellow dots on the left and right edges of the figure. The black line indicates the 1024 kg/m^3 isopycnal, the turquoise line indicates the 1023 kg/m^3 isopycnal, and the white line indicates the 1022 kg/m^3 isopycnal.

isopycnal (prior to June 1997 and after February 1998) merge smoothly with the regression estimate. The continuity through time of temperature on the estimated 1023 kg/m^3 isopycnal suggests that the regression estimate of salinity was reasonably successful.

Choice of h, Northern Site

At the northern site, error estimates for various choices of the isopycnal defining the lower boundary of the integration suggested that the errors are acceptably small when a single isopycnal (1023 kg/m^3) is used for the entire record. This is so because the total variation of SST during the record was considerably smaller at the northern site in comparison to the southern site. However, when a single isopycnal is used, there are times when there is appreciable temperature stratification above the depth h (Figure 3-7), and, during these times, T_a does not give an entirely faithful representation of the SST (e.g. July-November of 1998 in Figure 3-8). Also, the difference between estimated values of T_a and $T(-h)$ exceeds 4°C during October-November 1997, and this contributes to relatively large errors in T_a during that time.

40
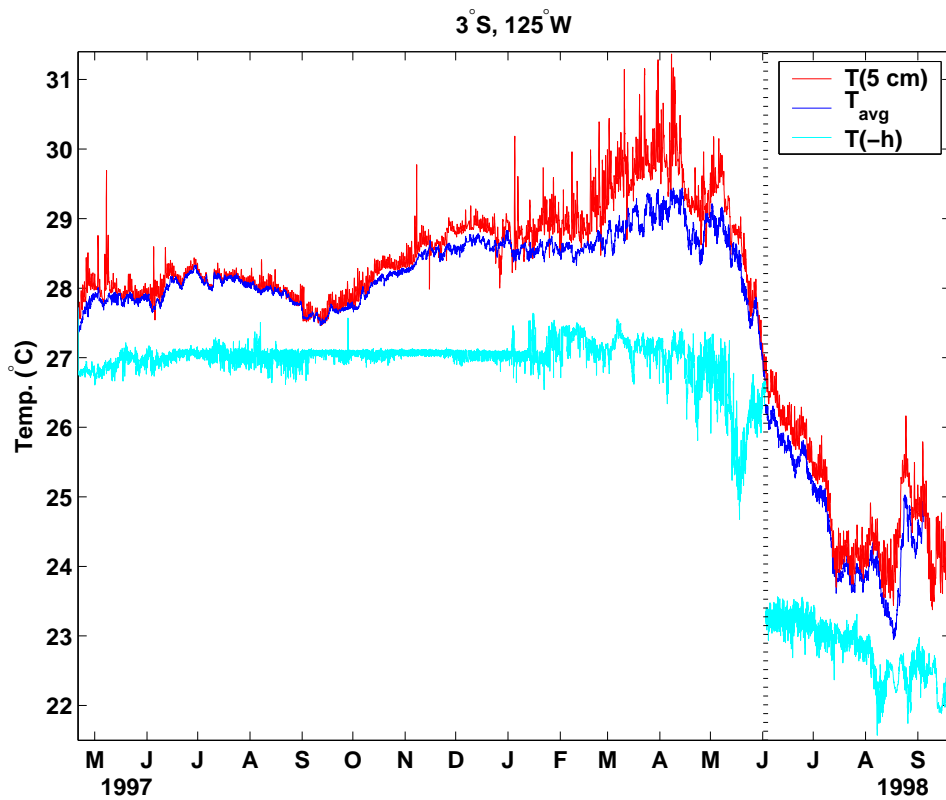
Figure 3-6: SST, T_a, and T_{-h} from the southern site. The integration was performed to the 1023 kg/m^3 isopycnal (left of heavy, black dashed line) and to the 1024 kg/m^3 isopycnal (right of heavy, black dashed line).
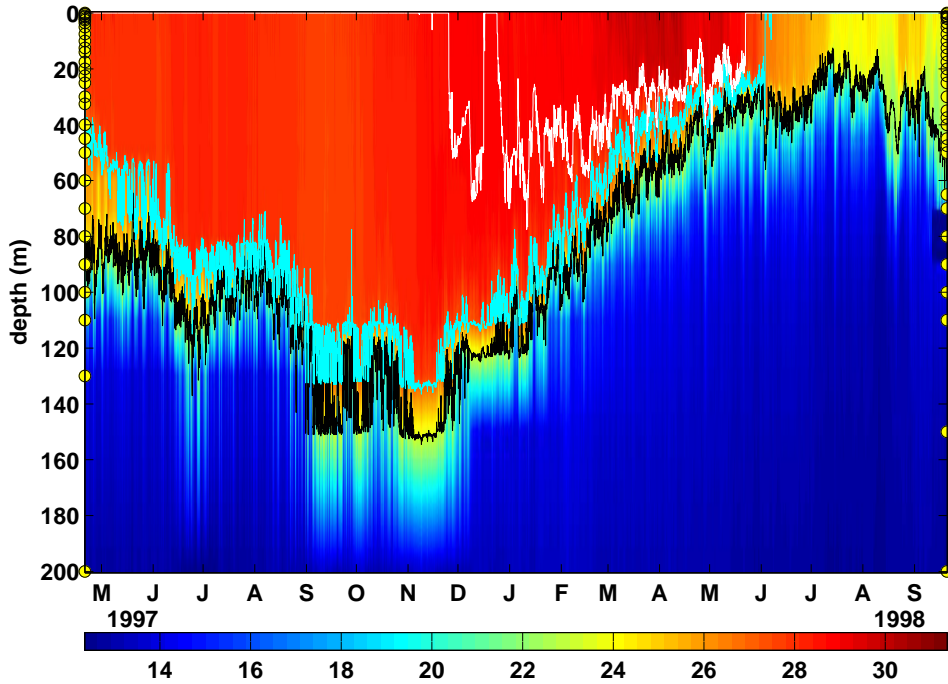
Figure 3-7: Depth-time plot of (gridded) observed temperature at 10°N, 125°W. Temperature sensor locations during the two mooring deployments are indicated by yellow dots on the left and right edges of the figure. The black line indicates the 1023 kg/m^3 isopycnal.
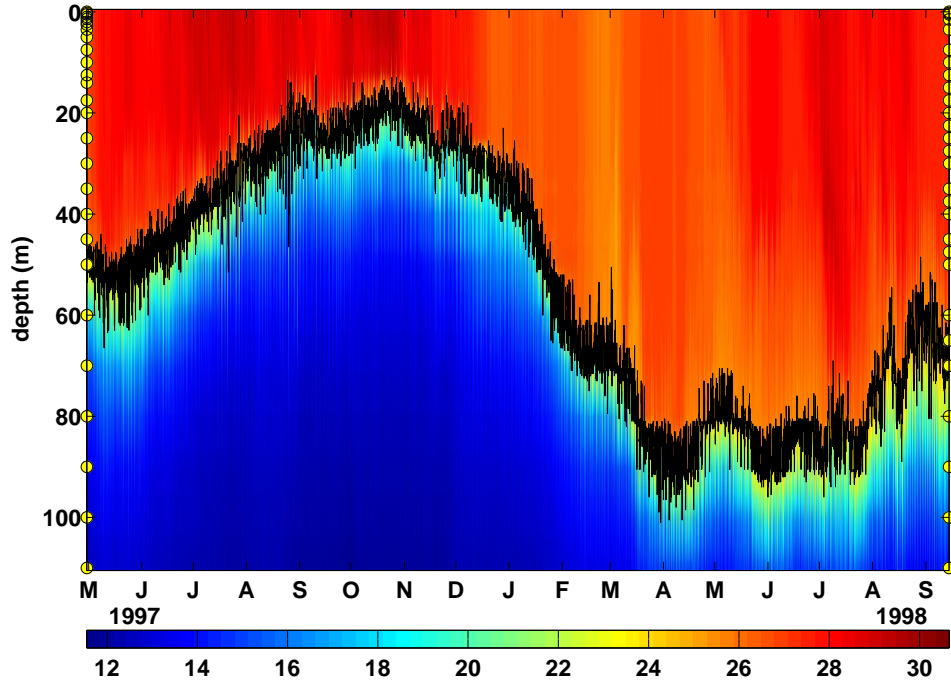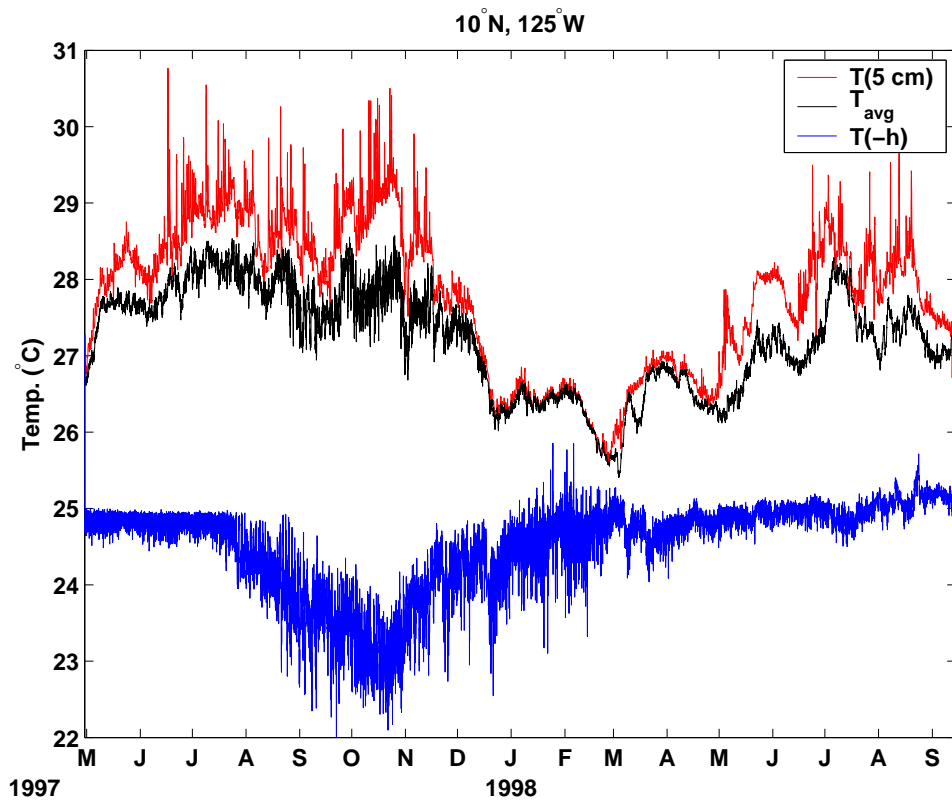

Figure 3-8: SST, T_a, and T_{-h} from the northern site. The integration was performed to the 1023 kg/m^3 isopycnal.

3.3 Results

3.3.1 Southern Site

The rate of change of mixed layer temperature at the southern site is dominated by the local transition to La Niña conditions (Figure 3-9), a period of large ($\sim$0.06°C/day), negative $\partial T_a/\partial t$. The overall balance from May 1998 onward is fairly complicated, with each term exerting substantial influence on the rate of change of mixed layer temperature at various times during the event. Horizontal advection was a strong cooling influence during May-July 1998. As the the cold event progresses, the surface heating term increasingly counteracts the cooling of SST through the combined influence of increasing surface heat flux and a shoaling mixed-layer depth. As the mixed layer and thermocline reach increasingly shallow depths, shoaling to less than 30 m by June 1998, the residual term becomes larger and acts to reinforce the cooling by horizontal advection.

It is of interest to examine the relative influence of zonal and meridional advection in bringing about the local transition to La Niña conditions at the mooring site. Most of the observations suitable for studying the role of advection in the transition from El Niño to La Niña in the eastern tropical Pacific have come from the equator (e.g., Wang and McPhaden, 2001). These studies have shown that zonal advection is more important than meridional advection. This is perhaps not surprising, because meridional temperature gradients tend to be small on the equator owing to the rough meridional symmetry of SST about the equator, and zonal currents tend to be stronger than meridional currents. In contrast, at 3°S, inspection of the relative contributions of zonal and meridional advection (Figure 3-10) reveals that meridional advection is much more important than zonal advection in bringing about the local transition to La Niña conditions. As the local La Niña conditions develop, the meridional temperature gradient is much larger than the zonal temperature gradient (Figure 3-10), as should be expected for a site located on the southern flank of the equatorial cold tongue. The zonal and meridional components of the layer-average velocity tend to be of comparable strength (not shown). With these factors in mind, it is not surprising that meridional advection should be more important than zonal advection in the local transition to La Niña conditions.

Before the rapid surface cooling began in May 1998, the temperature balance suggests
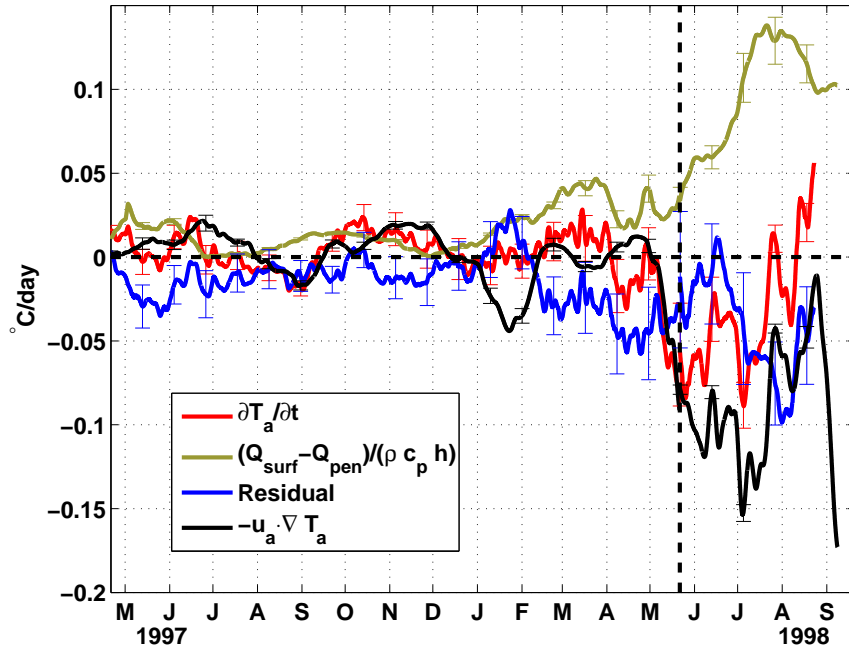
Figure 3-9: Terms in the mixed-layer temperature balance equation (Eqn. 3.5) at 3°S, 125°W. The integration was performed to the 1023 kg/m^3 isopycnal (left of heavy, black dashed line) and to the 1024 kg/m^3 isopycnal (right of heavy, black dashed line).

that the residual term played an important role in slowing the rate of increase of surface temperature during mid-February to mid-May 1998. The residual cooling during April 1998 was more than double what it was during November 1997. This might be rationalized as vertical mixing and entrainment since the 1023 kg/m^3 isopycnal defining h shoaled from 130 m to 40 m depth over the 5 month period, bringing cool thermocline water closer to the surface. The surface heat flux of 50-100 W/m^2 during mid-February to mid-May (Figure 3-1) was enough to warm the surface layer temperature by 0.02-0.04°C/day, or by 1.8-3.6°C over this three month period. Although some warming of the surface layer did occur during this time, the residual term acted to cool the surface layer at a rate nearly equal to the heating by the surface flux. As a result, the net warming of SST over this period was less than would be expected from climatology (e.g., in the comparison of observed SST to the climatology of Levitus and Boyer (1994) in Figure 3-1).
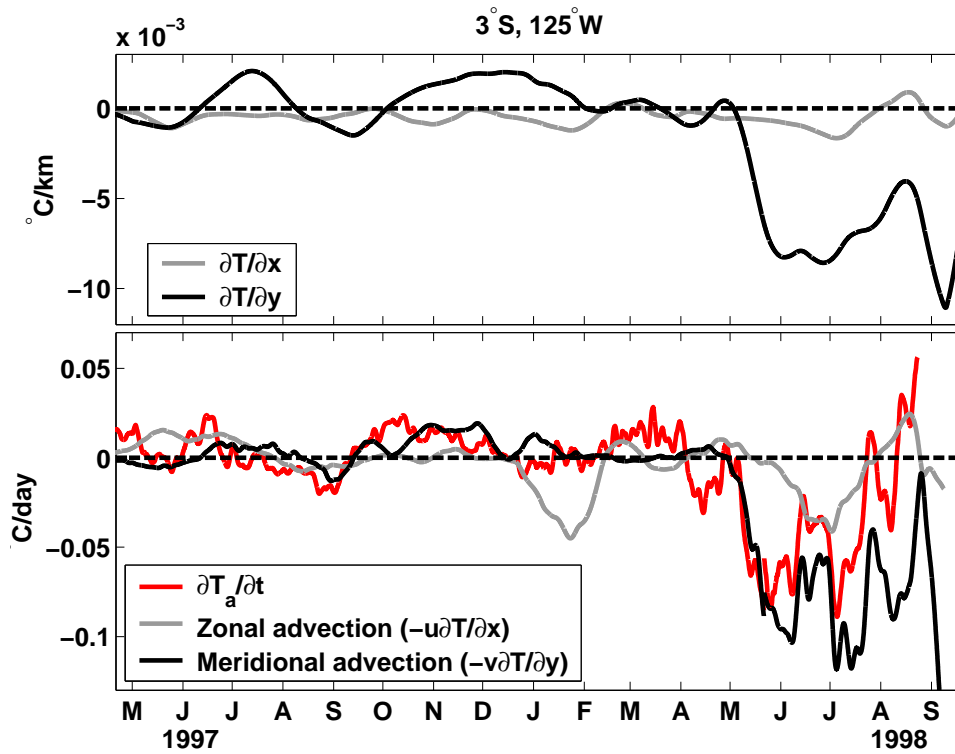
Figure 3-10: Upper panel: Zonal (grey) and meridional (black) components of the surface temperature gradient. Lower panel: Contribution of zonal (grey) and meridional (black) advection to $\partial T_a/\partial t$ (red). During the cooling period associated with the local establishment of the equatorial cold tongue after the El Niño event (May-July 1998), meridional advection exerted substantial influence on T_a.

3.3.2   Northern Site

During the 1997 ITCZ season, the surface-forcing term and the residual term were both important in setting $\partial T_a / \partial t$, with the horizontal advection term playing an increasingly important role near the end of the season (November and December of 1997). While surface forcing and the residual were both large terms during the partial record of the 1998 ITCZ season (July-September of 1998), the magnitude of the terms is about half as large as during the same time period of the 1998 season. The net heat flux during the two ITCZ seasons was comparable (Figure 3-3), so the difference between the size of the surface-forcing terms is clearly attributable to the interannual differences in the layer depth, which varied by about a factor of two between the two seasons (Figure 3-7). The difference in the residual term between the two seasons, if interpreted as vertical mixing and entrainment, is also plausibly due to this variation in h, since the entrainment and vertical turbulent flux terms are also inversely proportional to h and the diapycnal velocity is likely to be smaller when the layer base is farther from the surface.

This difference in thermocline and mixed-layer depth between the summers of 1997 and 1998 is a local expression of a large-scale pattern of thermocline-depth variability associated with El Niño (Zhang and Levitus, 1997; Perigaud et al., 2000a, b; Cassou and Perigaud, 2000; Meinen and McPhaden, 2000, 2001). This large-scale, zonally-coherent variation of thermocline depth is sometimes referred to as the "meridional tilting mode" (Meinen and McPhaden, 2000) because it involves anti-phased variations of thermocline depth between the equator and 10°N in association with ENSO[1](Alory and Delcroix, 2002). The long-recognized weakening or reversal of the North Equatorial Counter Current (NECC) in association with the transition from El Niño to La Niña (Wyrtki, 1977, 1979) is another expression of this meridional tilting mode (e.g., Farrar, 2003, p. 25). Thus, the contrast seen in the behavior of the surface-forcing term and the residual when comparing the 1997 and 1998 ITCZ seasons reflects, at least in part, differences in h associated with transition from El Niño to La Niña.

When $\partial T_a / \partial t$ is smoothed to suppress variability at periods less than three weeks, the largest variations in $\partial T_a / \partial t$ occur during the spring of 1998, with a nominal period of 50-70 days (Figure 3-11). There are energetic variations in the meridional velocity at these same

---

[1]Note that Figures 3-5 and 3-7 reflect this pattern; the thermocline depth at the two sites is out of phase.
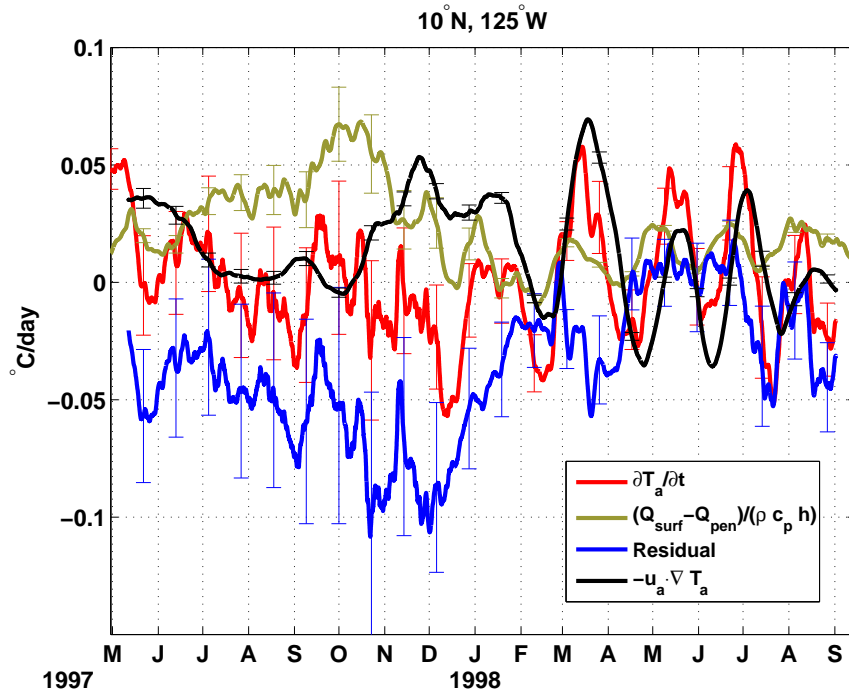
Figure 3-11: Terms in the mixed-layer temperature balance equation (Eqn. 3.5) at 10°N, 125°W. The integration was performed between the sea surface and the 1023 kg/m^3 σ_0 isopycnal.

periods during this time (Ch. 4), and the variations in $\partial T_a / \partial t$ are most nearly balanced by variations in horizontal advection (Figure 3-11). The surface temperature gradient was primarily meridional during 1998, and the variations in horizontal advection are primarily due to meridional advection (Figure 3-12). Velocity and dynamic height fluctuations at intraseasonal periods and zonal scales of 550-1650 km are characteristic of this region (Miller et al., 1985; Perigaud, 1990; Chapter 4), and the variability and the various mechanisms that may contribute to it are discussed at length in Chapter 4.

3.3.3 Interpretation of the residual

The residual of the temperature balance computation contains three terms that cannot be estimated with confidence (Equation 3.6), as well as the combined errors in the other terms. In addition, because the estimate of ∇T_a was smoothed over 49 days, the residual may contain contributions from horizontal eddy flux divergences. In previous computations of this sort, the residual has been interpreted as being representative of vertical exchange (turbulent fluxes and/or entrainment) at the base of the layer (Cronin and McPhaden, 1997; Wang
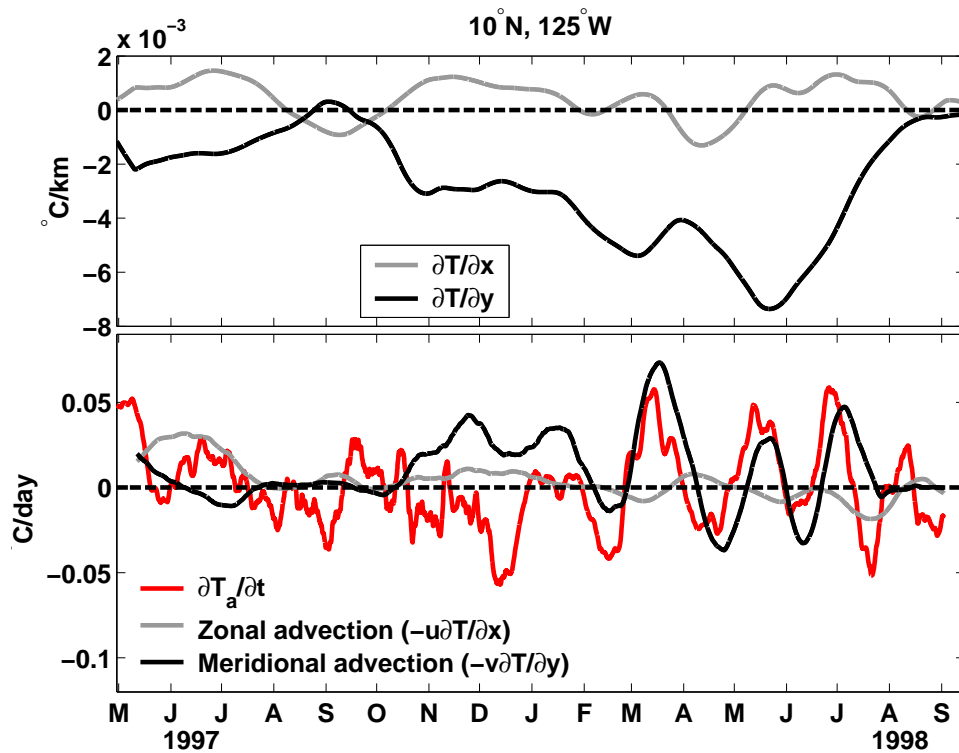
Figure 3-12: Upper panel: Zonal (grey) and meridional (black) components of the surface temperature gradient. Lower panel: Contribution of zonal (grey) and meridional (black) advection to $\partial T_a/\partial t$ (red). From about February-July 1998, meridional advection contributes prominently to the variability in $\partial T_a/\partial t$.

and McPhaden, 1999, 2001). This is reasonable since, in those studies, as in this one, the residual is generally a cooling influence on the mixed layer temperature. That the residual is almost exclusively negative or within error bars of zero suggests that the residual is not dominated by errors or the divergence term (term C in Equation 3.3) because there is no reason to expect these terms to be systematically negative. Horizontal eddy flux divergences could be, systematically or otherwise, positive or negative and thus may contribute to the observed residual.

3.4 Discussion

One clear implication of the temperature balance at the southern site is that southward advection played an important role in the local onset of La Niña conditions (or, alternatively, in the local establishment of the the equatorial cold tongue) from May-July 1998. For the three week period centered on 1 June, 1998, the average rate of cooling of T_a was 0.06 °C/day; the average rate of warming by the surface fluxes was 0.06 °C/day; the residual acted to cool T_a by 0.02 °C/day; and advection acted to cool T_a at a rate of 0.10 °C/day. It is of interest to identify the primary dynamical mechanism responsible for the southward flow that brought cool water from the north beginning in May 1998.

A likely possibility is that the resumption of the southeast trades in association with the northward migration of the ITCZ contributed to increased southward Ekman transport. This hypothesis was tested by comparing the observed V_a to $-\tau^x/(\rho f h)$, a simplistic estimate of the vertically averaged Ekman current. (τ^x is the zonal wind stress and f is the local Coriolis parameter.) The correspondence of V_a and $-\tau^x/(\rho f h)$ is remarkably good, with both quantities changing by about 20 cm/s during May 1998 (Figure 3-13). This constitutes strong evidence that the rapid acceleration of southward flow during April and May of 1998 was due to an increase in the westward wind stress.

It is not obvious that the value of h used in calculation of the temperature balance is the appropriate choice for this estimate, especially because the appreciable size of the residual in the temperature balance suggests the existence of turbulent heat fluxes (and probably momentum fluxes) across the base of the layer. Even so, the fact that the depth h is near the top of a sharp pycnocline (typically within about 10-30% of h) leads us to expect that vertical turbulent heat and momentum transport should decay rapidly at depths larger than
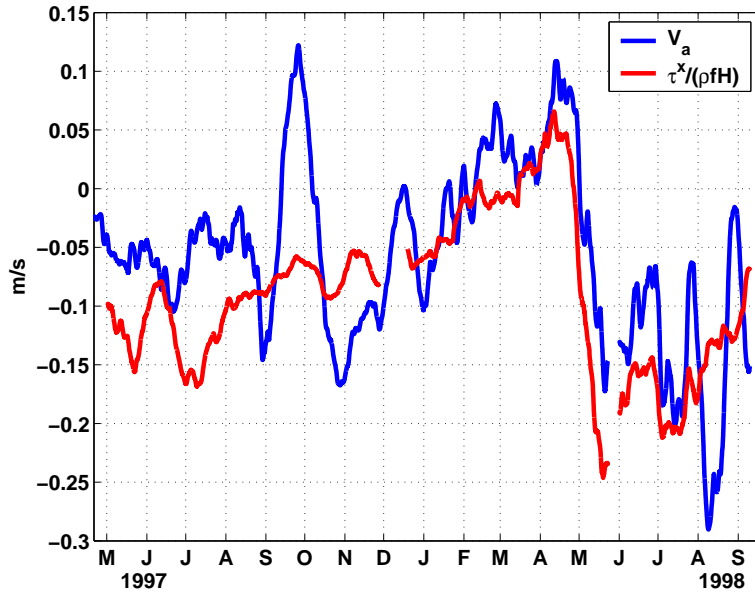
Figure 3-13: Comparison of the observed, depth averaged meridional current at the southern site to $-\tau^x/(\rho f h)$, the value of the vertically averaged meridional Ekman current expected if the current is confined above the depth h. The temperature balance suggests that there was mixing across the depth h during and after the boreal spring of 1998, so there was likely also mixing of momentum across this depth. However, the vertical turbulent momentum transport is expected to decay rapidly with depth below h (in the main pycnocline), so that h is expected to be roughly representative of the depth where the Ekman current vanishes.

h. Thus, h is likely a good approximation to the depth where the turbulent momentum flux becomes very small. The near correspondence of V_a with $-\tau^x/(\rho f h)$, taken together with the results of the temperature balance calculation, suggests that southward Ekman transport, as the trades resumed near the end of the El Niño event, was vital to the development of La Niña conditions at this off-equatorial site.

At the northern site, intraseasonal variability was present in SST, surface heat flux, and upper-ocean currents during roughly the first half of 1998. The mixed-layer temperature balance suggests that the intraseasonal signal in SST results primarily from horizontal advection. The surface heat flux signal is too weak to account for the size of the variations in $\partial T_a/\partial t$ (Figure 3-11), and intraseasonal variations in the surface heating term are not in phase with those of $\partial T_a/\partial t$ (particularly during March-July 1998). These factors suggest that the intraseasonal signal in the surface heat flux may be a response to the SST variations caused by horizontal advection.

SST variations can be either the cause or the result of surface heat flux variations (e.g., Frankignoul et al., 1998). To the extent that SST is merely a response to surface heat
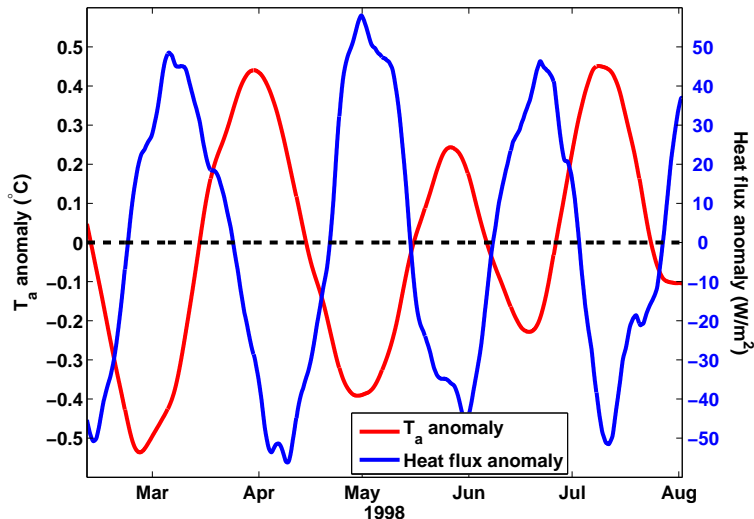
Figure 3-14: 21-81 day band-pass filtered T_a (red line) and net surface heat flux (blue line).

flux variations, SST should be in quadrature with Q. On the other hand, if Q responds to variations in SST, serving as a negative feedback on SST, one might expect the phase relationship of Q and SST to be 180°.

The phase relationship observed between T_a and Q at intraseasonal periods supports the notion that the intraseasonal surface heat flux signal is a response to SST variations caused by horizontal advection. To clarify this relationship, time series of Q and T_a have been filtered to pass variability with 21-81 day periods. During March-July 1998, these band-passed time series of Q and T_a are roughly out of phase, suggesting that variations in T_a may be causing variations in Q (Figure 3-14).

It is illuminating to examine how the different components of the net heat flux contribute to the observed intraseasonal variation in Q by examining band-passed versions of the individual components of the heat flux. Variations in latent heat flux are important in producing the observed intraseasonal variation in Q, contributing roughly 25 W/m² to the signal (Figure 3-15). Surprisingly, though, variations in the net solar radiation contribute comparably to the signal in Q. There is clearly an intraseasonal signal in the sensible heat flux, but its amplitude is small, only a few W/m². The band-passed net longwave heat flux shows no obvious relation to the signal in T_a or Q.

Modulation of the net solar radiation suggests a modulation of atmospheric cloud or water vapor properties. The rest of this thesis examines the intraseasonal variability at the northern
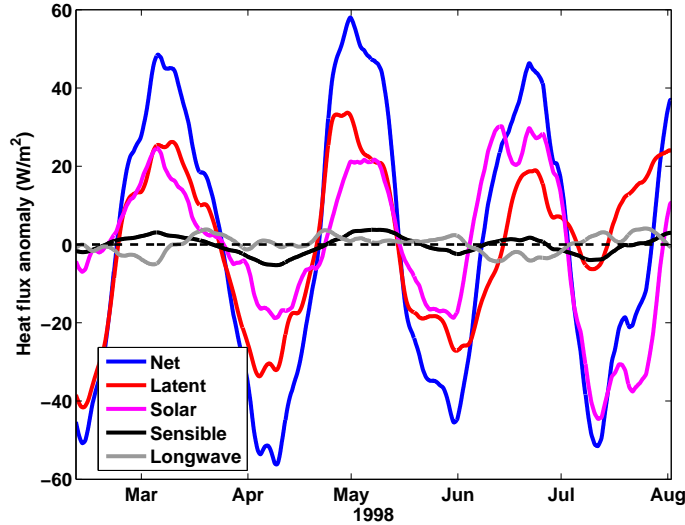
Figure 3-15: 21-81 day band-pass filtered heat flux components at the northern mooring site.

site. Chapter 4 focuses on the intraseasonal velocity signal, characterizing the signal observed at the mooring within its larger spatial and temporal context. There, it is shown that the intraseasonal velocity signal influencing SST can be ascribed to oceanic Rossby waves with a zonal wavelength of about 550 km and a phase speed of roughly 10 cm/s. That atmospheric convection could be systematically affected by such a slow, small-scale (in comparison to the atmospheric synoptic scale) disturbance is unanticipated and warrants closer inspection. This relationship between oceanic Rossby waves and atmospheric convection is explored further in Chapter 5 using satellite observations of SST and cloud properties.

Appendix: Sensitivity to errors

Uncertainty in estimates of the terms in Equation 3.5 derives from three interrelated types of error: instrumental error (e.g., errors in T), sampling error (e.g., errors in $T(z)$ associated with discrete vertical sampling), and errors in derived quantities (e.g., isopycnal depth and penetrating solar radiation). Care has been taken to ensure that systematic instrumental errors have been identified and removed to the extent possible by pre- and post-deployment calibration and in situ sensor inter-comparison (Anderson et al., 2000), so instrumental errors will be assumed random for this analysis. We estimate the error of each term in Equation 3.5 based on the theory of propagation of errors (e.g. Young, 1996). The error of a quantity

$Q = Q(a, b, c, ...)$ computed from the measured quantities $(a, b, c, ...)$ is given by

$$\Delta Q = \frac{\partial Q}{\partial a}\Delta a + \frac{\partial Q}{\partial b}\Delta b + \frac{\partial Q}{\partial c}\Delta c + ... \tag{3.8}$$

Lacking knowledge of systematic correlations between terms on the right-hand-side, we operate under the pessimistic assumption that error contributions at a given time are correlated in the worst possible way. Thus, each error contribution is assumed to have the same sign on the right-hand-side in Equation 3.8 and in the other equations involving addition of errors below.

The error in T_a is consequently,

$$\Delta T_a = \frac{\Delta T}{\sqrt{\tilde{N}_T}} + \hat{T}|_{-h}\frac{\Delta h}{h}, \tag{3.9}$$

where the temperature measurement errors are assumed to be uncorrelated in depth and the calculus identity $\frac{d}{dx}\int_{u(x)}^{0} f(t)dt = -f(u)\frac{du}{dx}$ has been employed. $\tilde{N}_T$ is a number less than the number of temperature sensors used to compute the vertical average. ($\tilde{N}_T$ would equal the number of temperature sensors used if the vertical spacing of sensors were uniform. That $\tilde{N}_T$ is less than the number of sensors has to do with the fact that T_a is a weighted average rather than an arithmetic mean of the temperatures measured by the sensors.)

Similarly, the estimated error in $\vec{u}_a$ is

$$\Delta u_a = \frac{\Delta u}{\sqrt{\tilde{N}_u}} + \hat{u}|_{-h}\frac{\Delta h}{h}, \tag{3.10}$$

$$\Delta v_a = \frac{\Delta v}{\sqrt{\tilde{N}_u}} + \hat{v}|_{-h}\frac{\Delta h}{h}. \tag{3.11}$$

Equations 3.9-3.11 each express two types of contributions to the uncertainty in the vertical average. The first source of uncertainty is associated with instrumental errors; the second is associated with imprecise knowledge of the integration depth, h. This second source of uncertainty expresses the fact that if the temperature or velocity at $z = -h$ deviates substantially from the vertical average value, then a relatively small error in h could cause a large error in the estimated vertical average value.

Since h is time-dependent, the number of sensors above the depth h is also time depen-

dent. Because the depth h is chosen to be the depth of an isopycnal in the upper pycnocline (near strong gradients of T and $\mathbf{u}_a$), the error in the vertical average associated with instrumental error is negligible compared to the error associated with uncertainty in h, even if $\tilde{N}$ (i.e. $\tilde{N}_T$ or $\tilde{N}_u$) is taken to be one. For convenience, the $\tilde{N}$'s are conservatively taken to be equal to one in estimating the error in depth averaged temperature and velocity.

The error in the term of Equation 3.5 involving surface heating and penetrating solar radiation is (denoting this term by F)

$$\Delta F = F\frac{\Delta h}{h} + \frac{\Delta Q_H + \Delta Q_s(1 - Ae^{-\gamma_1 h} - (1 - A)e^{-\gamma_2 h}) + \Delta h Q_s(\gamma_1 Ae^{-\gamma_1 h} + \gamma_2(1 - A)e^{-\gamma_2 h})}{\rho c_p h},$$
(3.12)

where Q_s is the net surface solar radiation and Q_H is the rest of the surface heat flux. If random error in the solar extinction coefficients (γ_1 and γ_2) and the associated parameter A is accounted for, the error in F contains the additional terms

$$\Delta F = \frac{Q_s Ae^{-\gamma_1 h}}{\rho c_p}\Delta\gamma_1 + \frac{Q_s(1 - A)e^{-\gamma_2 h}}{\rho c_p}\Delta\gamma_2 + \frac{Q_s(e^{-\gamma_2 h} - e^{-\gamma_1 h})}{\rho c_p h}\Delta A.$$
(3.13)

While parameterization of the penetration of solar radiation by a double-exponential decay profile is expected to be adequate given an appropriate choice of parameters, the appropriate parameters is expected to be variable and the particular choice made here may be systematically in error. Since systematic errors are correlated in time, averaging does not reduce their magnitude. Thus, the most important errors in the estimate of penetrating solar radiation are likely to be systematic ones associated with poor choice of parameters for the double-exponential decay parameterization. These errors are accounted for by adding another term to the error in the term associated with surface heating and penetrating solar radiation that is, in form, identical to Equation 3.13:

$$\Delta F_{sys} = \frac{Q_s Ae^{-\gamma_1 h}}{\rho c_p}\Delta\gamma_{1,sys} + \frac{Q_s(1 - A)e^{-\gamma_2 h}}{\rho c_p}\Delta\gamma_{2,sys} + \frac{Q_s(e^{-\gamma_2 h} - e^{-\gamma_1 h})}{\rho c_p h}\Delta A_{sys},$$
(3.14)

where the subscript "sys" indicates a systematic error.

The errors in zonal and meridional advection are, respectively,

$$\Delta A_x = T_x \Delta u_a + u_a \Delta T_x,$$
(3.15)

$$\Delta A_y = T_y \Delta v_a + v_a \Delta T_y, \tag{3.16}$$

Under the assumption that errors in a given term are normally distributed and uncorrelated in time, the error in the temporal average of each estimated term (excluding $\partial T_a / \partial t$; see below) is taken to be reduced by a factor of $\sqrt{N}$, where N is the number of points used in the computation of the time-average. This assumption is probably overly optimistic. However, the error at each time is estimated under the pessimistic assumption that individual error sources are correlated in the worst possible way (i.e., using a sum-of-absolute-values rather than a sum-of-squares approach), so that the combination of these pessimistic and optimistic assumptions may effectively compensate one another. In any case it is encouraging that the envelope of the error bars for each term typically covers the high frequency "jitters" in the smoothed estimates, suggesting that the estimated uncertainty is close to the true uncertainty. Note that this error estimate is substantially more pessimistic than the error estimates used in other studies making estimates of the terms in Equation 3.5 (e.g. Cronin and McPhaden, 1997, Wang and McPhaden, 2000).

Because $\partial T_a / \partial t$ is computed as a finite difference, there is systematic error cancellation in this term when the estimate is averaged in time. If ΔT_a were constant in time, the (worst case) error in $\partial T_a / \partial t$ would be,

$$\Delta T_{at} = \frac{3}{2} \frac{\Delta T_a}{N \Delta t}, \tag{3.17}$$

where the factor of $3/2$ comes from the use of a fourth-order centered difference scheme in calculating $\partial T_a / \partial t$. (It would be a factor of 2 if a two-point centered difference were used.) Averaging reduces the error in this term by more than a factor of $\sqrt{N}$ because the differencing operation leads to systematic cancellation of errors (rather than a random cancellation). The temporal variability of ΔT_a is accounted for here by using a temporally smoothed value in Equation 3.17.

The values of the error inputs are given in Table 3.4.

Error parameter	Symbol	Value
Temperature sensor error	ΔT	0.01°C
Current meter error	ΔU, ΔV	3 cm/s
Isopycnal depth error (relative)	$\frac{\Delta h}{h}$	10 %
Horizontal ∇T_a error*	ΔT_x, ΔT_y	2×10^{-6} °C/m
Surface heat flux error (all but solar)	ΔQ_H	7 W/m^2
Surface heat flux error (solar)	ΔQ_s	20 W/m^2
Error in proportion of shortwave/longwave in Q_s	ΔA	0.15 (25%)
Error in solar shortwave decay constant	$\Delta \gamma_1$	1 m^{-1} (60 %)
Error in solar longwave decay constant	$\Delta \gamma_2$	0.03 m^{-1} (60 %)
Systematic error in proportion of shortwave/longwave in Q_s	ΔA	0.1 (20%)
Systematic error in solar shortwave decay constant	$\Delta \gamma_1$	1 m^{-1} (60 %)
Systematic error in solar longwave decay constant	$\Delta \gamma_2$	0.03 m^{-1} (20 %)

Table 3.1: Table of error estimates used as inputs to the error propagation formulas given in this appendix. *The satellite SST measurements were averaged over a 3×3 grid-cell area prior to computation of the gradient, decreasing the error in SST from that given in the data documentation.

Chapter 4

Intraseasonal Variability near 10°N in the Eastern Tropical Pacific Ocean[1]

Abstract

New in situ observations from 10°N, 125°W during 1997-1998 show strong intraseasonal variability in meridional velocity and sea surface temperature. 50- to 100-day oscillations in sea surface height (SSH) have long been recognized as a prominent aspect of oceanic variability in the region of 9-13°N in the eastern Pacific Ocean. We use in situ and satellite data to more fully characterize this variability. The oscillations have zonal wavelengths of 550-1650 km and propagate westward in a manner consistent with the dispersion relation for first baroclinic mode, free Rossby waves in the presence of a mean westward flow. Analysis of 9 years of altimetry data shows that the amplitude of the 50- to 100-day SSH variability at 10°N is largest on 90-115°W, with peak amplitudes occurring around April. Some eddies traveling westward at 10-13°N emanate from near the Gulfs of Tehuantepec and Papagayo, but eddies sometimes also appear to intensify well away from the coast while in the North Equatorial Current (NEC). The hypothesis that the intraseasonal variability and its annual cycle are associated with baroclinic instability of the NEC is supported by a spatio-temporal correlation between the amplitude of 50- to 100-day variability and the occurrence of westward zonal flows meeting an approximate necessary condition for baroclinic instability. The notion that baroclinic instability may be involved is further corroborated by the tendency of the NEC to weaken while the eddies intensify, even as the wind works to strengthen the current.

---

[1]This chapter contains contributions from a co-author, Robert Weller, and was published in the *Journal of Geophysical Research*. See the citation for Farrar and Weller (2006). The right to reproduce the content of this article here was retained by the authors when the American Geophysical Union was granted (non-exclusive) copyright.

4.1 Introduction

The region near 10°N in the eastern tropical Pacific Ocean is characterized by strong intraseasonal (50- to 100-day period) sea level fluctuations; Miller et al. (1985) deployed a meridional array of five inverted echo sounders extending from the equator to 9°N along 110°W and found energetic 60- to 80-day dynamic height variability with an amplitude of roughly 10 dyn cm (comparable to the meridional change in dynamic height across the NECC) at the northern end of this array. There are indications of annual period variability in the strength of this intraseasonal variability; in the 14-month dynamic height time series, the oscillations were observed to be strongest during February-August (Miller et al., 1985), and subsequent studies using 1-2 years of satellite altimetry data have found the variability to be strongest during roughly the first half of the year with a maximum amplitude near 10-13°N in the eastern tropical Pacific (Perigaud, 1990; Giese et al., 1994).

Strong intraseasonal velocity variability can play a role in air-sea coupling by setting the local SST and its gradient field and by effecting meridional heat transport. Near-surface meridional velocities, acting along the mean SST gradient, can cause substantial modulation of the local SST, and eddy transports can contribute to the meridional heat transport in the region. Zhurbas and Oh (2004) attributed elevated levels of eddy diffusivity in the eastern Pacific warm pool to heightened levels of mesoscale oceanic variability. Fluctuations in strong meridional temperature gradients can also affect the atmospheric boundary layer. The intraseasonal fluctuations in SST observed near 10°N are likely to modulate surface turbulent heat fluxes as has been noted to occur in the tropical instability wave region (Zhang and McPhaden, 1995; Thum et al., 2002), and the SST signatures associated with eddies in the eastern Pacific warm pool (e.g., Raymond et al., 2004) may be sufficient to affect atmospheric deep convection. Recent studies have also shown that intensification of tropical cyclones is influenced considerably by oceanic mesoscale SST variability (Shay et al., 2000; Hong et al., 2000; Kaplan and DeMaria, 2003), and this effect is likely to be important in the eastern tropical North Pacific, one of the world's most prolific regions of cyclogenesis. Thus, not only should the space-time nature of the energetic intraseasonal fluctuations of temperature and velocity be considered when sampling the region, but they should be considered to have potential impact on the simulation of weather and climate.

While there is consensus that strong intraseasonal variability exists near 10°N in the

eastern tropical Pacific, a comprehensive description of this variability is lacking. This inhibits understanding of the causes and consequences of this energetic signal. The two studies that have examined the signal over broad spatial and temporal domains (Perigaud, 1990; Giese et al., 1994) have arrived at contradictory conclusions regarding the properties and likely generating mechanisms of the variability. While the two studies found similar phase speeds for the variability, different conclusions were reached about the origin of the sea surface height (SSH) fluctuations and the zonal direction of energy propagation. Giese et al. (1994) argued that the fluctuations are due to anticyclonic eddies forced by episodic wind bursts across the Gulfs of Tehuantepac and Papagayo, while Perigaud suggested that the fluctuations may be due to instabilities associated with the meridional shear of the NECC and NEC. Perhaps more importantly, the two studies seem to disagree as to the nature of the fluctuations. Giese et al. argued that the motions are associated with isolated eddies that are locally forced at the eastern boundary by quasi-periodic wind events and then propagate westward, losing energy and decaying below detection threshold by about 120°W. Localized forcing at the eastern boundary implies westward energy propagation. In contrast, Perigaud treated the motions as waves (albeit nonlinear ones), and estimated the group velocity to be eastward at about 10 km/day. Perigaud's (1990) inference of eastward energy propagation is inconsistent with the eastern boundary forcing mechanism proposed by Giese et al. (1994).

Many studies have considered oceanic variability at scales of up to 1500 km in the eastern Pacific warm pool region using theoretical, numerical, or observational techniques. However, except for the work of Miller et al. (1985) and Perigaud (1990), these studies have not attempted to quantify the periodicity of the variability so it is not entirely clear whether all of these studies are relevant to the intraseasonal variability. The mountain gap winds at the Gulfs of Tehuantepac and Papagayo are thought to force eddies that propagate westward (or southwestward) at speeds of about 13-17 cm/s (Stumpf and Legeckis, 1977; Giese et al., 1994; Ballestero and Coen, 2004). These eddies may be forced linearly by fluctuations in the strong mountain gap winds or nonlinearly by the annually varying winds that apply strong vorticity forcing (Yamagata et al., 1991; Umatani and Yamagata, 1991). Perigaud (1990) examined the possibility of barotropic instability in the region but did not reach any strong conclusion, and Philander (1976) suggested that the North Equatorial Current (NEC) may be baroclinically unstable. Hansen and Maul (1991) have argued that the strong anticyclonic eddies observed in the region with surface drifters result from retroflection of the North

59

Equatorial Counter Current (NECC) at the eastern boundary. In this hypothesis, upon contact with the eastern boundary, water from the NECC moves northward to about 11°N where it takes on anticyclonic relative vorticity to conserve potential vorticity and propagates westward under the influence of the planetary vorticity gradient. Another plausible source of intraseasonal variability near 10°N is the intraseasonal coastal Kelvin wave variability in the region (Spillane et al., 1987; Enfield, 1987), which may radiate Rossby waves to the west. Some authors have interpreted the literature on this variability as evidence of distinct types of variability (e.g. Weidman et al., 1999) while others have treated the different observational studies as evidence of a single type of intraseasonal variability (e.g. Giese et al., 1994). The various theories for the strong intraseasonal variability on 10-13°N can be grouped into four classes: (1) mountain gap wind forcing of intraseasonal eddies, either by fluctuating or seasonally varying winds, (2) instability of the zonal equatorial currents, either by barotropic instability (involving the NEC/NECC shear) or baroclinic instability (involving the vertical shear of the NEC), (3) NECC retroflection, and (4) radiation of Rossby waves (or similar westward propagating variability) from the intraseasonal coastal Kelvin waves that exist on the eastern boundary. The present study seeks to develop a more complete characterization of the intraseasonal variability near 10°N in the eastern tropical Pacific by drawing on both in situ and satellite data.

In this chapter, we analyze in situ current and dynamic height data, satellite SST, and satellite altimetry to gain further insight into the energetic intraseasonal oscillations along 10°N in the eastern tropical Pacific. This chapter is organized as follows: Section 4.2 provides an overview of the data used, and Section 4.3 gives a qualitative description of the intraseasonal fluctuations as seen in in situ data and examines the effects of the variability on SST. Section 4.4 uses satellite SST and satellite altimetry to complete this description and set the broader spatial and temporal context. Section 4.5 quantifies basic properties of the variability, such as its wavelength, frequency, and dispersion relation. Section 4.6 discusses the interpretation of the intraseasonal oscillations as Rossby waves and the generation mechanisms for the variability. Finally, Section 4.7 offers some concluding remarks.

Pacific climatological SST
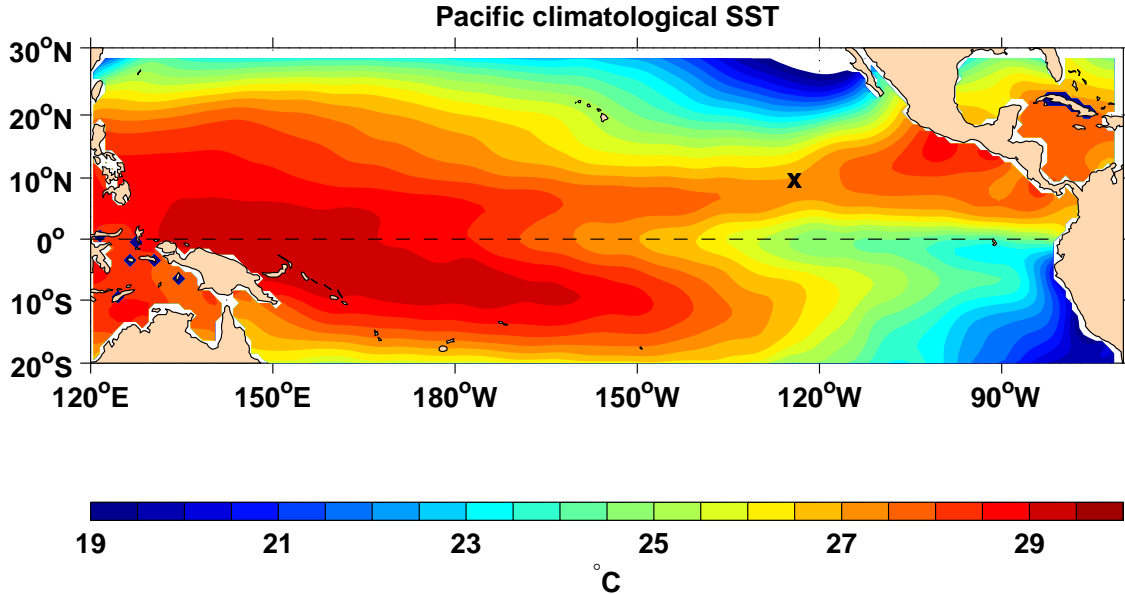
Figure 4-1: Mean SST of the tropical Pacific (Levitus and Boyer, 1994). The location of the mooring is indicated by an 'x' at 10°N, 125°W.

4.2   Data

In addition to data from the PACS mooring near 10°N, 125°W (Figure 4-1), this study makes use of Version 3 of the 0.5°, 5-day binned SST from the Advanced Very High Resolution Radiometer (AVHRR) on the NOAA polar orbiting satellites distributed in association with the World Ocean Circulation Experiment (WOCE). For quantitative spectral calculations involving altimetry data, we use the WOCE Version 3 0.5°, 10-day binned TOPEX/Poseidon SSH anomaly data set. We use the WOCE Version 3 1°, 5-day gridded and interpolated TOPEX/Poseidon SSH anomaly data set for display purposes (i.e., in figures showing SSH anomaly) and when computing SSH anomaly gradients. The SSH anomaly and SST products used here and details regarding their processing can be obtained from the NASA JPL Physical Oceanography Distributed Active Archive Center web site at "http://podaac.jpl.nasa.gov/woce/". For all calculations utilizing the AVHRR SST data, gaps caused by clouds were filled by linear interpolation in time. This approach was chosen because the data gaps typically span fewer data points in time than in space, lasting for times comparable to atmospheric synoptic timescales.

We also employ the Bonjean and Lagerloef (2002) tropical Pacific surface current analysis to understand the spatial and temporal context of the low frequency (seasonal timescale) currents measured at the mooring site. These investigators used a diagnostic model incor-

porating geostrophic, Ekman, and thermal wind dynamics to estimate the surface currents (15 m depth) from SSH anomalies, SST, surface winds, and mean dynamic topography. It is noteworthy that the Bonjean and Lagerloef analysis does show an intraseasonal signal at the mooring site that is in phase with the observed signal; however, the amplitude of the signal is too small during the spring of 1998, presumably because the objectively analyzed, $1° \times 1°$ version of the TOPEX/Poseidon data used for their analysis further smooths the $5°$ signal (Section 4.5) that is already only marginally resolved in TOPEX/Poseidon data, which has a zonal track separation of up to 316 km. Although intraseasonal variability in the currents at the mooring site is not adequately represented in the surface current analysis, the Bonjean and Lagerloef (2002) currents seem to give a faithful representation of the zonal current at lower frequencies. For example, the mean zonal current in the Bonjean and Lagerloef (2002) analysis at the mooring site during the mooring deployment differs from the in situ mean at 15 m depth by only 1.1 cm/s. Given the strong intraseasonal variability and the relatively short 17 month mooring record, this agreement may be fortuitous, but, for lack of a better estimate, we will use the Bonjean and Lagerloef (2002) surface currents when considering the spatial and temporal variability of the low frequency zonal currents.

We will discuss a number of period bands in this paper. The period band of interest is 50-100 days, but when working with the relatively short 504 day mooring record, it is sometimes impractical to examine the full 50-100 day period band. This is especially true when performing band-pass filtering or spectral computations on the mooring data. When band-pass filtering the mooring data, we face a tradeoff in selection of low-frequency cutoff for the pass-band. A lower frequency cutoff passes more intraseasonal energy, but also shortens the useful length of the band-passed record. This tradeoff motivates our choice of pass-band low frequency cutoffs, which will be chosen according to circumstance. We choose the high frequency cutoff to be as high as possible while still suppressing energy in the internal wave and atmospheric weather bands in order to make the pass-band as broad as possible to avoid unwanted distortions by a narrow band filter. All data filtering is done with a moving average filter. When performing spectral calculations on the mooring data, the "intraseasonal band" is dictated by the record length and the amount of averaging required to obtain statistically meaningful results.

4.3 Intraseasonal variability at the mooring

For comparison with the dynamic height observations of Miller et al. (1985) at 9°N, 110°W, we computed the steric height of the water column between 10 and 110 m depths using the temperature and salinity data from the mooring. Due to conductivity sensor failures during the first phase of the field program, the salinity at depths where no data were available was estimated by linear regression between observed temperature and salinity. The 20° isotherm (a proxy for the center of the thermocline) was always shallower than 110 m, so the 10-110 m depth interval covers a substantial fraction of the density difference over the water column. The steric height, filtered to pass 21-91 day variability, is shown in Figure 4-2. While the amplitude of the steric height signal, computed between 10 and 110 m depths, cannot be quantitatively compared to the full water column dynamic height observations of Miller et al. (1985), the seasonal modulation of the signal is remarkably similar to that observed by Miller et al. (1985), with the strongest intraseasonal variability occurring between January and August 1998. The period of the oscillations can be seen to be about two months from October 1997 to June 1998, and the oscillations rapidly intensify during the first few months of 1998. The amplitude of the oscillations approximately doubles between December 1997 and February 1998, and it doubles again between February and April 1998. At its peak strength in April 1998, the signal is associated with nearly a 7 cm peak-to-peak change in the thickness of the upper 110 m of the water column.

Strong intraseasonal current fluctuations are evident within the mixed layer and are coincident with the signal in steric height (Figures 4-3 and 4-4). A ten-day averaging period was chosen to emphasize the sub-inertial variability, as the inertial period is about 2.87 days at 10°N. Above the thermocline, intraseasonal variability was found in the zonal currents as well as in the meridional currents. However, the upper-ocean zonal and meridional currents are not significantly coherent at intraseasonal frequencies. Below the thermocline, zonal and meridional velocity components are also incoherent at sub-inertial frequencies. The meridional velocity (Figure 4-4) shows strong oscillations with a period of about two months during November 1997 to July 1998. While the sub-thermocline meridional velocity clearly exhibits a quasi-periodic signal with a period of roughly two months between November and July, the zonal velocity is dominated by lower frequency variability, as can be seen in the velocity time series from the deepest current meter at 110 m depth (Figure 4-5). Aside
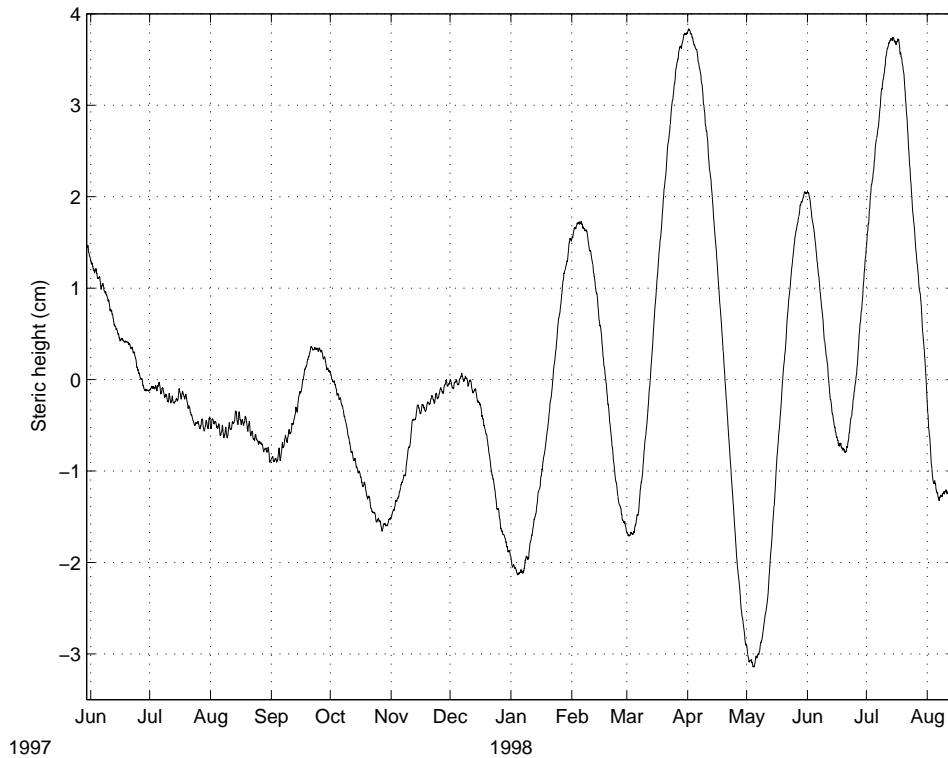
Figure 4-2: 21-91 day bandpassed steric height at 10 m relative to 110 m. Edge effects in the filtering contaminate the signal prior to August 1, 1997 and after June 15, 1998.

from two periods of strong near-surface zonal currents in May 1997 and July 1998, the low frequency meridional currents are comparable in size to the zonal currents above the thermocline; both are typically 10 to 20 cm/s (Figure 4-4). The westward velocity signal observed during May/June 1997 was associated with the passage of an anticyclonic eddy that approached from the east (shown in Section 4.6.2); the peak velocity signal associated with this eddy was 40-50 cm/s in the upper 40 m and more than 15 cm/s at 110 m.

The non-stationarity of the intraseasonal oscillations is evident, and conventional spectral analysis of the time series does not recover a discrete, statistically significant spectral peak associated with them. To better quantify the temporal evolution of the energy levels at different periods we used the wavelet power spectrum. Figure 4-6 shows the wavelet power spectrum for the meridional velocity at 110 m (10°N, 125°W) computed using a Morlet wavelet following Torrence and Compo (1998). In the figure, the parabola-like yellow line indicates the cone of influence; below this curve, edge effects may contaminate the spectrum (Torrence and Compo, 1998). This analysis reveals a distinct spectral peak that transitions from a period near 85 days in October/November 1997 toward a period near 50 days by June

64
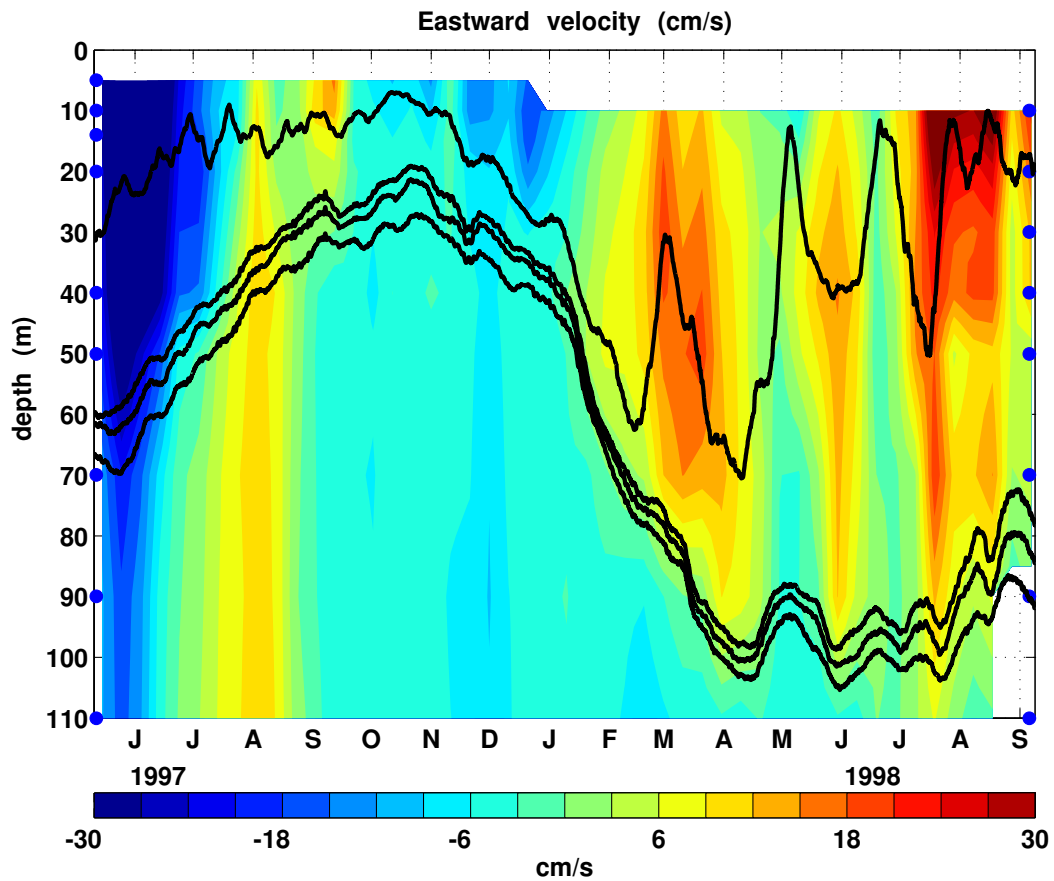
Figure 4-3: Depth-time plot of 10-day averaged zonal velocity at 10°N, 125°W. Current meter locations during the two deployments are indicated by blue dots on the left and right edges of the figure. The upper black line indicates the mixed layer depth (where the temperature is 0.1°C less than its surface value) and the lower three black lines are isotherms in the upper half of the thermocline (19, 22, and 24°C isotherms). Mixed-layer depth and isotherms are 10-day running averages.
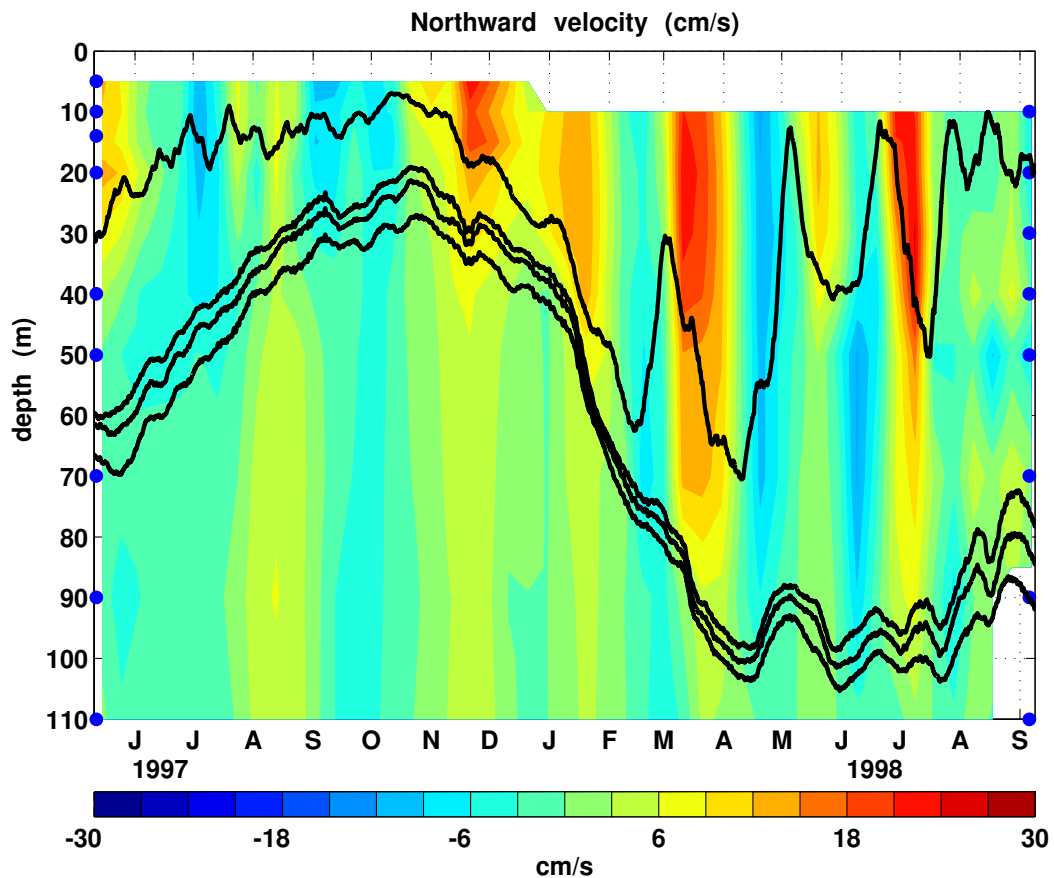
Figure 4-4: Depth-time plot of 10-day averaged meridional velocity at 10°N, 125°W. Current meter locations during the two deployments are indicated by blue dots on the left and right edges of the figure. The upper black line indicates the mixed layer depth (where the temperature is 0.1°C less than its surface value) and the lower three black lines are isotherms in the upper half of the thermocline (19, 22, and 24°C isotherms). Mixed-layer depth and isotherms are 10-day running averages.

66
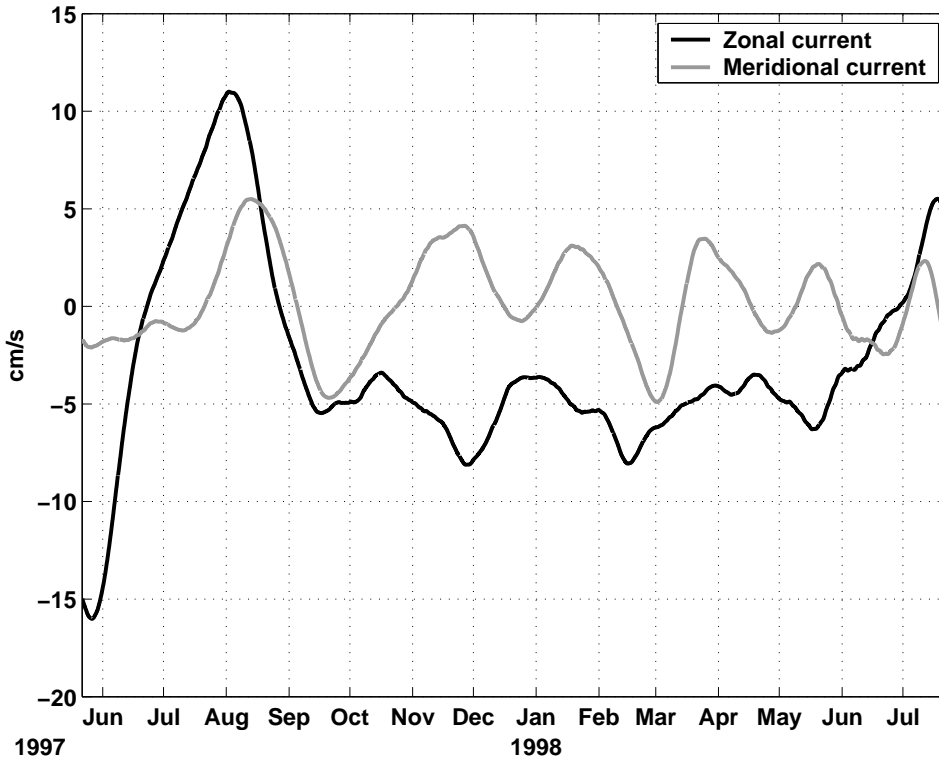
Figure 4-5: Zonal and meridional velocity components at 110 m depth. Both time series have been smoothed by two successive applications of an 11-day moving average filter.

1998 (Figure 4-6).

The intraseasonal velocity fluctuations at the mooring site were accompanied by substantial fluctuations in SST during part of the observational record. While this coherence of SST and meridional velocity is apparent in the raw data, the relationship is more readily apparent when comparing the 20-70 day bandpassed meridional velocity at 10 m depth and the 20-70 day bandpassed SST (25 cm depth) from the mooring site (Figure 4-7). From January to June of 1998, there is a signal in SST with an amplitude of 0.2-0.4°C. These observations are reminiscent of the work of Leeuwenburgh and Stammer (2001), who found significant correlations of SST and the ocean eddy/wave field on timescales as short as one month and attributed these correlations to advection by the geostrophic eddy/wave field.

The peak-to-peak change in SST associated with this signal was observed to exceed 0.8°C at the mooring site, so it is of interest to determine the extent to which horizontal advection can account for the signal. The evolution of temperature is governed by conservation of heat, given approximately by

$$\frac{\partial T}{\partial t} = \frac{\nabla \cdot \vec{q}}{\rho c_p} - (\vec{u} \cdot \nabla T) \tag{4.1}$$

67
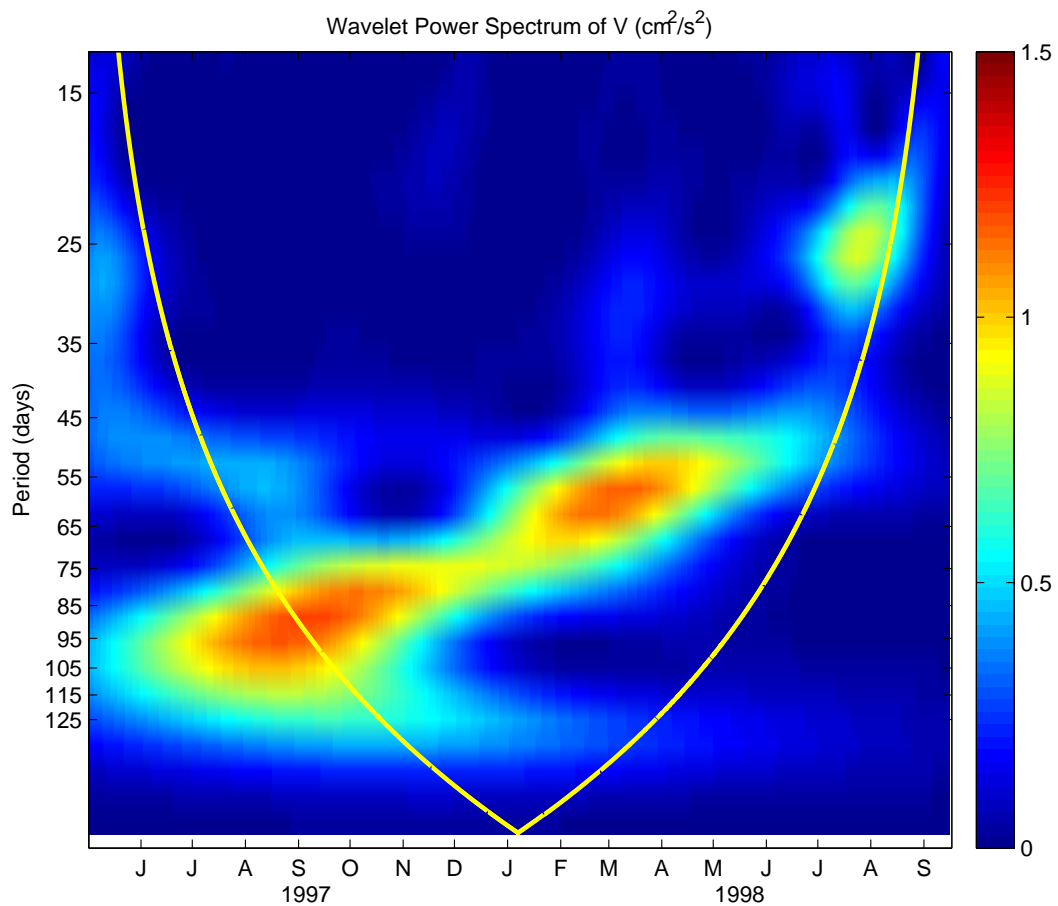
Figure 4-6: Wavelet power spectrum of the meridional velocity at 110m (cm^2/s^2). The solid yellow curve indicates the cone of influence; below this curve edge effects potentially contaminate the results.
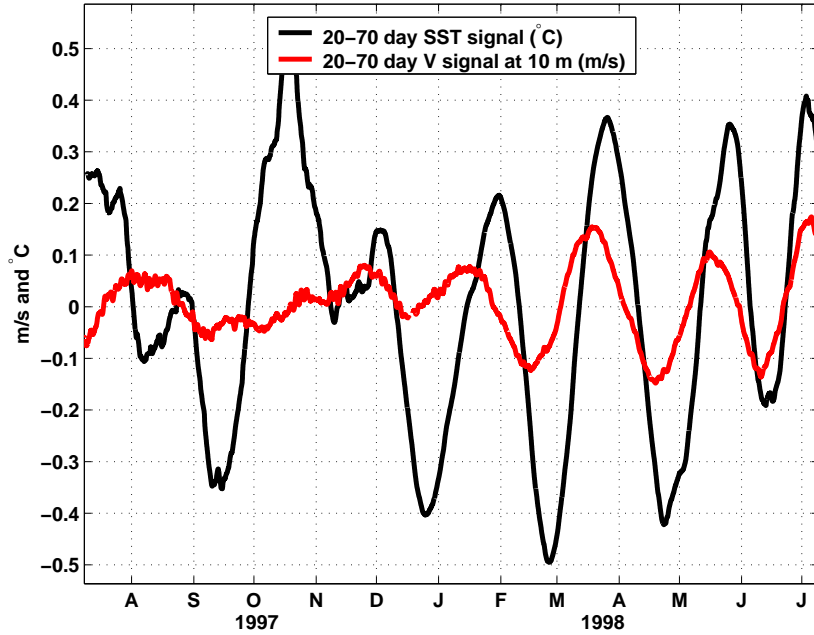
Figure 4-7: SST and 10 m velocity from a mooring at 10°N, 125°W, filtered to pass 20-70 day variability.

where ρ is the density of seawater, c_p is the specific heat, and $\vec{q}$ is the turbulent and radiative heat flux. To understand the balance of processes that set SST, the typical procedure is to combine the equations of heat and mass conservation and integrate vertically over the mixed layer (e.g., Cronin and McPhaden, 1997). However, since our primary interest here is in understanding the effect of horizontal advection on SST, we examine the balance of the tendency of SST with the advection term directly.

We carried out the analysis at 10 m depth, since this is the shallowest depth where both temperature and currents are available for both phases of the field program. We estimated the horizontal surface temperature gradient, ∇T, at 5-day resolution by a fourth-order-accurate centered difference scheme using the WOCE Version 3 AVHRR SST product and linearly interpolated the $0.5° \times 0.5°$ field to the mooring location. This type of approach to estimating ∇T is believed to provide a reasonably accurate estimate of the mixed layer horizontal temperature gradient (Wang and McPhaden, 1999, 2001). To suppress noise in the ∇T estimate due to measurement error and unresolved variability in the SST field and its subsequent amplification in the discretized derivative, we smoothed the ∇T estimate in time with an 11-point (55-day) running average filter. As such, only the contributions of the low-frequency ∇T are included in the calculation.
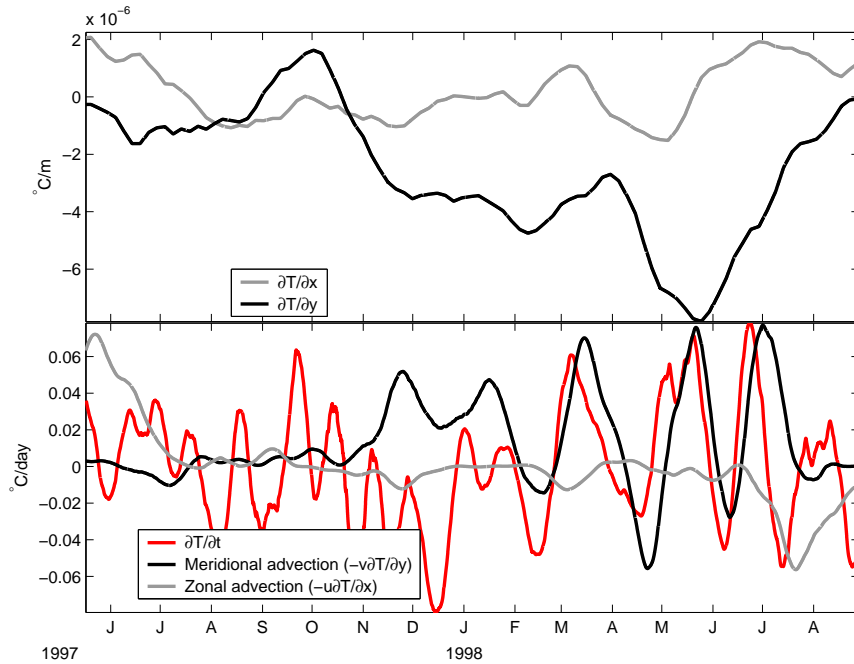
Figure 4-8: Upper panel: Zonal and meridional components of the surface temperature gradient at 10°N, 125°W (grey and black lines, respectively). Lower panel: The estimated contribution of zonal advection (grey line) and meridional advection (black line) to the local rate of change of surface temperature (red line). In the lower panel, all quantities were smoothed by two successive applications of an 11-day moving-average filter.

The zonal temperature gradient was considerably weaker than the meridional temperature gradient (Figure 4-8a). The meridional temperature gradient reached -0.86 °C/° latitude during May 1998 in the final stage of the 1997-98 El Niño event, whereas the magnitude of the zonal temperature gradient never exceeded 0.25 °C/° longitude during the mooring deployment. During May-November 1997, SST gradients were relatively small, the mixed layer was relatively shallow, and the presence of the ITCZ at the site contributed to variability in the surface meteorology, so that SST was more heavily influenced by entrainment and variability in the surface heat fluxes than by horizontal advection during this time period. Zonal advection was relatively unimportant except during the periods of strong zonal flow during June/July 1997 and July 1998 (Figure 4-8b). In contrast, meridional advection by the intraseasonal velocity signal exerted considerable influence on mixed layer temperature during February to June 1998. As noted earlier, the zonal and meridional currents were typically of comparable strength, but the meridional advection term exerted a sustained influence on SST because it was acting more nearly along the mean temperature gradient (Figure 4-8b). Thus, the intraseasonal signal in meridional velocity played an important role

70

in setting the sea surface temperature during most of the first half of 1998.

4.4 Intraseasonal variability near 10°N in the eastern tropical Pacific

The presence of coherent SST and velocity signals at the mooring site indicated that information about the spatial characteristics of the intraseasonal signal might come from satellite measurements of SST. Longitude-time plots of SST and SST filtered to pass 50- to 100-day period, 2-15° wavelength variability along 10.25°N from the WOCE AVHRR SST data set reveal the presence of westward-propagating signals with phase speeds of 8-18 cm/s (Figure 4-9). The intraseasonal signal is evident at the mooring site (125°W) and over a broad range of longitude. The signal phase propagates westward, and the wavelength at the mooring site appears to decrease through time from about 15° longitude during the early part of the mooring record to about 5° by the spring of 1998. By inspection, the westward phase speed at the mooring site during March and April 1998 is estimated to be about 10 cm/s.

The broad spatial and temporal coverage of the TOPEX/Poseidon satellite allows examination of the spatial and temporal structure of the fluctuations in SSH associated with the intraseasonal fluctuations in currents, dynamic height, and SST. The previous work of Perigaud (1990) and Giese et al. (1994) found that intraseasonal SSH signals near 10°N propagate westward. A longitude-time diagram of zonal slope of SSH anomaly also clearly shows westward-propagating variability with intraseasonal periods and wavelengths of roughly 5-15° (Figure 4-10). To the extent that the intraseasonal SSH anomaly signals are resolved in the altimetry data, the zonal slope of SSH anomaly is expected to be proportional to the intraseasonal meridional velocity signal. By inspection, the phase speed of the signal ranges over roughly 8-18 cm/s and the maximum zonal gradients of SSH tend to occur in in the eastern Pacific during the boreal spring. Note that the intraseasonal signal observed at the mooring (and in satellite SST) during the spring of 1998 is not clearly reflected in Figure 4-10, probably because the short wavelength of the signal (about 5° of longitude) is not well resolved in the 1° gridded TOPEX/Poseidon data used for the plot.

An estimate of the distribution of intraseasonal power in time and space is desirable because it can give insight into the generation location of the variability and the zonal
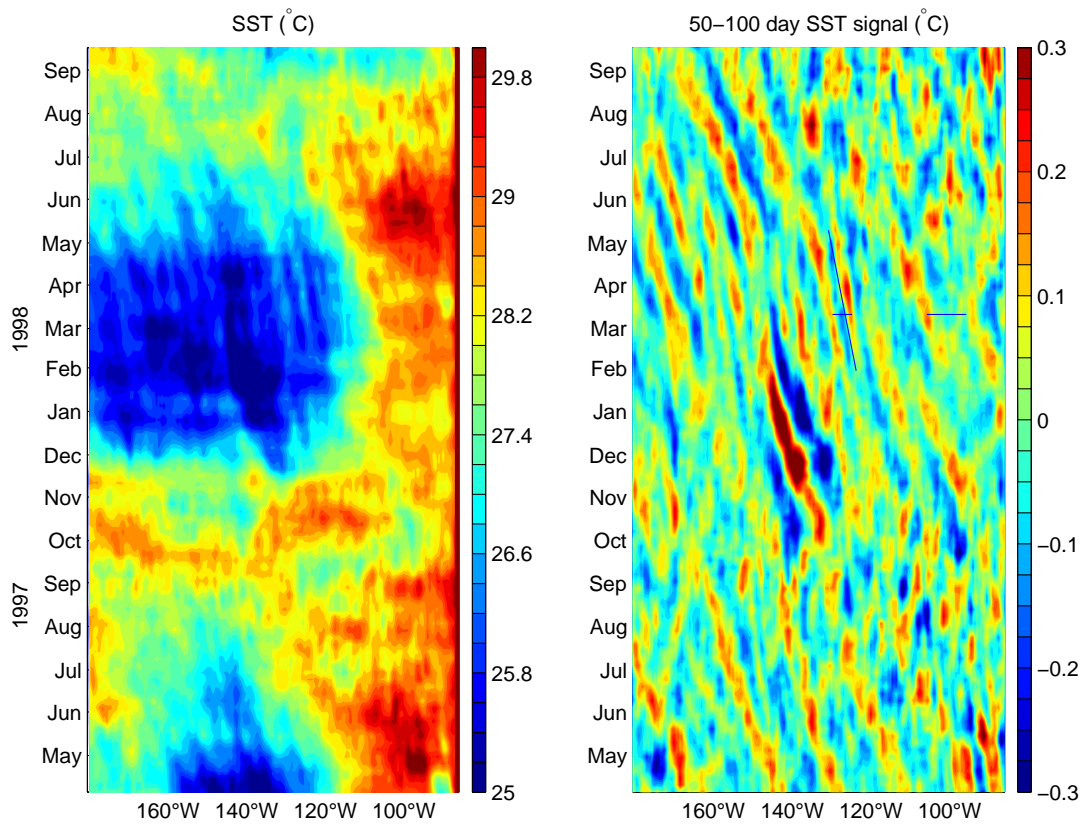
Figure 4-9: Left panel: AVHRR SST along 10.25°N. Right panel: 50- to 100-day SST signal along 9.75°N. In the right panel, a 15° longitude zonal running average was removed to filter SST fluctuations of larger zonal scales. The mooring was located at 125°W. For reference, zonal scales of 5° and 10° longitude are marked in March 1998. The solid diagonal line indicates a westward speed of 10 cm/s.
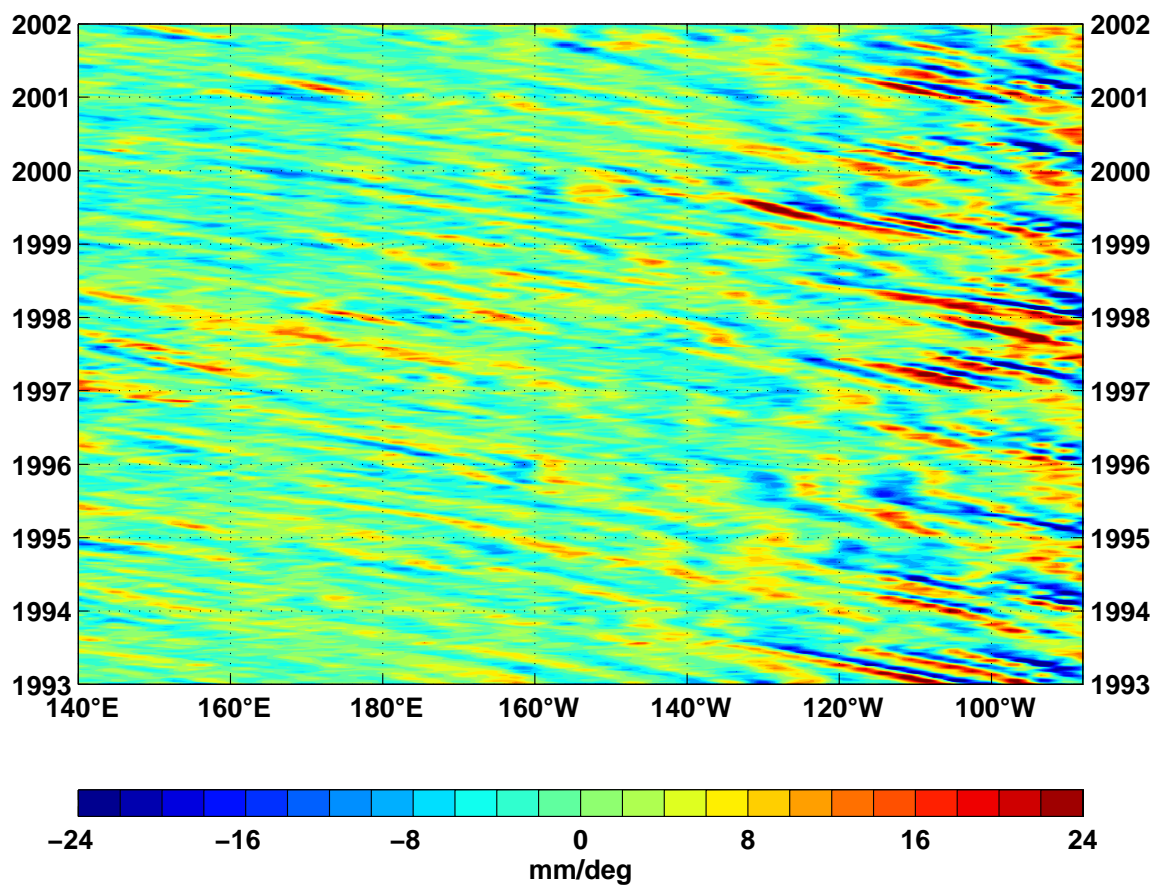
Figure 4-10: Zonal slope of SSH anomaly along 10.5°N. No filter was applied.

direction and speed of energy propagation. One way of producing such an estimate is to compute the wavelet frequency spectrum for SSH at each point in longitude to yield an estimate of intraseasonal SSH power through time and longitude. We computed the wavelet power spectrum of SSH for each location along 10.25°N and extracted time series of power in the 50- to 100-day band. Then, we averaged the 50- to 100-day power estimates over pairs of adjacent longitude points (0.5° apart) to improve the stability of the estimate and took the square root to obtain a time series of 50- to 100-day amplitude for each point (Figure 4-11). As expected from prior work and the observations discussed here, the amplitude is largest east of 120°W and is annually modulated. The westward group speed of first baroclinic mode, long Rossby waves at this latitude in the eastern Pacific is about 20 cm/s, taking the value of the deformation radius to be the zonal mean of the values reported by Chelton et al. (1998) for 88-115°W. This speed, indicated in Figure 4-11, can be thought of as a realistic upper bound on the westward group velocity of baroclinic motions in the region. Although faster westward group speeds are theoretically possible, they require unrealistically large westward current speeds. Most of the localized amplitude peaks in the region appear to travel westward at speeds less than the long Rossby wave group speed (e.g. the peak originating near 105°W at the beginning of 1994), consistent with westward energy propagation. During most years, multiple amplitude peaks appear nearly simultaneously across a fairly broad range of longitude (up to 20°). The increase of energy over such a broad range of longitude is too rapid to be attributable to baroclinic wave propagation from the east. A possible exception is 1998, when an amplitude peak can be seen to travel westward from near the eastern boundary to about 125°W; this different behavior may be related to the transition of the tropical Pacific to a La Niña state after the strong El Niño of 1997-98.

To clarify the temporal variability in the region, the estimates of the wavelet power spectrum of SSH anomaly at each longitude along 10.25°N were averaged into three bins of about 15° longitude within the eastern tropical Pacific. The RMS amplitude of 50- to 100-day variability along 10.25°N was computed by taking the square root of the mean SSH 50- to 100-day power at each longitude (Figure 4-12d). The peak RMS amplitude occurred in the middle bin (100-115°W) and there was a slightly lower peak amplitude in the easternmost bin (88-100°W). In the westernmost bin (115-130°W) the RMS amplitude was substantially smaller than in the two bins to the east, but was above the background level of the central Pacific. As expected from earlier observations of intraseasonal SSH variability

Amplitude of 50 to 100 day SSH variability, 10.25° N
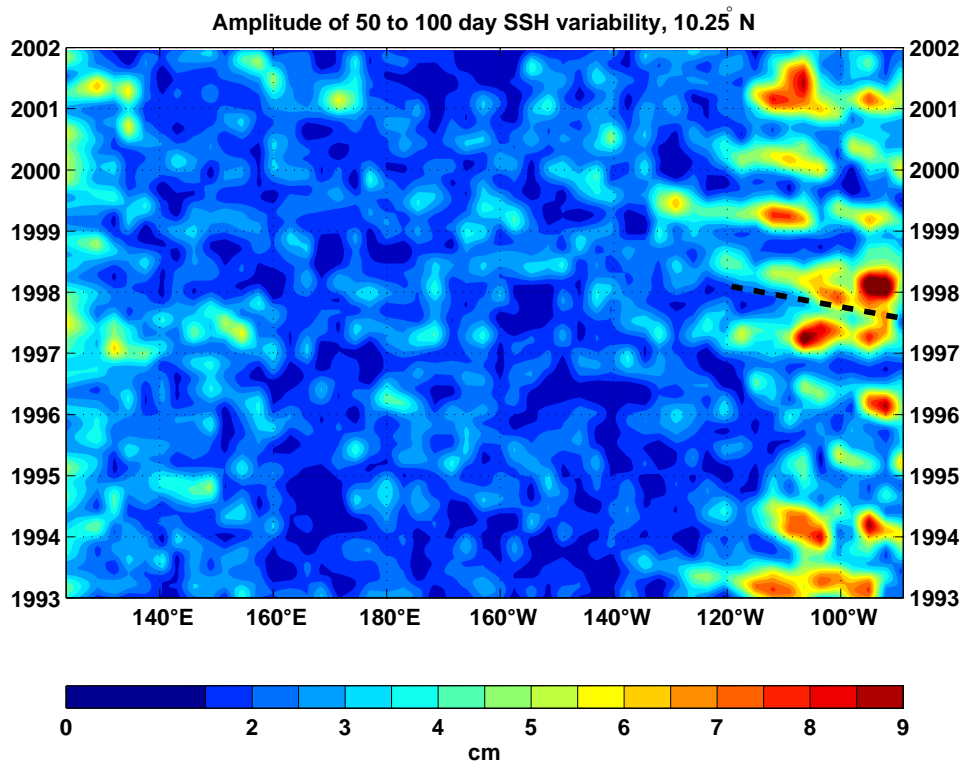
Figure 4-11: Longitude-time plot of amplitude of 50- to 100-day variability along 10.25°N in the tropical Pacific Ocean based on wavelet analysis of TOPEX data from 1993-2001. The time-longitude evolution of amplitude provides an indication of the speed of zonal energy propagation. The thick dashed line indicates a realistic upper bound on the westward group speed for baroclinic Rossby waves in the eastern tropical Pacific (i.e., the long wave speed) During most years, the amplitude increases too rapidly to be attributable to a baroclinic signal that was forced at the eastern boundary. Note that the tropical Pacific was undergoing transition from a strong El Niño to a strong La Niña during early 1998, and it appears that some of the 50- to 100-day amplitude may have propagated well offshore from the eastern boundary during that time period.
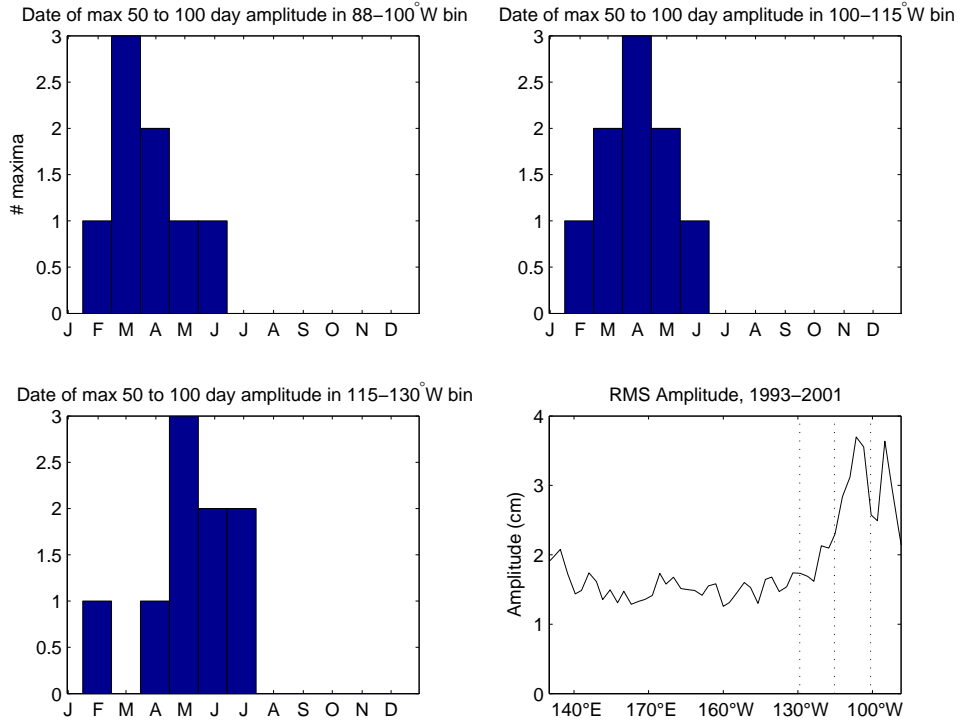
Figure 4-12: Panels (a), (b) and (c): Histograms showing the time of peak amplitude of 50- to 100-day variability during each year at 10.25°N for three sub-regions of the eastern tropical Pacific Ocean based on wavelet analysis of TOPEX data from 1993-2001. Panel (d): RMS amplitude of 50- to 100-day variability as a function of longitude during 1993-2001.

in the region (Miller et al., 1985; Perigaud, 1990; Giese et al., 1994), the amplitude of the 50- to 100-day variability undergoes a substantial annual cycle, with peak amplitudes during roughly the first half of each year. During each of the years 1993-2001, the peak amplitude in each subregion occurs between February and July (Figure 4-12). In the easternmost bin (88-100°W) the peak amplitude occurred most often in March, while in the middle bin (100-115°W) the peak amplitude occurred most often in April, and in the westernmost bin (115-130°W) the amplitude peaked most often in May.

The temporal evolution over 1993 to 2001 of SSH anomaly amplitude in these three longitude bins in the 50- to 100-day period band is shown in Figure 4-13. The amplitude is typically larger in the 100-115°W region than in the 88-100°W or 115-130°W regions; only during 1998 was the amplitude substantially larger in the bin nearest to the eastern boundary. The intraseasonal fluctuations appear to have been less energetic in 1995 and 1996 than in other years. This year-to-year variability may explain the different amplitudes of intraseasonal variability near 10°N in the eastern tropical Pacific reported in prior studies. Miller et al. (1985) reported amplitudes of about 10 dyn cm; Perigaud (1990) reported a

Amplitude of 50 to 100 day band SSH anomaly at 10.25° N
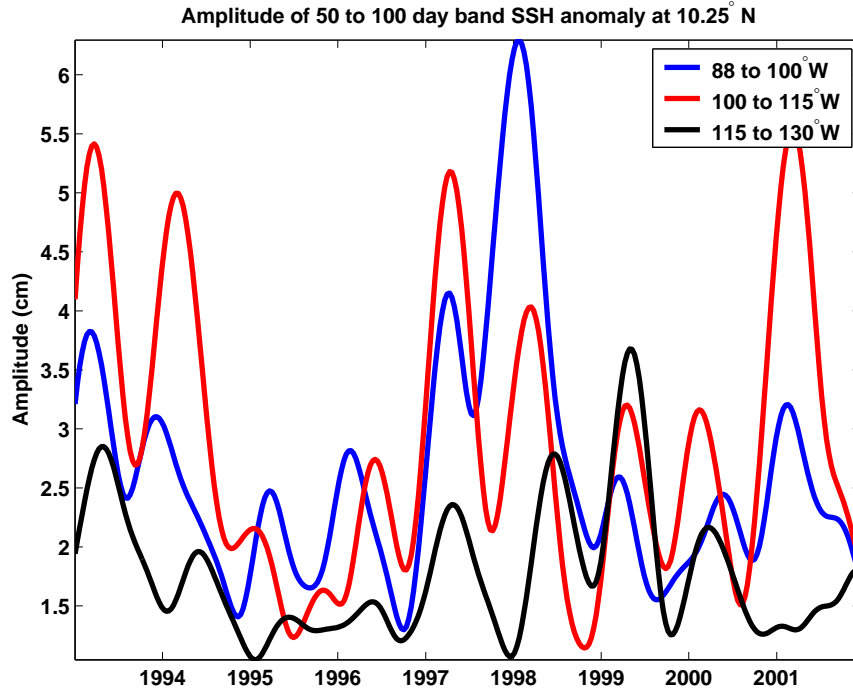
Figure 4-13: Estimated amplitude of 50- to 100-day variability in SSH anomaly at 10.25°N for three sub-regions of the eastern tropical Pacific Ocean. Edge effects potentially contaminate the results during about the first and last 140 days of each time series.

maximum SSH amplitude of 6.9 cm; and Giese et al. (1994) reported amplitudes of 5-13 cm (Giese et al. actually reported 10-25 cm, but we take that to mean peak-to-peak amplitude; see their Figure 3b). While different levels of filtering and signal processing in the various studies can probably account for part of the difference in reported amplitudes, the 9 year time series in Figure 4-13 suggests that much of the difference in observed amplitudes may be due to the intrinsic spatial and interannual variability of the amplitude of the intraseasonal signal.

4.5 Estimation of spatial scales and propagation characteristics

In this section, we present quantitative estimates of the zonal wavelength and phase speed of the intraseasonal signal and investigate characteristic frequencies and wave numbers along 10°N using TOPEX/Poseidon SSH data and the in situ mooring data. The zonal wave number-frequency spectrum was estimated using a two-dimensional Fast Fourier Transform

(2DFFT), by a method similar to that described in Zang et al. (2002), applied to the WOCE Version 3.0 0.5° gridded TOPEX/Poseidon product for the period of 1993-2001. Since the TOPEX/Poseidon satellite generally does not provide data at zonally uniform sampling intervals, the data were first linearly interpolated to the smallest zonal sampling interval. The temporal mean was removed from the sea surface height anomaly before computing the 2DFFT at 9.75, 10.25, and 10.75°N over 140°E-88°W. The points in each periodogram were multiplied by the square of the wave number to obtain periodograms for zonal sea surface slope. The zonal slope of SSH anomaly is taken to be a proxy for upper ocean meridional velocity. The three 2D periodograms, assumed to have uncorrelated noise, were averaged to improve the statistical stability of the spectral estimate. Then, non-overlapping averaging was carried out across seven adjacent frequency bands and three wave number bands. This leads to a total of 125 degrees of freedom and a 95% confidence interval (in a chi-square sense) of 0.22 decibels. To allow for the possibility that the three periodograms are heavily dependent, we also computed a more pessimistic 95% confidence interval for 41 degrees of freedom (0.38 decibels). We will report results based on this second confidence interval.

The resulting wave number-frequency spectrum of SSH zonal slope along 10.25°N shows elevated variance in the 50- to 100-day period band (Figure 4-14). In the figure, westward-propagating signals have negative wave numbers. As might be expected, most of the energy in sea surface slope along 10°N is associated with westward-propagating signals. Most of the energy at periods of 40-70 days has zonal wavelengths of 5-9°, while most of the energy at periods of 75-100 days exists at somewhat larger zonal scales of 6-20°. Within the 10 frequency bands in the 42-102 day period band, the maximum spectral power at each frequency lies at wavelengths between 5.8 and 13.2° longitude. Statistically significant power is found with a broad range of phase speeds, but the spectral peaks all occur at phase speeds of 10-20 cm/s. The intraseasonal variability is not significantly stronger than the semiannual variability when the more pessimistic confidence interval is employed. Even so, Perigaud (1990) showed that the intraseasonal power in SSH anomaly on 10-14°N in the eastern Pacific is substantially higher than in the western Pacific or in the eastern tropical South Pacific. The wave number-frequency spectrum is a measure of the average power over the spatial and temporal domain indicating that, on average during 1993-2001, the most energetic variability in (resolved) sea surface slope in the 40-100 day period band propagates westward with a wavelength of 5-15°. Note that the enhanced power levels at ±4° wavelengths are an artifact

of linear interpolation of the non-uniformly spaced zonal sections to a uniform grid.

We can take advantage of the dynamics that govern variability at frequencies much less than the local inertial frequency to further refine an estimate of the wave number and phase speed of the intraseasonal signal observed at the mooring site. For low frequency motions (frequencies much less than inertial) that are not directly wind driven, the meridional velocity is very nearly geostrophic (e.g. Gill, 1982). That is,

$$v = \frac{g\eta_x}{f}, \tag{4.2}$$

where η is the dynamic height, v is the meridional velocity (relative to the velocity at the reference level for the dynamic height), and the subscript denotes partial differentiation. Supposing that variability at each frequency is associated with only one zonal wave number, the zonal phase speed is given by

$$c_p(\omega) = \frac{\omega}{k} = \frac{\hat{\eta}_t}{\hat{\eta}_x}, \tag{4.3}$$

where $\hat{\eta}_t$ and $\hat{\eta}_x$ are the complex Fourier amplitudes of η_t and η_x, ω is the frequency, and k is the zonal wave number. The phase speed, $c_p(\omega)$, can be thought of as the transfer function (or frequency response function) between dynamic height tendency and dynamic height zonal slope (c.f. Bendat and Piersol, 1986). Using Equation 4.2, we can rewrite Equation 4.3 as

$$\hat{\eta}_t = H(\omega)\hat{v}, \tag{4.4}$$

where $H(\omega) = \frac{c_p f}{g}$ is the transfer function between dynamic height tendency and meridional velocity. This term can be estimated empirically from the mooring data to determine the value of $c_p(\omega)$. This approach was employed by McPhaden (1996) to estimate the phase speed and wave number of monthly period variability observed at a mooring in the tropical Pacific.

Following McPhaden (1996), we calculated the dynamic height relative to 110 m, the deepest current meter depth (Section 4.3). Then, the meridional velocity was referenced to that at 110 m depth to obtain the time series v, and the dynamic height tendency, η_t, was calculated by a 4th-order-accurate centered difference scheme. The empirical transfer function, H, was then computed as described in Bendat and Piersol (1986). Specifically,
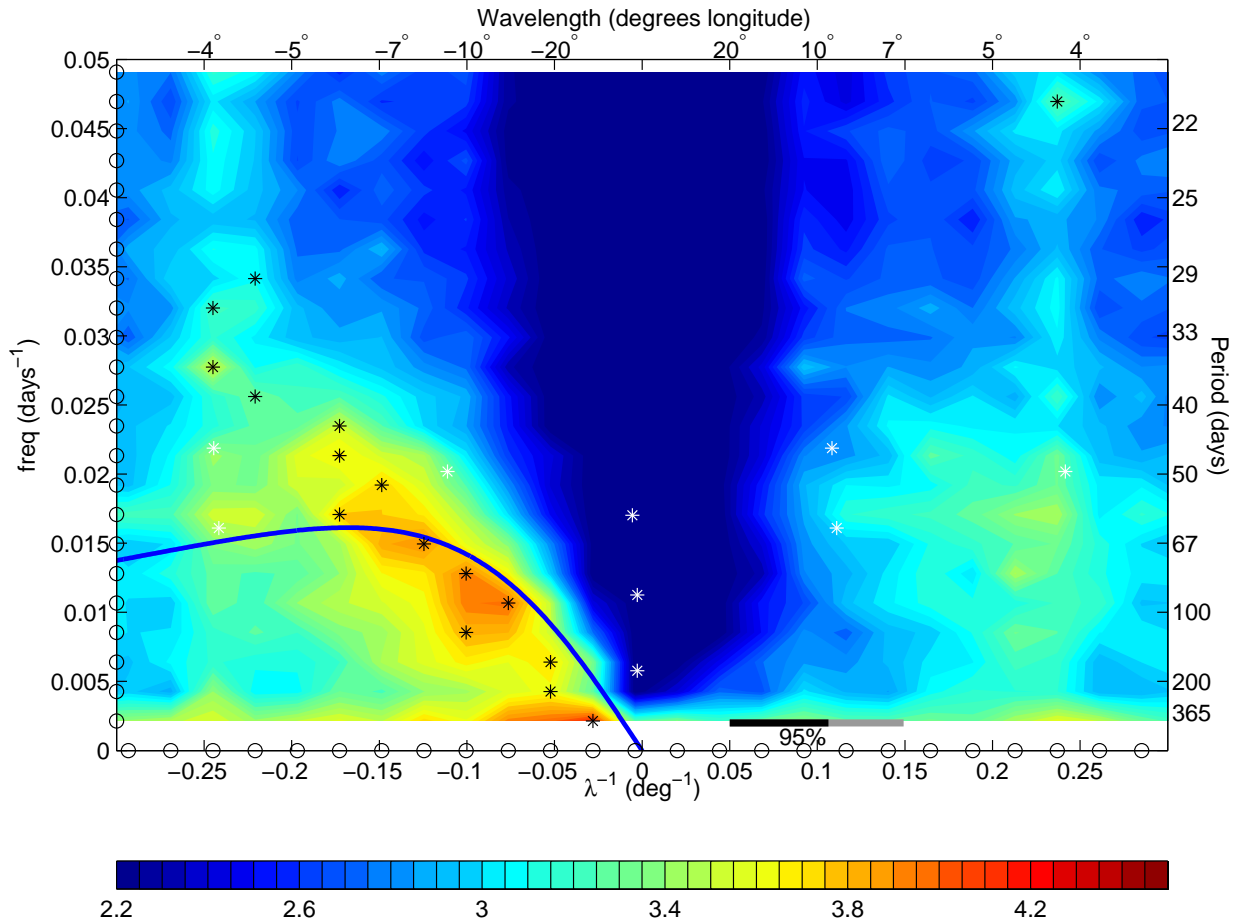
Figure 4-14: Wave number-frequency spectrum of SSH zonal slope along 10.25°N from 1993-2001. For reference, the Rossby wave dispersion relation is shown for free, 1st baroclinic mode Rossby waves computed with the zonal mean value of the deformation radius given by Chelton et al. (1998) and a meridional wave number of zero (blue line). The color-bar has a $\log_{10}$ scale with units of $\mathrm{mm}^2/\mathrm{deg}^2/\mathrm{cpd}/\mathrm{deg}^{-1}$, and the width of the 95% confidence interval (with respect to the color scale) is indicated by a black line for an optimistic estimate of the degrees of freedom. For the more conservative estimate of degrees of freedom described in the text, the additional uncertainty is indicated by the grey line. The black circles indicate the discrete values of frequency and wave number for the estimate. The black asterisks mark the peak power in each frequency band, and the white asterisks mark tidal alias wave numbers and frequencies from Schlax and Chelton (1994).

$H(\omega) = \gamma_{(\eta_t, v)} \sqrt{R} e^{-i\phi}$, where $\gamma_{(\eta_t, v)}$ and ϕ are the coherence amplitude and phase of η_t and v, and R is the ratio of the power spectral densities of η_t and v. Then, the phase speed is given by $c_p = \text{Real}(\frac{gH}{f})$. Note that the transfer function is defined in terms of the coherent variability in v and η_t, so that uncorrelated noise in the measurements of v and η_t does not contribute to H. Furthermore, if another forcing term contributes to variability in v in Equation 4.2 (e.g. local wind forcing), the presence of this forcing does not corrupt the estimate of H, so long as the additional forcing is uncorrelated with the local dynamic height fluctuations (as is likely to be the case for wind forcing).

Using the measured v from the current meters at 50 and 110 m depths and the dynamic height at 50 m relative to 110 m from the period Sept. 2, 1997 to Sept. 14, 1998, we computed the coherence amplitude and phase using a discrete Fourier transform method. After averaging the spectral estimates across three adjacent (non-overlapping) frequency bands, the most energetic low-frequency band for both v and η_t was centered on 0.0186 cpd ($1/54 \ d^{-1}$), representing the variability in the 44-69 day period band. Within this frequency band, the coherence amplitude of 0.95 exceeded the level of no significance at 95% confidence (which is about 0.90), and the phase angle was -11.3° (i.e., η_t leading v). The estimated phase speed is westward at 11.3 ± 5.5 cm/s, where the error bars express 90% confidence limits for the estimates as given in Bendat and Piersol (1971). (The 95% confidence intervals for phase speed are ± 7.0 cm/s.) This calculation confirms the notion that the intraseasonal fluctuations in temperature and dynamic height observed at the mooring are associated with westward-propagating motions, and the estimated phase speed is consistent with the phase speed estimate made by inspection of Figure 4-9. The estimate is comparable to the phase speed estimates near 10°N made by Perigaud (14 cm/s; 1990) and Ballestero and Coen (12.6 cm/s; 2004), but it is somewhat less than the phase speed estimates reported by Giese et al. (17 cm/s; 1994).

The zonal wavelength of the intraseasonal variability observed at the mooring site can be estimated using the phase speed estimate by noting that $c_p = \lambda\sigma$, where λ is the zonal wavelength and σ is the frequency. Thus, the estimated zonal wavelength for the 44-69 day variability at the mooring site is 526 ± 252 km (4.8 ± 2.3° longitude), where the error bars again express 90% confidence limits (95% confidence intervals are ± 3.0°). Again, this estimate is consistent with the wavelength estimated by inspection of Figure 4-9. The estimate also overlaps with the zonal wavelength for energetic intraseasonal variability of
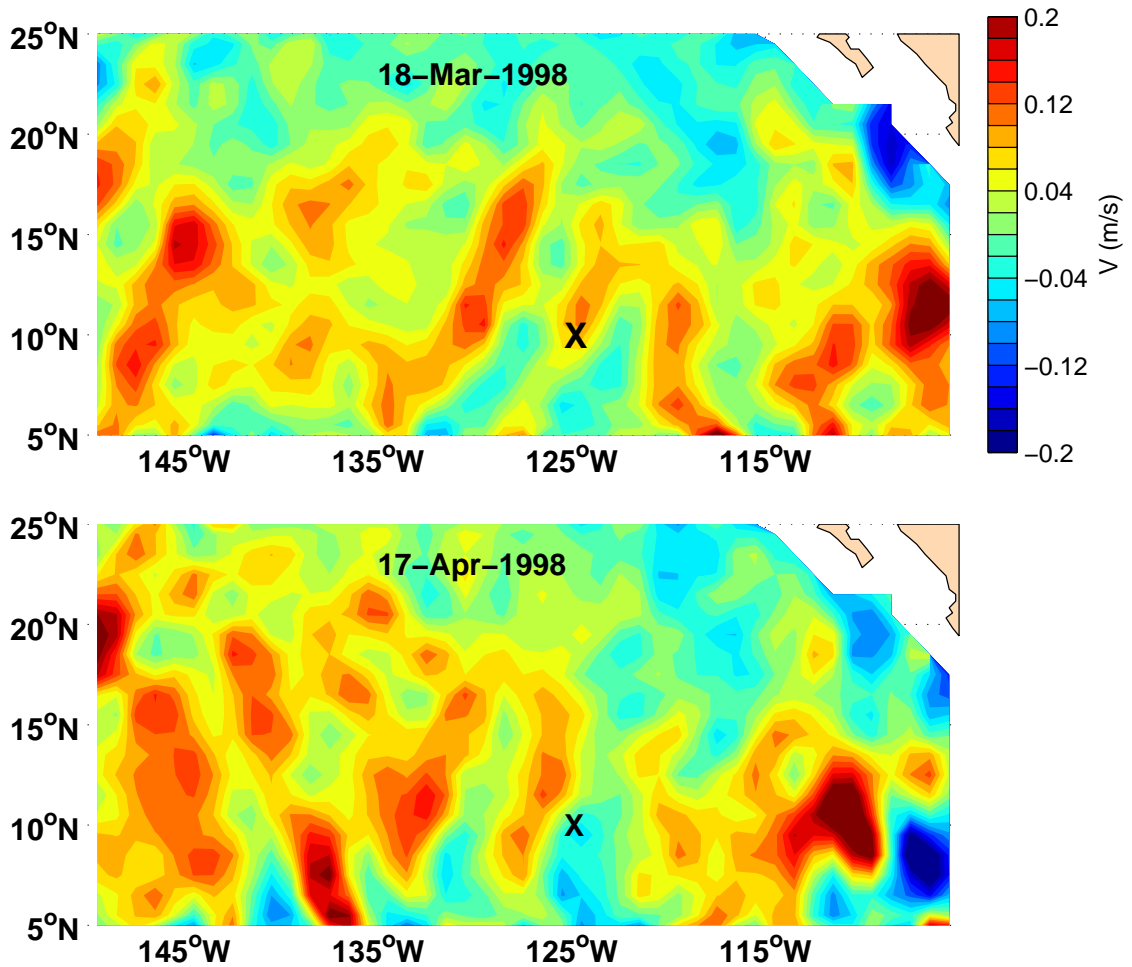
Figure 4-15: Surface meridional velocity in the Bonjean and Lagerloef (2002) surface current analysis during March (upper panel) and April (lower panel) of 1998. The mooring location is marked by an 'X' at 10°N, 125°W. The wave observed by moored instrumentation in the spring of 1998 is visible at the mooring, and it propagates about half a cycle in the 30 days between the two images.

630-950 km identified by Perigaud (1990), though the period band considered here (44-69 days) represents only a subset of the period band of 50-90 days considered by Perigaud. While the study of intraseasonal variability by Giese et al. (1994) did not offer a quantitative estimate of zonal scale, inspection of their Figure 6 suggests a zonal scale of 1100-1600 km (i.e. 10-15°). Note that Giese et al. (1994) examined TOPEX data that were averaged into 3° longitude bins, so that we should expect variability at scales less than about 12° to be poorly represented in their analysis.

We attempted to estimate the meridional wavelength of the 1998 intraseasonal variability at the mooring site by the same method. However, we could not obtain statistically significant intraseasonal coherence between zonal velocity and the dynamic height or its time

derivative. Given the zonal wave number, another way of estimating the meridional wave number is to compute the transfer function between zonal and meridional velocity, which yields an estimate of the ratio of meridional to zonal wave numbers. However, zonal and meridional velocities were also incoherent at intraseasonal frequencies. There are a number of reasons why zonal velocity might be incoherent with dynamic height and meridional velocity, but the most plausible reasons are that either: (1) the meridional wave number varies significantly through time while the zonal wave number does not, or (2) the meridional wave number is much smaller than the zonal wave number, yielding a wave-induced zonal velocity signal that is small. The second possibility is more likely given the lack of a clear zonal velocity signal corresponding to the 2-month signal in meridional velocity (e.g. Figure 4-5). Although the signal is not well resolved in the gridded TOPEX/Poseidon data, a signal matching the zonal wavelength estimated at the mooring and seen in the SST data is intermittently visible in the SSH data and in the Bonjean and Lagerloef (2002) surface current analysis, derived largely from gridded TOPEX/Poseidon data. The phase of this meridional velocity signal (Figure 4-15) matches that observed at the mooring site, but it is noisier and weaker than the observed velocity signal (compare to Figure 4-4). Both of these shortcomings probably result from poor resolution of the approximately 5° wavelength signal in the 1° gridded data used by Bonjean and Lagerloef (2002) and from poor resolution of the signal by the TOPEX/Poseidon flight track itself. Despite these shortcomings, the surface current analysis suggests that the meridional wavelength of the signal observed at the mooring site is perhaps 2-3 times as large as the zonal wavelength, and this helps to explain the incoherency of zonal velocity with dynamic height and meridional velocity at intraseasonal periods.

4.6   Discussion

We have worked to develop a more complete characterization of the intraseasonal variability in dynamic height and currents near 10°N in the eastern tropical Pacific Ocean. For this characterization, we have drawn on in situ observations, satellite altimetry, and satellite SST. The 17-month time series of in situ current and dynamic height observations at 10°N, 125°W reveal the presence of energetic intraseasonal variability. Longitude-time diagrams of SST and zonal slope of SSH anomaly and the wavenumber-frequency spectrum of sea

surface zonal slope indicate that most of the variance in the intraseasonal band is associated with westward-propagating motions having a zonal wavelength of 5-15° of longitude. The zonal scales of these motions ($\lambda/2\pi$) are comparable to the first baroclinic deformation radius ($L_D \approx 1°$; Chelton et al., 1998). Analysis of the in situ current and dynamic height data suggests that the signal observed at the mooring during the spring of 1998 was due to a westward propagating signal with a phase speed of about 11 cm/s and a zonal wavelength of about 5° longitude. The amplitude of this intraseasonal variability has a strong annual cycle and tends to be largest in April.

In this section we first discuss the interpretation of the intraseasonal variability near 10°N as westward-propagating Rossby waves and then discuss the mechanisms that may generate the intraseasonal signal.

4.6.1 Observed intraseasonal variability and the Rossby wave dispersion relation

The wavenumber-frequency spectrum of observed sea surface zonal slope (Figure 4-14) shows energy at 40-60 day periods propagating westward at 8-15 cm/s. Overlaid on the spectrum is the dispersion curve for a free, first-mode baroclinic Rossby wave with a meridional wavenumber of zero, where mean flow effects are ignored. The peak of this curve, which occurs at a wavelength of $2\pi L_D \approx 6°$ and a frequency of $\sigma_{max} = \frac{\beta L_D}{4\pi}$, represents the maximum theoretical frequency at which non-equatorially trapped baroclinic quasi-geostrophic signals can exist in the absence of Doppler shifting by the mean flow (c.f. Gill, 1982). Here, L_D is the Rossby deformation radius, which is taken to be the zonal mean of the values given by Chelton et al. (1998). There are a few reasonable explanations that can account for the presence of significant energy in sea surface zonal slope at frequencies higher than this curve. Perhaps the most likely explanation is that, at this latitude of mean westward flow, first baroclinic mode signals are Doppler shifted by the NEC. Another possible explanation is that the energy at these frequencies and wavenumbers is due to equatorial Rossby waves that are weakly trapped (i.e., meridional mode numbers greater than 2). Perigaud (1990) showed that the intraseasonal variability seen near 10°N is neither symmetric nor antisymmetric about the equator, so this possibility is not likely. Barotropic motions can exist at much higher frequencies because the barotropic deformation radius is much larger. It is con-

ceivable that barotropic motions contribute to the variance observed at these wavenumbers and frequencies. However, given that the energy in SSH anomaly is largely associated with the first baroclinic mode (Wunsch, 1997) and that the intraseasonal variability is associated with baroclinic disturbances (e.g., Figure 4-4), it seems unlikely that barotropic motions are responsible.

We now explore the possibility that the observed dispersion characteristics of the intraseasonal variability near 10°N are due to Doppler shifting by the mean zonal flow. In the presence of a spatially uniform steady zonal flow, U, the Rossby wave dispersion relation for a $1\frac{1}{2}$ layer flow is given by (e.g., Pedlosky, 1979, p. 109),

$$\omega = \frac{kU(k^2 + l^2) - \beta k}{k^2 + l^2 + L_D^{-2}} \tag{4.5}$$

where k and l are the zonal and meridional wave numbers.

Equation 4.5 is the primary theoretical basis for the so-called "non-Doppler shift" of long Rossby waves (e.g. Kessler, 1990). Long Rossby waves ($k \approx 0$ and $l \approx 0$) are relatively insensitive to the mean flow because the first term in the numerator goes to zero with k and l more rapidly than the second term; in contrast, short Rossby waves are susceptible to substantial Doppler shifting by the mean flow. The definition of a long wave can be based on the criterion that the wave travels westward though a quiescent background at a speed that is some fraction, say 90%, of the speed of a wave with infinite wavelength. At 10°N in the eastern Pacific, the tilted eastern boundary prohibits waves of infinite meridional scales. Waves here with comparable meridional and zonal scales (and L_D =93 km) would need a zonal wavelength of at least 23° longitude to be considered long and be insensitive to Doppler shifting. If we took $l = 0$ despite the tilted eastern boundary, a wavelength of 16° longitude would be considered long. In the western Pacific, with its lack of strongly tilted boundaries (but larger L_D), a zonal wavelength of 20° longitude would be considered long.

Even these long waves will be Doppler shifted if the zonal flow is strong enough; it is the ratio of $U(k^2 + l^2)$ to β that determines whether the non-Doppler shift principle holds. For example, a wave on 10°N in the eastern Pacific travelling in a 30 cm/s westward current with $l = 0$ and a zonal wavelength of 16° longitude will have a phase speed that is about 17% faster than it would in a quiescent ocean. A more accurate dispersion relation can be formulated by linearizing the governing equations about a meridionally-varying zonal flow (e.g., Chelton et

al., 2003), but because the most energetic intraseasonal signals are confined to a fairly narrow latitude band (10-13°N; Perigaud, 1990; Giese et al., 1994) and the flow is similar over this latitude band, we expect that Equation 4.5 will provide a reasonable approximation to the dispersion curve of the energetic intraseasonal variability in the presence of the westward NEC.

Although the result is qualitatively similar for a broad range of values of U, choosing the value of U is not trivial. There is significant zonal and temporal variation in the NEC and in the energetic intraseasonal variability, and, even without this variability, choice of an appropriate upper layer zonal flow is not necessarily straightforward (e.g., Chelton et al. 2003). One might expect the appropriate value of U to be the mean U over the season and region in which the energetic intraseasonal variability is observed. In order to choose an appropriate value for U, we consulted the Bonjean and Lagerloef (2002) tropical Pacific surface current analysis for 1993-2004, which provides a good representation of the zonal currents observed at the mooring site. We constructed a monthly mean climatological current field from the Bonjean and Lagerloef (2002) currents to consider the seasonal and spatial evolution of the zonal surface currents.

Examination of the spatial structure of the zonal currents suggests that the low frequency zonal currents observed at the mooring site are not representative of the zonal mean currents or of the zonal currents to the east of the mooring site, where the intraseasonal variability in SSH is greatest. For this reason, we chose a value of U based on the Bonjean and Lagerloef (2002) zonal currents, rather than using the zonal currents observed at the mooring. The zonal and temporal mean value of the zonal current along 10.25°N is about -12 cm/s on 88°W-140°E (used for the spectral calculation) and is about -11 cm/s on 88-115°W (the region of strongest variability). To explore the potential role of Doppler shifting by the zonal flow in the observed dispersion curve of the intraseasonal variability, we will use U=-11 cm/s. There is considerable uncertainty in the appropriate choice of a vertical averaging interval for U, and without a much more detailed analysis (e.g., Chelton et al., 2003) the choice of U is somewhat arbitrary. Similar ambiguities are involved in choosing a value of the deformation radius. For consistency with the chosen zonal current, we will take L_D=93 km, the zonal mean over 88-115°W of the climatological first baroclinic deformation radius given by Chelton et al. (1998) at 10.25°N. Due to the myriad uncertainties involved in choosing parameters for the dispersion curves, the resulting curves are mainly useful for qualitative

understanding of the effect of the NEC on the observed dispersion characteristics. The Doppler shifted dispersion curves are not overly sensitive to the value of U. Changing the mean flow by a few cm/s yields dispersion curves that are quite similar, and the curves for values of U ranging from -6 to -20 cm/s share qualitative similarities.

Figure 4-16 shows the variance-preserving wave number-frequency power spectrum of sea surface zonal slope, plotted so that the volume under each peak reflects its contribution to the signal variance. When plotted in this form, it is clear that the variance of sea surface zonal slope at periods less than annual is dominated by 50- to 100-day variability. It is also noteworthy that the M_2 tidal alias with about a 4° westward wavelength and 62 day period (Schlax and Chelton, 1994) contributes appreciably to the variance of the zonal slope, though the alias certainly does not dominate the variance. Four dispersion curves for free, first baroclinic mode Rossby waves, with meridional wave numbers ranging from $l = 0$ to $l = k$ and zonal mean flows ranging from zero to -11 cm/s are shown. Given that most of the power in sea surface zonal slope lies near the Doppler shifted dispersion curves, the most energetic motions in sea surface zonal slope (and by extension, the surface meridional velocity) can be interpreted as first baroclinic mode Rossby waves propagating in the westward-flowing NEC. Notice that the effect of the Doppler shifting is to make the variability nearly nondispersive and reduce the difference between waves of finite and infinite meridional scale. The wave number and frequency estimated for the velocity signal at the mooring is also indicated; this estimate overlaps the range of frequencies and wave numbers that dominate the variance of sea surface zonal slope.

We suggest that the observed dispersion characteristics of the variability on 10°N can be interpreted as being due to linear Rossby waves in a mean westward flow. This may be an oversimplification, not only because the space-time variability of the westward flow and the deformation radius limits the useful application of Equation 4.5, but also because the strong eddies observed in the eastern Pacific warm pool are likely to be nonlinear. Different nonlinear models of these eddies have been discussed by Hansen and Maul (1991) and Yamagata and co-investigators (Matsura and Yamagata, 1982; Yamagata et al., 1990; Umatani and Yamagata, 1991). These models suggest that the eddies should travel slightly faster than the long Rossby wave speed, consistent with other models of nonlinear eddies (e.g., McWilliams and Flierl, 1979). However, the quasi-geostrophic model discussed by McWilliams and Flierl (1979) suggests that the eddy speed is constrained by the linear wave
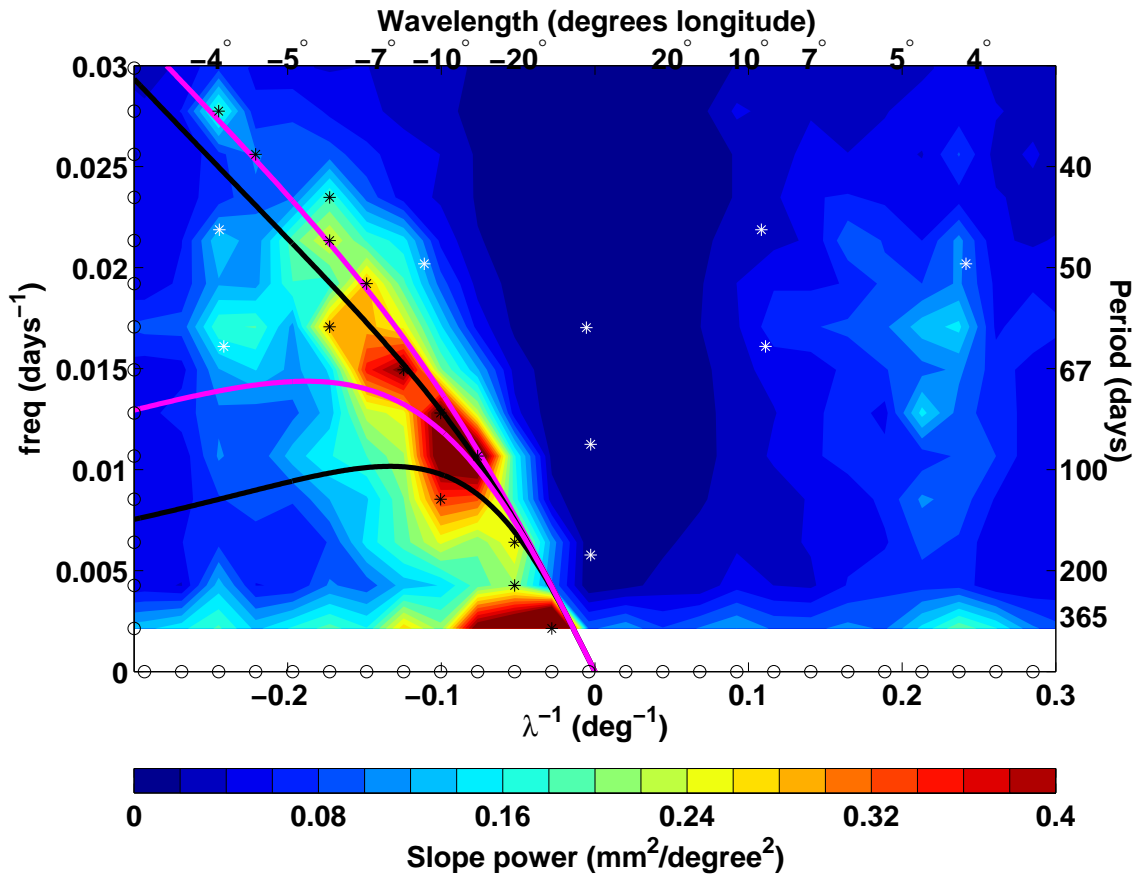
Figure 4-16: Variance-preserving spectrum of TOPEX/Poseidon zonal sea surface slope in units of mm^2/degree^2 at 10.25°N. Dispersion curves are shown for $l = 0$ (pink) and $l = k$ (black) with a mean zonal flow of -11 cm/s (upper curve) and without mean flow (lower curve). Black asterisks mark peaks of spectral density at each frequency, white asterisks mark known TOPEX tidal aliases, and the solid black circle marks the wave number and frequency estimated for the wave observed at the mooring. The dashed line marks the 90% confidence interval and frequency band for the mooring estimate.

field in the surrounding fluid, and perhaps this contributes to the wave-like nature of the observed dispersion characteristics.

4.6.2 Potential generation mechanisms

A variety of generating mechanisms for the intraseasonal variability have been proposed in the literature, but no consensus has been reached. The eastern tropical North Pacific is a region of strong wind forcing, annual variability, zonal currents, and a complex mean circulation. More than one of the proposed mechanisms may be involved in setting the properties of the observed intraseasonal variability. Perigaud (1990) hypothesized that the intraseasonal variability near 10°N is generated by barotropic instability associated with the NEC/NECC shear, in a manner analogous to the generation of tropical instability waves farther south. However, Perigaud noted that the shear strength along 12°N does not coincide well in space and time with the observed wave growth. Philander (1976) suggested that the NEC may be baroclinically unstable; based on a calculation with an idealized two-layer model, he suggested that the resulting waves would have a period of 30 days, a wavelength of 7° longitude, and an *e*-folding time of at least 60 days.

Yamagata et al. (1990) showed that sufficiently strong, steady forcing of potential vorticity can generate a sequence of propagating anticyclonic eddies for parameters appropriate to the strong wind stress curl signal associated with the passage of winds through the Central American mountain gaps of Tehuantepec and Papagayo. Umatani and Yamagata (1991) appealed to this theory to explain sequential eddies emanating from the Gulf of Tehuantepec in a high resolution numerical model forced with monthly mean climatological winds. A variant of this idea was proposed by Giese et al. (1994), who argued, based on the relative timing of 7 wind events and 5 visible eddies over a 17-month period, that fluctuations in the mountain gap winds may force the intraseasonal eddies. McCreary et al. (1989) employed analytical and numerical models to examine eddy generation by the mountain gap winds, and found that a cyclonic and anticyclonic eddy pair develops rapidly in response to the mountain gap winds, but by the time the eddy pair begins to detach from the coast (about 10 days after starting to form) the anticyclonic eddy is much stronger than the cyclonic eddy. Another interesting result of the the McCreary et al. analysis is that the anticyclonic eddies emanating from Tehuantepec weaken and broaden as they move away from the coast,

whereas the ones from Papagayo do not.

Another possible source of intraseasonal variability in the eastern tropical Pacific is the strong intraseasonal coastal sea level variability associated with baroclinic Kelvin waves propagating poleward along the west coast of the Americas (Spillane et al., 1987). This variability is believed to result from equatorial Kelvin waves forced by intraseasonal variability in the large scale zonal winds (Enfield, 1987; Kessler et al. 1995; Zang et al., 2002). The equatorial intraseasonal Kelvin waves have largest amplitude in the boreal fall and winter at 140°W (Kessler et. al, 1995). The amplitude of the coastal sea level and thermocline depth variability is expected to increase as the wave propagates northward from the equator to regions with a smaller deformation radius (Moore and Philander, 1977). The observations of Spillane et al. (1987) show peak intraseasonal RMS sea level amplitudes between about 7°N and the Gulf of California of a few centimeters. This intraseasonal coastal sea level and thermocline depth variability may radiate intraseasonal Rossby waves to the west.

Hansen and Maul (1991) argued that propagating anticyclonic circulations observed with drifters in the region are caused by conservation of potential vorticity as the NECC collides with the eastern boundary (the retroflection hypothesis). In this hypothesis, water that has travelled eastward in the NECC at a latitude between 5-8°N is moved northward along the eastern boundary to about 11°N where the water must take on anticyclonic relative vorticity to conserve potential vorticity. The resulting anticyclonic eddy then propagates westward under the influence of β. At its core, this hypothesis involves only potential vorticity conservation and the notion that the water near 10°N had come from the NECC. This hypothesis is somewhat different from the other three in that it offers only a diagnostic relationship between the eddies and their initial position and potential vorticity, rather than specifying a clear causal chain of events. Put another way, the eddies and the retroflection may be seen as part of a single process, and this process needs explanation; perhaps it would be due to some instability of the NECC or northward advection around the shoreward side of the Costa Rica Dome. It is also unclear to what extent potential vorticity is conserved in the presence of the strong vorticity forcing by the mountain gap winds (Kessler, 2002; Chelton et al., 2004) and the vorticity homogenization that may occur at the eastern boundary. The NECC retroflection hypothesis may very well be correct, but, if it is, further work will be required to explain the process that causes the retroflection and the eddies.

Determination of the generation mechanism(s) for the eastern tropical Pacific 50- to

100-day variability along 10°N is beyond the scope of this paper, but we tested the various hypotheses to the extent allowed by our results. Our analysis suggests that the 50- to 100-day variability near 10°N has the following characteristics: (1) The signal is strongest between 120°W and the eastern boundary, but the largest amplitude does not necessarily occur at the eastern boundary. (2) The signal amplitude is annually modulated, with peak amplitudes occurring around April in the region of strongest variability. (3) The signal is associated with zonal wavelengths of 5-15° and westward phase speeds of 10-17 cm/s. (4) The 50- to 100-day SSH amplitude along 10°N increases rapidly over a broad range of longitudes.

This last point may provide an important clue about the generation mechanism for the intraseasonal variability. The wavenumber-frequency spectrum of sea surface slope suggests that the intraseasonal variability propagates westward in a manner consistent with expectations for first baroclinic mode, free Rossby waves. However, the nearly simultaneous appearance of power on such a broad range of longitudes during the boreal spring would require an unrealistically large westward group speed in order for the energy to have travelled directly westward from the eastern boundary. Moreover, there are no years (with the possible exception of 1998) where the 50- to 100-day amplitude present at, say, 110°W can be observed to have propagated directly westward from the eastern boundary (Figure 4-11). This may indicate that the signal originates or grows in the ocean interior, perhaps as a result of instability of the zonal equatorial currents as hypothesized by Philander (1976; baroclinic instability) or Perigaud (1990; barotropic instability). While this line of reasoning suggests that the signal may originate in the ocean interior, it does not rule out the possibility that the 50- to 100-day power was generated near the eastern boundary at another latitude before propagating southwestward to appear offshore at 10°N. We examine this possibility below.

Some insight into the importance of intraseasonal variations in winds can be gained by examination of the output of realistic numerical models that are forced by monthly mean climatological winds. We examined intraseasonal variability in a high resolution ocean general circulation model (GCM), forced by monthly mean Hellerman and Rosenstein (1983) climatological winds, which shows energetic intraseasonal variability near 10°N with frequencies and zonal scales similar to what is observed. This model simulation was carried out by Jochum and Murtugudde (2004) for examination of tropical instability waves in the Pacific.

The modeled meridional velocity at the mooring location (not shown) is qualitatively similar to the meridional velocity record observed at the mooring (Figure 4-4), in that the

record is dominated by intraseasonal fluctuations that are more energetic above the pycnocline, and the amplitude and seasonal cycle of the intraseasonal current fluctuations are similar to what is observed. In addition, the wave number-frequency spectrum of the modeled meridional velocity is similar to that of the zonal slope of observed SSH, with both spectra showing elevated variance at similar wave numbers in the intraseasonal band. Comparison of longitude-time plots of the model's meridional velocity to the observed zonal slope of SSH reveals some qualitative differences, though. One notable qualitative difference is in the longitude of maximum amplitude; in the observations, the intraseasonal signal in sea surface slope has a maximum near 100-115°W, whereas the signal in the model meridional velocity has a maximum amplitude near 130°W and a weaker local maximum near 100°W. The intraseasonal currents in the model are different each year and the monthly mean climatological winds used to force the model have little energy at intraseasonal frequencies, so it seems unlikely that the intraseasonal variability in the model is due to direct wind forcing at intraseasonal frequencies as hypothesized by Giese et al. (1994) for the observed intraseasonal variability. Umatani and Yamagata (1991) also found strong intraseasonal variability in a high resolution (0.25°) ocean model forced by the same monthly mean winds. They attributed the variability to excitation of successive eddies by the steady supply of potential vorticity at the Gulf of Papgayo via the nonlinear mechanism described by Yamagata et al. (1990). The retroflection hypothesis or instabilities of the zonal equatorial currents might also explain the presence of intraseasonal variability in the models, but direct forcing by intraseasonal wind variations does not seem to be fundamental to the existence of the intraseasonal velocity variability.

Baroclinic instability?

Before relating the results from 10°N to the dynamics of the broader region, we briefly explore the possibility that the variability on 10°N is associated with baroclinic instability of the NEC. Philander (1976) employed the Phillips (1951) model to show that the NEC may be baroclinically unstable. For a two-layer system with a very small Rossby number, a necessary condition for baroclinic instability of a uniform westward zonal current is

$$U_1 - U_2 < \frac{-\beta g' H_1}{f^2},$$

(4.6)

where g' is the reduced gravity, H_1 is the thickness of the upper layer, and U_1 and U_2 are the velocities of the upper and lower layers. The deformation radius of the first baroclinic mode is $L_D = \frac{\sqrt{g'H_1 H_2}}{f\sqrt{H_1 + H_2}}$ where H_2 is the lower layer thickness. For $H_1/H_2 \to 0$ (a reasonable approximation for the eastern tropical Pacific), the necessary condition for baroclinic instability is given approximately by an upper-layer flow satisfying

$$U < -\beta L_D^2. \tag{4.7}$$

(In this limit of an infinitely thick lower layer, $U_2 \to 0$.) Note that $-\beta L_D^2$ is the speed of phase and energy propagation for long Rossby waves. Using Equation 4.7 and the zonal mean value of the deformation radius given by Chelton et al. (1998) for 88-115°W on 10.25°N in the Pacific, we find that this approximate necessary condition for baroclinic instability is met when $U_{crit} \approx -20$ cm/s. In theory, an eastward zonal current can also be baroclinically unstable, but because the upper layer of the tropical Pacific is much thinner than the lower layer, eastward currents require a much larger flow speed for instability. Pedlosky and Thomson (2003) have recently shown that time dependent zonal flows can become baroclinically unstable at even lower speeds than implied by the steady model.

Clearly, the two-layer model is a highly idealized approximation to the real ocean and the zonal flow in the region has considerable spatial and temporal variability, so the value of U_{crit} given here is not likely to be quantitatively accurate. Gill et al. (1974) compared baroclinic instability in the two-layer model to that in a continuously stratified fluid and discussed strengths and shortcomings of the two-layer model. Serious shortcomings of the two-layer model are its neglect of near surface horizontal density gradients, which can dramatically affect stability properties, and the poorly constrained choice of appropriate values of g', H_1, and H_2. When $H_1/H_2 \to 0$, the latter difficulty is somewhat alleviated because we only need to specify the first baroclinic deformation radius, which is well constrained by available data. Neglect of horizontal density variations is certainly an issue, but we can at least note that a negative meridional temperature gradient (i.e. warmer water to the south) tends to stabilize a westward current, whereas a positive temperature gradient tends to destabilize the current. During the season of active intraseasonal variability (as well as in the long term mean, e.g., Figure 4-1), the meridional surface temperature gradient is positive on 10°N in the eastern Pacific because the peak SSTs of the eastern Pacific warm pool are to the north.
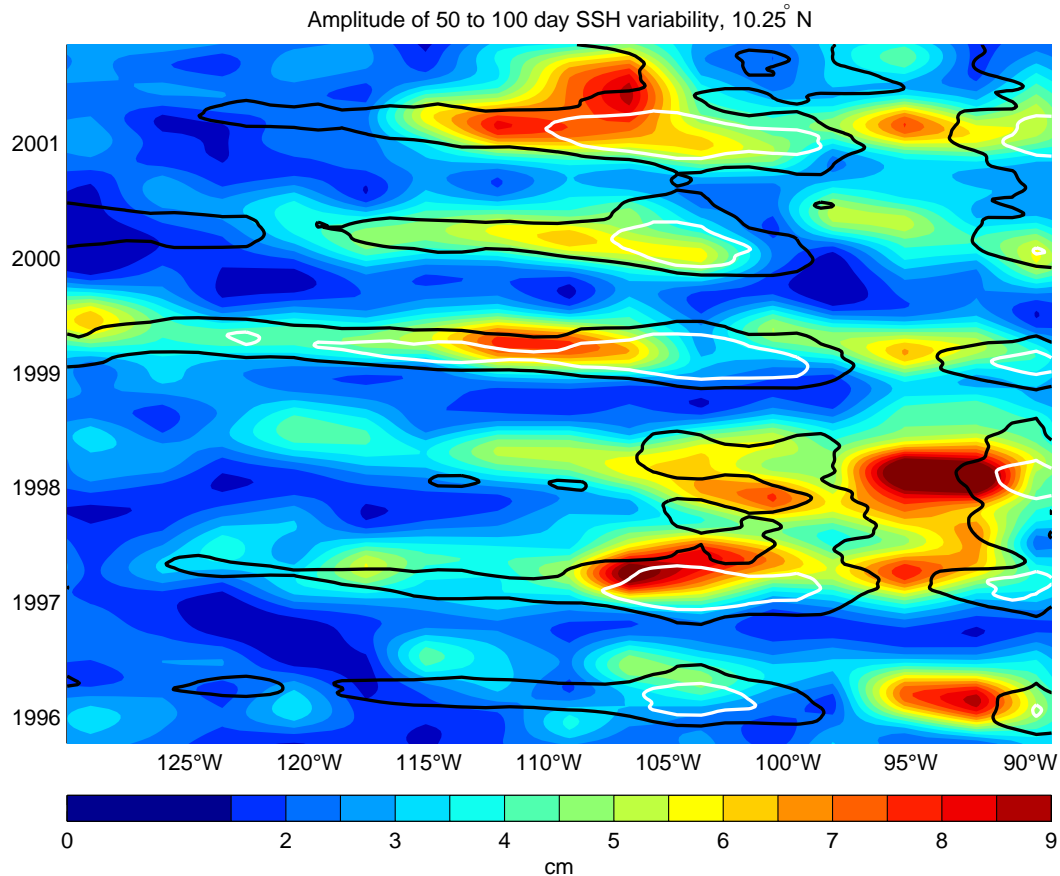
Figure 4-17: Amplitude of 50- to 100-day SSH signal along 10°N (color contours). Contours of low-frequency (125-day running-mean) zonal velocity are shown at -15 cm/s (black contours) and -25 cm/s (white contours).

In the central and western Pacific, the surface temperature gradient is generally negative, so we expect this region to be more stable than the two-layer model would suggest.

We have attempted to determine whether there is a link between the westward zonal current and the growth of 50- to 100-day oscillations near 10°N in the eastern tropical Pacific by re-examining the amplitude of 50- to 100-day SSH variability in the eastern tropical Pacific during 1996-2001 in the context provided by the Bonjean and Lagerloef (2002) surface current estimates. Figure 4-17 shows the amplitude of 50- to 100-day SSH variability in the eastern tropical Pacific during 1996-2001. The 125-day running-mean westward zonal current from the Bonjean and Lagerloef (2002) surface current analysis is also indicated. As is often noted (e.g., Pedlosky, 1979, p. 491), the observed zonal flow is not necessarily a good measure of the background zonal flow that would exist in the absence of instabilities because the observed flow is altered by the presence of instabilities. Nevertheless, the space-time correspondence of

strength of the westward flow with the amplitude of 50- to 100-day variability is remarkable. Episodes of intense 50- to 100-day SSH variability are typically preceded by an increase of westward flow speeds associated with the normal seasonal cycle of the NEC. In addition, the westward flow often decreases as the 50- to 100-day oscillations grow, suggesting that the 50- to 100-day oscillations may be drawing energy from the large scale zonal current. The GCM output discussed earlier exhibits a similar relationship of westward flow speed and 50- to 100-day variability. These facts suggest that the intraseasonal variability and its annual cycle are influenced by baroclinic instability of the NEC in the eastern part of the basin.

While baroclinic instability does seem to be a plausible explanation of some the observed properties of the intraseasonal variability, some of the other hypotheses may be equally plausible. It is not obvious that the baroclinic instability hypothesis can explain the often-noted tendency for anticyclonic eddies in the region (e.g., Hansen and Maul, 1991; Giese et al., 1994), and the space-time correlation of 50- to 100-day amplitude with zonal flow speeds meeting the two-layer model instability condition may be a mere coincidence. Most properties of the eastern tropical Pacific in the region have a strong annual signal, so correlation of two quantities in the region at annual periods is not especially strong evidence of a direct causal relation. Anticyclonic eddies have been observed to propagate southwest from the Gulf of Tehuantepec at about 13°N and either cross or travel along 10°N on 100-115°W (e.g., Giese et al. 1994). This could explain the enhanced intraseasonal variability in the region, and the coherence with the zonal flow might be explained as a rectification of the velocity of the eddies (though, if this were the case, we would expect peak eddy activity to occur at the same time as peak low-frequency zonal flow). Both the coastal wind forcing and retroflection hypotheses can readily explain the tendency for anticyclonic eddies. Without the full context in latitude, longitude, and time, the results from 10°N are difficult to interpret, so we now briefly consider the evolution of the variability in latitude and longitude.

Examination of the variability in its dynamical context

We examined sequential images of 50- to 100-day band-passed SSH (from the 1° gridded WOCE TOPEX/Poseidon product) from the 1994-2002 seasons and present sequential images for the 1997 and 1999 seasons here (Figures 4-18-4-19). We take a "season" to encompass the periods before, during, and after peak 50- to 100-day variability (i.e., roughly October-

June). The choice of years was motivated by the following factors. With the exception of the 1998 season, which involved a rapid transition from a strong El Niño to a strong La Niña, the different seasons were qualitatively similar. We chose the 1997 season because it includes some eddies that passed the mooring site during the early part of the mooring deployment (May-August 1997), and we excluded the 1998 season because the adjustment from El Niño to La Niña makes the imagery difficult to interpret (e.g., Figure 4-17). In addition, the waves observed at the mooring site during the spring of 1998 are not well-resolved in the 1° gridded SSH data, so little insight into these waves is gained through inspection of sequential images. We chose the 1999 season because Figure 4-17 indicates that there was a broad region of the NEC along 10°N that was potentially baroclinically unstable during this time.

We also estimated the surface geostrophic flow using the 1° gridded WOCE TOPEX/Poseidon product and the mean dynamic height relative to 1000 m from Levitus et al. (1997) following Bonjean and Lagerloef (2002). We chose to compute the geostrophic flow in this way because the Bonjean and Lagerloef (2002) currents include an Ekman flow with a westward component near 10°N due to the northeasterly trade winds. Excluding the Ekman flow, which does not contribute directly to instability, allows a more rigorous test of the baroclinic instability hypothesis. The currents used here are qualitatively similar to the Bonjean and Lagerloef (2002) currents, but tend to be weaker. To allow examination of the possibility that baroclinic instability influences the evolution of 50- to 100-day SSH amplitude, contours of $U/\beta L_D^2$ are indicated for westward currents. We also overlaid contours of the NECC zonal current speed in Figures 4-18-4-19 to facilitate evaluation of the retroflection hypothesis. All zonal currents were low-pass filtered with a 100 day cut-off. To strike a balance between covering a broad time period and displaying a manageable number of images, we chose to show images at 30-day intervals. In most cases, this still allows eddies and other 50- to 100-day SSH anomalies to be tracked through sequential images.

Each year, both positive and negative 50- to 100-day SSH anomalies emanate from near the Gulfs of Tehuantepec and Papgayo, though the positive anomalies are typically of larger amplitude, consistent with the calculations of Umatani and Yamagata (1991) and McCreary et al. (1989). Much of the variability in 50- to 100-day SSH on 10°N appears to be related to anticyclonic eddies propagating southwestward from the Gulf of Tehuantepec, consistent with the observations of Giese et al. (1994). The NECC impinges on the eastern boundary around December/January, though our computation of the geostrophic flow extends to within

Figure 4-18: 50- to 100-day SSH anomaly (filled color contours). The contour interval is 1 cm and the color scale spans $\pm$ 8 cm. Eastward flow speeds are contoured (grey lines) at speeds of 10, 15, and 25 cm/s. $U/\beta L_D^2$ (Equation 4.7) is contoured at values of 0.4, 0.5, 0.6, and 0.7 (black lines) and at values of 0.8, 0.9, and 1 (pink lines).
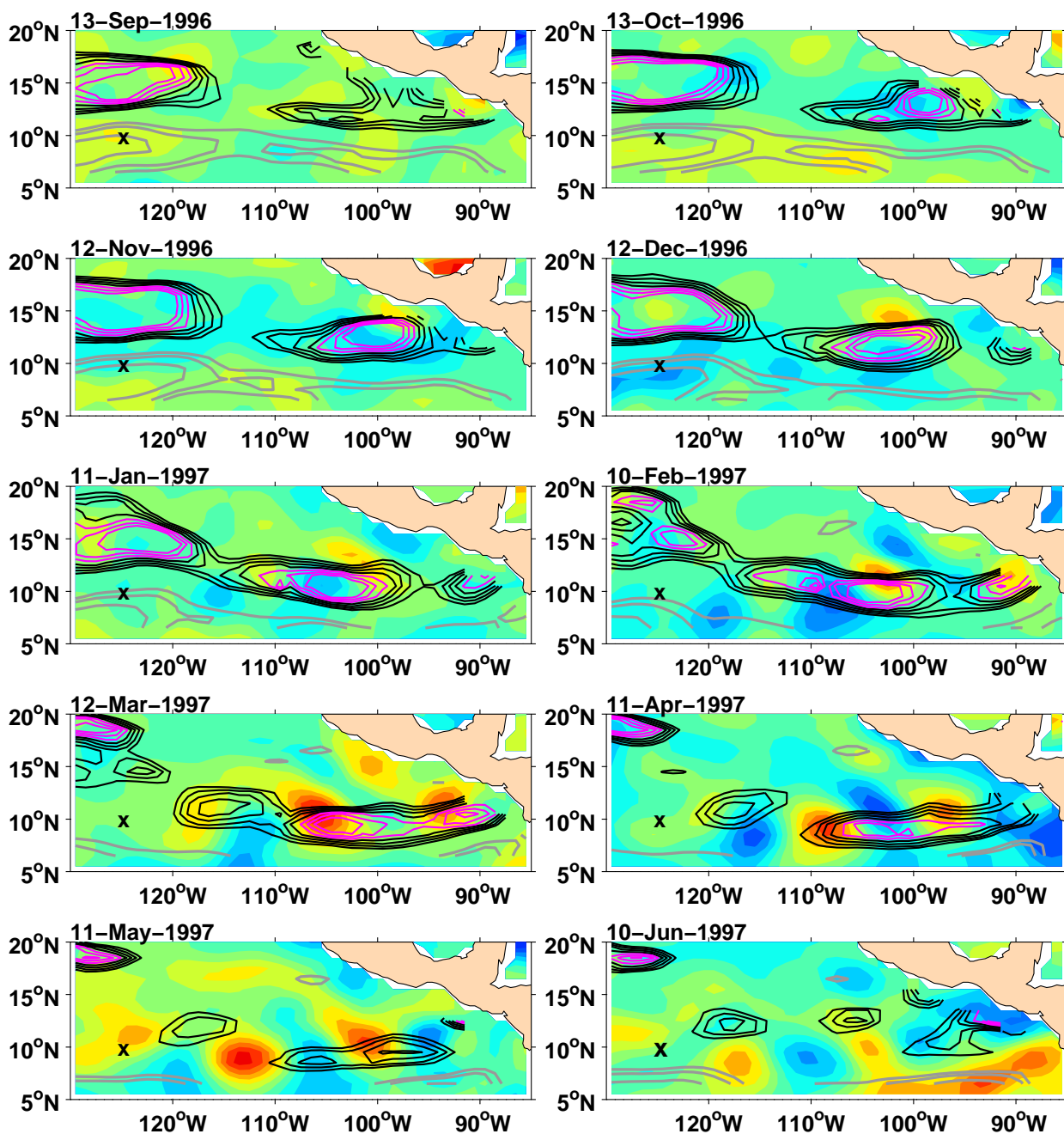
Figure 4-19: 50- to 100-day SSH anomaly (filled color contours). The contour interval is 1 cm and the color scale spans $\pm$ 8 cm. Eastward flow speeds are contoured (grey lines) at speeds of 10, 15, and 25 cm/s. $U/\beta L_D^2$ (Equation 4.7) is contoured at values of 0.4, 0.5, 0.6, and 0.7 (black lines) and at values of 0.8, 0.9, and 1 (pink lines).
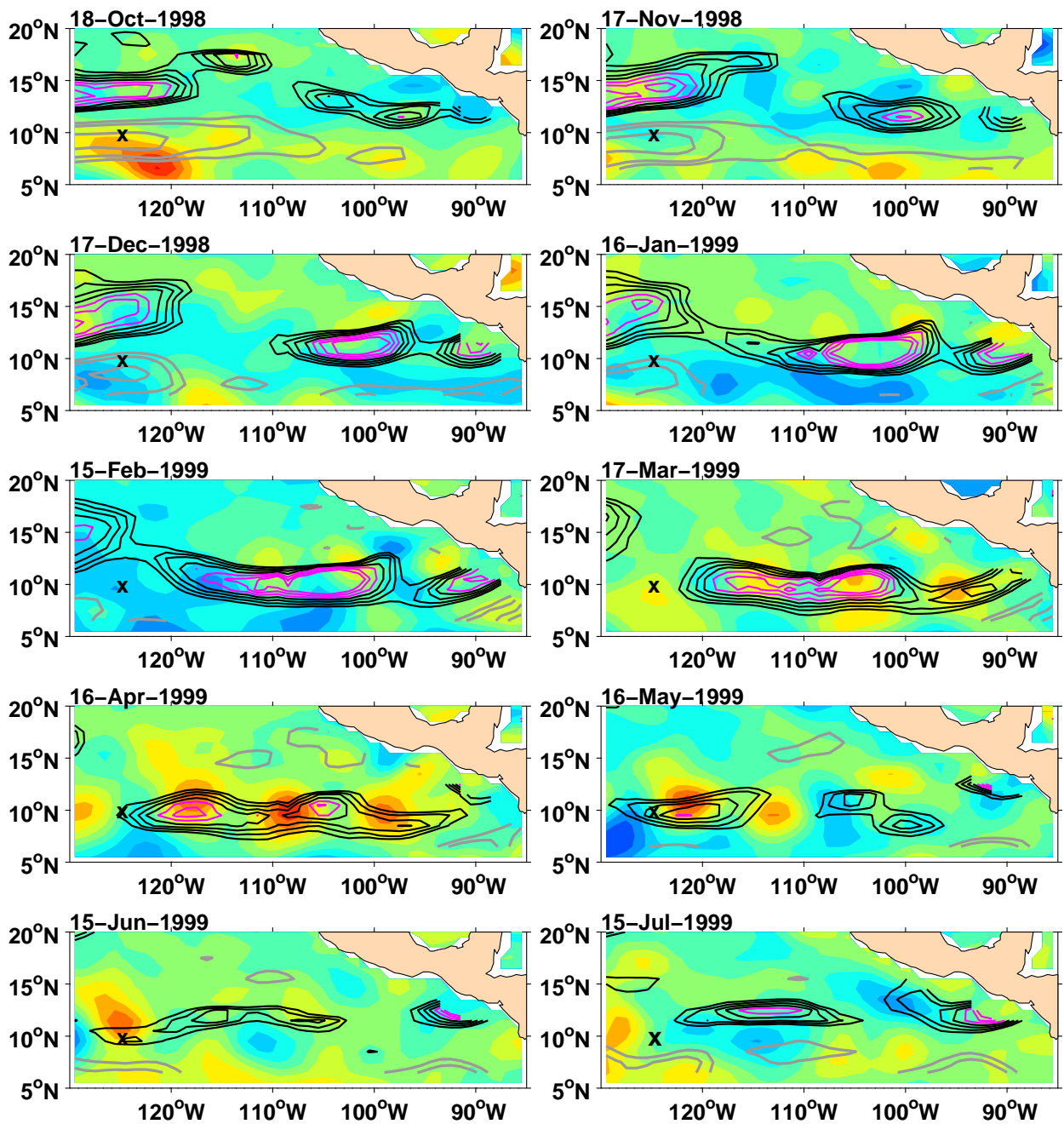
only about 2° of the coast. For a northward flow speed of 20 cm/s, it would take about 15 days for water to travel from 7°N to 11°N; during both of the seasons shown, anticyclonic eddies appear to form near 11°N within about a month of the NECC retroflection. However, the time of retroflection from the images is subject to considerable uncertainty, and it is difficult to assess whether the anticyclonic eddy formation is due to retroflection or wind forcing without further analysis. It is difficult to reliably identify Rossby waves radiating from intraseasonal Kelvin waves at the coast by inspection of the SSH imagery. Still, there are times (e.g., May and July frames of 1999 and other times not shown) when the images give the impression of large scale, coherent coastal sea level variability radiating to the west.

The eastern branch of the NEC (east of about 120°W; as indicated by contours of $U/\beta L_D^2$) is typically weaker and farther north during September-December than during January-March, consistent with Wyrtki's (1975) analysis of hydrographic data. (Note that, for a given value of U, $U/\beta L_D^2$ will be larger at higher latitudes because both β and L_D tend to decrease to the north.) Around the time of peak 50- to 100-day amplitude (i.e., roughly March-May), the eastern branch of the NEC weakens considerably, decreasing in speed by a factor of two or more.

The amplitude of the eddies increases as the eddies move away from the coast, reaching maximum amplitudes on 10-12°N between 100-120°W between March and May, consistent with the analysis along 10°N for 1993-2001 in Section 4.4. In this region, systematic growth of eddies occurs almost exclusively while the eddies are in contact with parts of the NEC that meet the criterion for baroclinic instability. The variability appears to become more spatially organized as the NEC reaches peak intensity around January/February, about two months before the peak eddy amplitudes are reached. In addition, there are growing eddies that do not appear to have come from the eastern boundary. For example, the eddy that is first identifiable near 12°N, 108°W on January 16, 1999 intensifies, along with the other eddies in contact with the "critical" NEC, and propagates westward past the mooring site during June 1999. Another such example is the eddy forming at 12°N, 111°W on January 11, 1997. The eddies reach peak amplitudes within about two months of peak flow speeds in the eastern branch of the NEC, and the NEC weakens as the eddies intensify. By about June, the eastern branch of the NEC almost completely disappears, and the eddies rapidly decay and/or disperse. In most years, the eddies are virtually unidentifiable by July.

The fact that the NEC weakens as the eddies grow suggests that the eddies may be
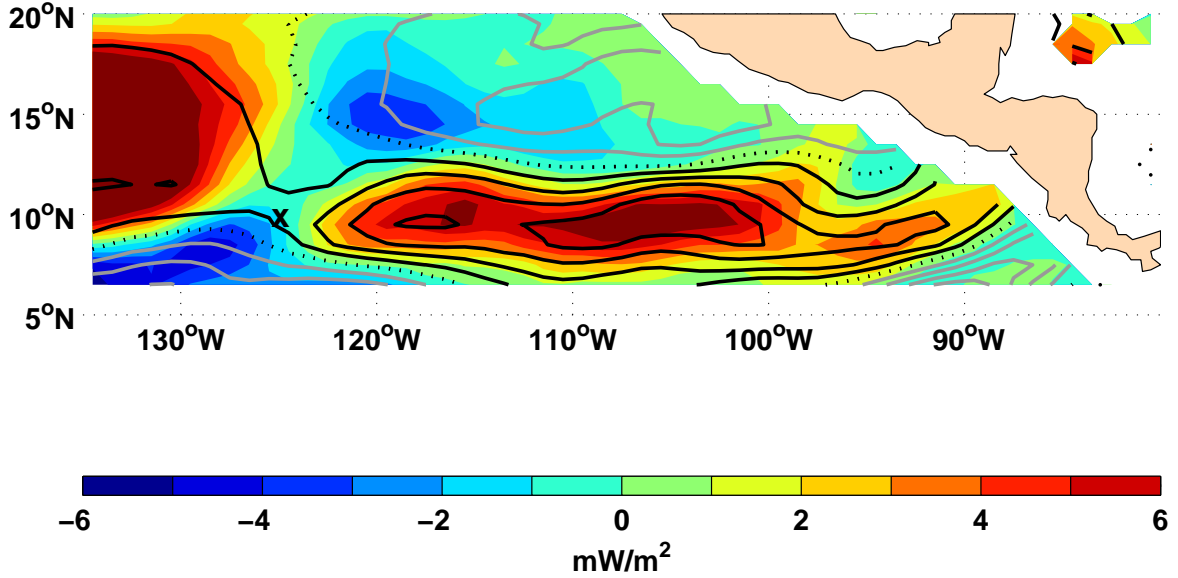
Figure 4-20: Mean work by the wind on the seasonally varying geostrophic flow ($< \vec{\tau} \cdot \vec{u_g}^{\,slow} >$) over the period January 1-June 15, 1999. Contours of the mean zonal flow during the period are overlaid at intervals of 4 cm/s; eastward zonal flows are indicated by grey contours and the zero contour is dashed.

extracting energy from the low frequency zonal currents. However, a number of other mechanisms could explain the weakening of the NEC. One likely mechanism is direct wind forcing. Kessler (2002) showed that the weakening of the climatological NECC near 7°N, 110°W is due to direct wind forcing. One way of determining whether the weakening of the NEC observed between January and June is also due to direct wind forcing is to compute the wind energy input to the geostrophic flow over this time period. If the wind energy input is negative, then the wind works to decrease the energy of the flow and the observed decrease in strength of the NEC could be explained by direct wind forcing. We take the wind work on the geostrophic flow to be given by (Stern, 1975; Fofonoff, 1981; Wunsch, 1998)

$$W = < \vec{\tau} \cdot \vec{u_g} > = < \vec{\tau} \cdot \vec{u_g}^{\,slow} > + < \vec{\tau} \cdot \vec{u_g}^{\,rapid} >, \tag{4.8}$$

where the brackets denote a time average over January-June and $\vec{\tau}$ is the wind stress. The second equality follows from a trivial modification to Wunsch's (1998) approach, made to distinguish between the eddies ($\vec{u_g}^{\,rapid}$, timescales less than 100 d) and the seasonally-varying geostrophic flow ($\vec{u_g}^{\,slow}$, timescales greater than 100 d). Derivation of this expression as-

100

sumes that the dominant dynamics are geostrophic and Ekman balance (or Sverdrup balance; Wunsch, 1998) which is probably a decent approximation for the annual mean flow (Kessler, 2002). The surface geostrophic flow was computed from TOPEX/Poseidon and mean dynamic height data as described earlier in this section. We utilized the scatterometer wind stress data from the European Space Agency's ERS2 satellite. For 1997 (not shown) and 1999 (Figure 4-20), the work by the wind on the eastern branch of the NEC is positive with values of a few mW/m^2, comparable to the global average value of wind work on the geostrophic flow estimated by Wunsch (1998). For comparison, the estimated work by the wind on the eddies, averaged over 10-13°N and 95-120°W, is about -0.013 mW/m^2 in 1997 and about 0.013 mW/m^2 in 1999; both values are a few hundred times smaller than the energy input to the seasonally-varying geostrophic flow. In retrospect, it is not surprising that the wind work on the NEC should be positive, since the trade winds and the NEC are generally in the same direction. The tendency of the wind to strengthen the NEC near 10°N, 105°W is consistent with Kessler's (2002) interpretation of the mean dynamical balance of the region, in which the downwelling-favorable curl($\vec{\tau}/f$) signal extending from the Gulf of Tehuantepec strengthens the thermocline trough near this location. Despite the fact that the wind stress acted to increase the energy of the eastern branch of the NEC over the period January-June, the current speed (and energy) decreased dramatically. One plausible explanation for the decrease in strength of the current is energy extraction by the growing eddies, but examination of one term in the energy balance is far short of a complete energy budget. Vertical mixing or horizontal advection of energy by the mean flow could cause the current to decrease even as the wind works to increase the energy of the current. Still, we can safely infer that direct wind forcing cannot be responsible for observed decrease in energy of the current.

The evidence given above suggests that baroclinic instability of the eastern branch of the NEC can explain the timing and location of the observed intraseasonal variability, and it was argued in Section 4.6.1 that the observed dispersion characteristics are those of first baroclinic-mode Rossby waves propagating in the NEC. These two interpretations are, strictly speaking, inconsistent. Disturbances growing within a baroclinically unstable flow are not free Rossby waves, and while the instabilities may propagate, their dispersion characteristics should be different from those of Rossby waves.

The inconsistency between the two interpretations is not as profound as it may at first

appear, as can be made clear by consideration of the dispersion relation for the two-layer model (Gill et al., 1974) and its relationship to the dispersion relation for the 1.5-layer model (Figure 4-21). The dispersion curves were evaluated using parameters appropriate to the region ($g' = 0.06$ m/s^2, $H_1 = 100$ m, $H_2 = 4000$ m), and the particular choice of the upper-layer zonal flow used in Figure 4-21 was $U_1 = 30$ cm/s. (The choice of U_1 affects the growth rate and, to a lesser extent, the unstable wavenumbers and frequencies, but the choice is otherwise irrelevant to this discussion. Note that the two-layer model is not particularly good at reproducing the growth rate and unstable wavenumbers and frequencies in comparison to continuously stratified models (Gill et al., 1974).) Because the upper layer is much thinner than the lower layer, the dispersion curve derived from the 1.5-layer model provides a good approximation to the real part of the dispersion curve for baroclinic motions in the two-layer model. At a given wavenumber, the largest difference in frequency for the two models is about 5%. In other words, the unstable modes in the two-layer model have propagation characteristics that are very close to those of free Rossby waves in the 1.5-layer model. An important difference between the two representations is that the two-layer model predicts a smaller group velocity for the unstable modes. The observed dispersion characteristics of sea surface zonal slope (i.e., the power spectrum; Figure 4-16) do not allow, and are not expected to allow, identification of such a "flat" region of the dispersion characteristics.

Thus, the observations are consistent with both interpretations, but the two interpretations may be inconsistent with one another. However, the two interpretations are not necessarily inconsistent with one another. The instability may occur for a relatively short time (on the order of a wave period), and, thus, during most of the time that the intraseasonal mesoscale variability is observed, instability may not be occurring. The similarity of the dispersion curves for the unstable modes and free Rossby waves suggests that, after the zonal current is rendered stable by the instability, the disturbances that gained energy during the instability should continue propagating as free Rossby waves. This interpretation is supported to some extent by the fact that the mean flow speed required in Equation 4.5 to produce a good fit to the observed distribution of power is less than the critical flow speed for the two-layer model, suggesting that the average dispersion characteristics observed are dominated not by the growing unstable modes, but rather by the propagating disturbances that result from the transient growth.
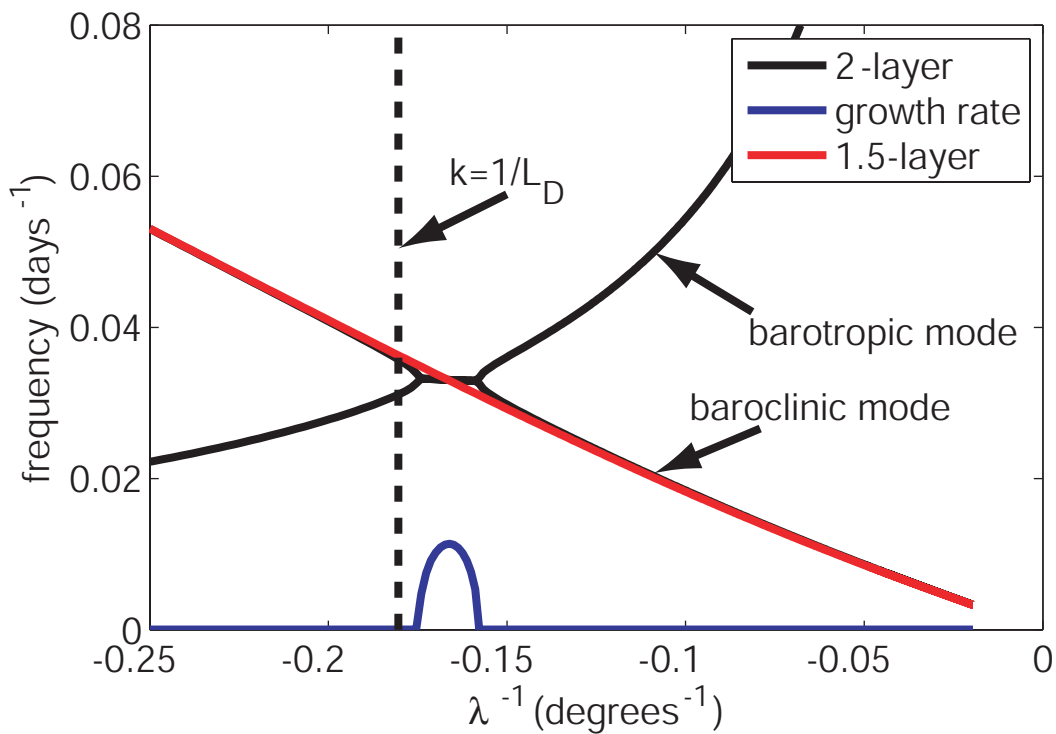
Figure 4-21: Dispersion curves for the two-layer and 1.5-layer models. The black curves are the real part of the dispersion curves for the two-layer model and indicate how disturbances propagate. The blue curve is the imaginary part of the two-layer dispersion relation (or, the growth rate of unstable modes). In the parameter regime relevant to the eastern tropical Pacific, there is very little difference in the propagation characteristics of baroclinic motions in the two-layer and 1.5-layer models, even for the modes that are unstable in the two-layer model.

4.7 Conclusion

We have examined the observed characteristics of intraseasonal variability near 10°N in the eastern tropical Pacific using in situ and satellite data. The observations show that both wavelike and eddy-like motions contribute to the intraseasonal variability. We found that the variability is annually modulated, with strongest amplitudes tending to occur around April, but there is also substantial spatial and interannual variability in the intraseasonal signal. Besides being of potential importance for meridional heat transport and air-sea interaction, this variability poses a sampling challenge to those working to study air-sea coupling and other processes in the vicinity of 10°N in the eastern Pacific.

When viewed on a zonal section along 10°N, the amplitude of the intraseasonal variability seems to increase too rapidly to be explained by due-westward energy propagation. Some intraseasonal eddies travel southwestward to 10°N from near the Gulf of Tehuantepec, and this can explain part of the rapid increase of intraseasonal variability on 10°N. In addition, some of these eddies appear to intensify after coming into contact with a potentially baro-clinically unstable NEC. The wavelike intraseasonal variability observed at the mooring site during the first half of 1998 modified SST by meridional advection along the slowly evolving horizontal surface temperature gradient. The strong eddies observed near the coast are also known to produce strong SST signatures by advection and also by upwelling/downwelling and entrainment during their generation stage (e.g. McCreary et al., 1989).

We now briefly summarize our findings regarding the generation mechanism for the intraseasonal variability seen near 10°N in the eastern tropical Pacific. We have shown, as have others (e.g., Giese et al., 1994), that eddies emanate from near the Gulfs of Tehuantepec and Papagayo and propagate westward along 10-13°N. Under monthly mean climatological wind forcing, the GCM output of Jochum and Murtugudde (2004) and Umatani and Yamagata (1991) shows intraseasonal variability near 10°N, which suggests that intraseasonal fluctuations in the mountain gap winds (i.e., the hypothesis of Giese et al., 1994) are not fundamental to the existence of the variability, though the wind fluctuations certainly may play an important role in determining the details of the observed variability. Eddies are generated near the eastern boundary with remarkably high frequency; for example, Gonzalez-Silvera et al. (2004) identified 18 eddies being shed from the Gulfs of Tehauntepec and Papagayo during the 5 month period of November 1998 to March 1999. It remains unclear how these

frequently generated eddies might contribute to intraseasonal variability near 10°N. We have not endeavored to determine whether the intraseasonal eddies observed at the eastern boundary are forced by the wind or are associated with retroflection, though there is substantial evidence for wind forced eddies (e.g. Stumpf and Legeckis, 1977; McCreary et al., 1989; Clarke, 1988) and the Gulf of Tehuantepec seems rather far from the NECC for retroflection to make sense as a generation mechanism there. Nonetheless, Ballestero and Coen (2004) have suggested that their observations near the Gulf of Papagayo are consistent with both interpretations.

Our analysis suggests that the eddies typically strengthen in March-May, well away from the coast and while in contact with a potentially baroclinically unstable NEC. While the eddies grow, the NEC weakens considerably, despite continued energy input from the wind. We have not attempted to determine whether barotropic instability might also contribute to the disturbances. It is worth noting that Jochum and Malanotte-Rizzoli (2003) examined variability at similar frequencies and scales in the northern tropical Atlantic of a GCM and concluded that both baroclinic and barotropic instability contributed energy to those disturbances. One interpretation of the existing literature and the observations presented here is that wind forcing (and possibly other mechanisms) generates disturbances that propagate into an unstable NEC. As the disturbances draw energy from the current, the current weakens considerably. When the eastern branch of the NEC stabilizes, the disturbances rapidly decay and disperse, and the stage is set for the next annual cycle. We have not been able to fully evaluate the various hypotheses for the intraseasonal variability here, but the observations suggest that baroclinic instability contributes to the intraseasonal variability.

Chapter 5

Cloud signals associated with oceanic Rossby waves on 10°N

5.1 Air-sea interaction at the oceanic mesoscale

Following the development of microwave techniques for accurate measurement of sea surface temperature (SST) and surface winds with high spatial and temporal resolution from satellites, much attention has been focused on air-sea interaction at spatial scales smaller than the atmospheric synoptic scale. Most of this attention has been devoted to the relationship between SST and surface wind speed (Xie et al., 1998; Hashizume et al., 2001; Xie, 2004; O'Neill et al., 2003, 2005; Small et al., 2005). This chapter examines coherent variability at the oceanic mesoscale in SST and some satellite-derived measures of atmospheric convection. Since it seems likely that variations in surface wind speed and atmospheric convection associated with oceanic mesoscale SST variability may be symptoms of a single atmospheric response to spatial variations in SST, it is worthwhile to review the relatively well-studied relationship between variations in wind speed and SST at the oceanic mesoscale.

Warm mesoscale SST anomalies are associated with relatively higher wind speeds (e.g., Hayes et al., 1989; Hashizume et al., 2001; Xie, 2004; O'Neill et al., 2003, 2005; Small et al., 2005). This relationship is believed to result in part from variations in the static stability of the atmospheric boundary layer (ABL) caused by surface heat flux variations associated with the varying SST field. Destabilization of the ABL leads to increased turbulence in the boundary layer and entrainment of faster-moving air from aloft. Mesoscale SST variations

107

can also lead to variations in the horizontal pressure gradient in the atmospheric boundary layer (e.g., Cronin et al., 200X) that can modulate the surface wind field. The relative importance of these and other mechanisms (Spall, submitted manuscript) is a subject of active study, and the momentum balance leading to the observed relationship between SST and wind speed is likely to depend on several factors, such as latitude, mean wind speed, and the scale of SST gradients (Spall, submitted manuscript; Small et al., submitted manuscript).

In the tropics and subtropics (40°N to 40°S), SST and wind speed variations at the oceanic mesoscale ($< 10°$ longitude) are in phase, with the wind speed response being 0.5-1.5 ms^{-1} per °C of SST change (Small et al., 2005). The mesoscale SST signals propagate westward at speeds consistent with the phase speeds of first baroclinic-mode Rossby waves, and these SST signals are accompanied by co-propagating features in the surface wind speed. The phase relationship between the westward propagating SST signals and sea surface height fluctuations indicates that the SST fluctuations result largely from meridional advection of the mean temperature gradient (Leeuwenburgh and Stammer, 2001; Small et al., 2005).

The relationship between mesoscale SST variations and surface wind speed was first detected in association with tropical instability waves (Hayes et al., 1989), which have an SST signal of several degrees. Associated variations in properties of clouds and the ABL (Deser et al., 1993; Hashizume et al., 2001) have been cited as evidence supporting the role of the ABL destabilization mechanism in producing a surface wind speed signal (Hashizume et al., 2001; Xie, 2004).

A relationship between mesoscale SST variations and atmospheric convection has been noted away from the equator, as well. For example, correlated oceanic mesoscale variations in SST, wind speed, and cloud liquid water (CLW) have been detected in the Agulhas Return Current region (southwest of Africa near $\sim$45°S) where warm SST perturbations are associated with higher winds and larger amounts of CLW (O'Neill et al., 2005). In the eastern tropical Pacific Inter-Tropical Convergence Zone (ITCZ) region, the mesoscale patch of cool SST associated with the Costa Rica Dome (a mesoscale doming of the thermocline), although only about 0.5°C cooler than the surrounding sea surface, reduces the local precipitation by about a factor of two relative to the surrounding area (Xie et al., 2005).

In Chapter 3, it was noted that there were intraseasonal SST variations at the 10°N site caused primarily by meridional advection, and these SST variations appeared to be associated with variations in solar heating (as well as latent and sensible surface heat fluxes). Because

the heat flux signal was not large enough to drive the signal in mixed-layer temperature, it was suggested that variations in insolation may be driven by the SST signal. In Chapter 4, the oceanic motions responsible for the meridional velocity signal were investigated in detail. The distribution of power in sea surface zonal slope was examined, and it was argued that these motions can be interpreted as first baroclinic-mode Rossby waves.

The relationship between the SST fluctuations driven by Rossby waves and the surface solar radiation suggests that the oceanic Rossby waves may influence atmospheric convection. This chapter examines the impact on tropical convection of SST variability driven by oceanic Rossby waves. Specifically, the relationship between westward propagating SST fluctuations in the oceanic Rossby wave wavenumber-frequency band and cloud liquid water is considered, and this relationship is corroborated by examination of International Satellite Cloud Climatology (ISCCP) surface solar radiation and data from the Geostationary Operational Environmental Satellite-9 (GOES-9). Although it is found that much of the variability in solar radiation at the buoy is linked to atmospheric variability of larger scales and is therefore not linked to the local SST variations, a statistically significant relationship between SST fluctuations and cloud properties (cloud liquid water and surface solar radiation) is detected in the Rossby wave band.

5.2   Data

This study uses estimates of SST from the Tropical Microwave Imager (TMI) instrument aboard the Tropical Rainfall Measuring Mission (TRMM) satellite (Kummerow et al., 1998). The TMI measures microwave radiation passively in nine channels and is derived from the Special Sensor Microwave/Imager (SSM/I) instrument that has been deployed on U.S. Defense Meteorological Satellite Program (DMSP) satellites since 1987. The primary difference between the TMI and SSM/I sensors is the inclusion in the TMI package of 10.7-GHz channels for measuring horizontally and vertically polarized radiation (Kummerow et al., 1998), which allows accurate estimation of SST because microwaves at frequencies lower than about 12-GHz can penetrate clouds and atmospheric aerosols with little attenuation (Wentz et al., 1999). SST is estimated from the microwave measurements using a physically-based algorithm (Wentz and Meissner, 2000) that is an extension of the Wentz (1997) algorithm for estimation of geophysical parameters from the SSM/I microwave radiance measurements.

The microwave measurements by the TMI and SSM/I instruments also allow estimation of columnar cloud liquid water (CLW). Cloud liquid water was estimated using the physically-based Wentz (1997) algorithm developed for the SSM/I instrument. The orbit patterns of the satellites carrying the TMI and SSM/I instruments allow complete spatial coverage over about a two-day period, so some temporal averaging is required to produce a field without large spatial data gaps. Weekly-average and daily, three-day running-average cloud liquid water estimates from the TMI and SSM/I instruments and SST estimates from TMI were obtained from Remote Sensing Systems (www.remss.com) at $0.25° \times 0.25°$ spatial resolution. This study utilizes the three-day running average data for analysis and display in the time-space domain and the weekly average fields for calculations in the spectral domain.

Individual storms in the tropics travel at speeds of several m/s (or several hundred km per day), so the two-day period required for complete spatial coverage can lead to poor sampling of an individual storm. This problem can be clearly seen by inspection of the weekly average CLW from TMI for an individual storm. For example, Hurricane Darby of 1998 appears in a few discrete locations (Figure 5-1a). To alleviate this sampling problem and produce a better representation of the track of individual weather systems, the weekly and three-day average CLW fields from the TMI and SSM/I instruments aboard the DMSP F11, F13, and F14 satellites were averaged (Figure 5-1b). A similar procedure was used by Hashizume et al. (2001) to investigate the relationship between SST and CLW for eastern Pacific tropical instability waves.

For examination of the relationship between surface solar radiation and SST, the surface solar radiation from the ISCCP radiative flux data set (Rossow and Zhang, 1995; Zhang et al., 1995; Zhang et al., 2004) was used. This radiation product uses a variety of satellite and other observations of the properties of the atmosphere and clouds, together with a radiative transfer model, to estimate the upwelling and downwelling radiation at five levels spanning the surface to the top of the atmosphere with a resolution of 280 km and three hours (Zhang et al., 2004). Comparison to observations suggests that the surface radiation fields have an accuracy of 10-15 W/m^2 for monthly averages (Zhang et al., 2004). The net surface solar radiation field from the ISCCP product was averaged to a daily time-base and was linearly interpolated to a $1° \times 1°$ spatial grid to facilitate comparison with the SST product described below.

For cross-spectral calculations against the ISCCP radiation fields, a time series of SST
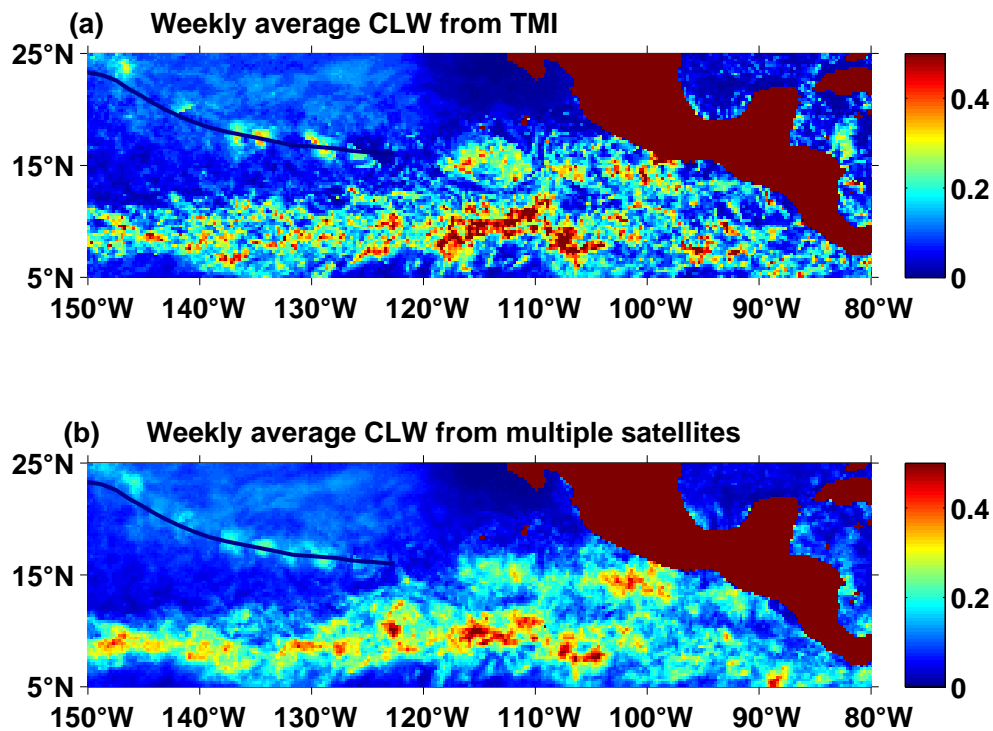
Figure 5-1: Upper panel: One-week average of CLW (mm) from the TMI instrument for the week ending on 1 August, 1998. Lower panel: One-week average of CLW (mm) constructed by averaging weekly estimates from the TMI instrument and three SSM/I instruments that were in orbit at the same time. In both panels, the black line shows the estimated track of Hurricane Darby during that time period (from the U.S. National Hurricane Center). The averaging of CLW from several satellites was carried out to improve the representation of the mean CLW for individual weather systems and to generally improve the accuracy the CLW estimate.

going back to 1984 was required. Examination of mesoscale SST variability in a few available products suggested that the objectively analyzed SST field of Yu et al. (2004) resolves the SST variability adequately. This SST product is derived primarily from the AVHRR NOAA-NASA Oceans Pathfinder SST product (Brown et al., 1993) at 9 km, daily resolution. These observations are combined by variational objective analysis with the SST fields for the NCEP2 reanalysis product (Kanamitsu et al., 2000) and the ECMWF operational analysis, but the AVHRR SST field is weighted six times more heavily than the NCEP2 and ECMWF SST fields. Comparison of the Yu et al. (2004) SST analysis to data from the TMI instrument suggests that mesoscale signals in SST are resolved but are somewhat smoother than those seen in the TMI data. Since the spatial resolution of the ISCCP radiation field is 2.5°, the smoothing of scales less than 5° longitude in the SST product is acceptable for the present purpose.

Data from the visible and infrared imager aboard the GOES-9 satellite are also used (Menzel and Purdom, 1994; Weinreb et al., 1997) in situations where the 2.5° resolution of the ISCCP product is insufficient. Specifically, data from channels measuring outgoing radiation in the 0.52-0.72 μm wavelength band (visible channel) and 10.2-11.2 μm wavelength band (an infrared channel) are used (Menzel and Purdom, 1994). These data were obtained for the period 3 February-25 July of 1998 at a resolution of 3 hours and 0.1° × 0.1° spatial resolution from the Joint Office of Science Support at UCAR. The visible channel data is normalized by the solar constant and gives a measure of the solar radiation reflected to space after correcting for variations in solar zenith angle. Because the visible channel returns no useful data at night, only the local noontime value (∼2100 UTC) from the visible channel is used here. The infrared channel gives a measure of cloud-top temperature and is a useful indication of depth of convection.

Aliasing of diurnal or other high-frequency variability into the wavelength and period band of oceanic Rossby waves is a concern for the various satellite data products used here. The use of several satellite data sets is motivated by this and concerns about the possibility of other systematic errors in the satellite data. The various fields used come from satellites with markedly different orbit patterns and sampling strategies, and the results from the various data sets will be shown to be consistent. Use of multiple data sets alleviates concerns about systematic sampling and measurement errors in any particular data set. In addition, the fidelity of the TMI SST in representing the Rossby wave signal observed at the mooring
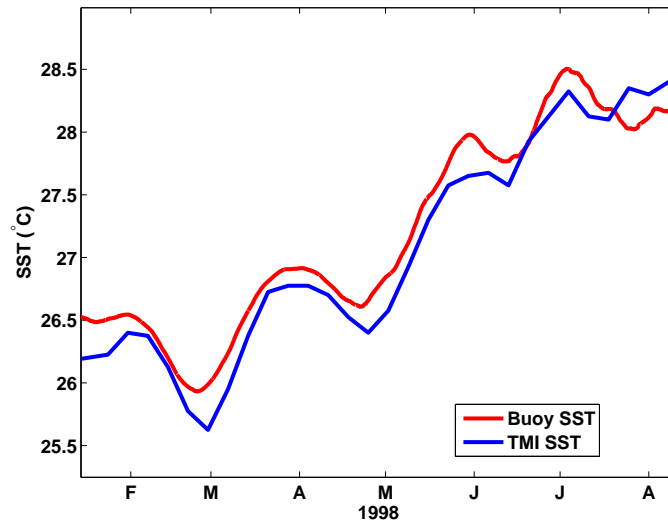
Figure 5-2: Comparison of SST from a buoy moored at 10°N, 125°W to SST at the same location from the TMI instrument. The buoy SST a 21-day running average of hourly-average data; the TMI SST is a 21-day average of weekly-average data. The intraseasonal period band in the TMI data shows no clear evidence of contamination by aliasing of unresolved variability.

Data product	Spatial resolution	Temporal resolution	Further processing (time domain)	Further processing (spectral domain)
TMI and SSM/I	$0.25° \times 0.25°$	daily, 3-day running average for time domain; 7-day average for spectra	3-week running average; 1.5° zonal running average	none
ISCCP radiation	$2.5° \times 2.5°$	3 hour average	N/A	daily average; interpolation to $1° \times 1°$
O-A SST (Yu et al., 2004)	$1° \times 1°$	daily average	N/A	none
GOES visible	$0.1° \times 0.1°$	3 hour	subsampled once-daily	N/A
GOES infrared	$0.1° \times 0.1°$	3 hour	none	N/A

Table 5.1: Summary of resolution of data products used and further processing applied for calculations in the time-space domain (Section 5.4) and wavenumber-frequency domain (Section 5.5).

(Chapter 4) is good (Figure 5-2); comparison to the in situ SST shows that this Rossby wave signal in the TMI SST data (discussed below) is not a result of aliasing of high-frequency variability. Though a similar test cannot be performed for the CLW estimate, it is unlikely that a signal in CLW coherent with the Rossby-wave SST signal could be a spurious result of the satellite's sampling pattern. The spatial and temporal resolution of the various data sets and additional processing applied prior to analysis is summarized in Table 5.1.

113

5.3 SST fluctuations along 10°N in the eastern Pacific Ocean

A number of previous studies have noted the widespread presence of westward propagating SST anomalies (e.g., relative to a zonal average of SST) throughout much of the world oceans, and there is mounting evidence that these mesoscale SST variations are caused primarily by meridional advection along the mean temperature gradient (e.g., Hill et al., 2000; Leeuwenburgh and Stammer, 2001; Small et al., 2005). The temperature balance analyses in Chapters 3 and 4 support this interpretation for the mesoscale SST anomalies observed at the 10°N mooring site.

The evolution of SST along 10°N during 1998 is depicted in Figure 5-3a, as measured by the TMI instrument. Most of the variance in SST is at large spatial and temporal scales (basin and seasonal scales). However, some relatively small variations in SST (O(0.5°C)) can be seen to propagate westward; for example, the SST variations at the 10°N, 125°W mooring site examined in Chapters 3 and 4 are clearly visible during March-June.

These westward propagating SST variations can be seen more clearly when a longitudinal high-pass filter is applied (Figure 5-3b). (For SST and other high-pass filtered fields in this chapter, the filtering is accomplished by subtracting a zonal running average from the data to remove variability with zonal scales exceeding 10° longitude.) Westward propagating signals can be seen throughout the domain in the the filtered SST, though the propagation characteristics vary through time. However, there are times when the filtered SST signals do not exhibit clear westward propagation, particularly during the ITCZ season spanning roughly July-December.

5.4 Time-space domain

This analysis examines the relationship between mesoscale SST signals and cloud properties, and is motivated by in situ buoy observations of the relation between solar radiation and SST variations driven by oceanic Rossby waves. While the buoy observations are suggestive of a relationship, a more complete assessment should examine the relationship in time and space. Ideally, one would look for the Rossby wave signal in satellite solar radiation data, but the ISCCP surface solar radiation product is distributed on a spatial grid of 2.5°, so the ~5°

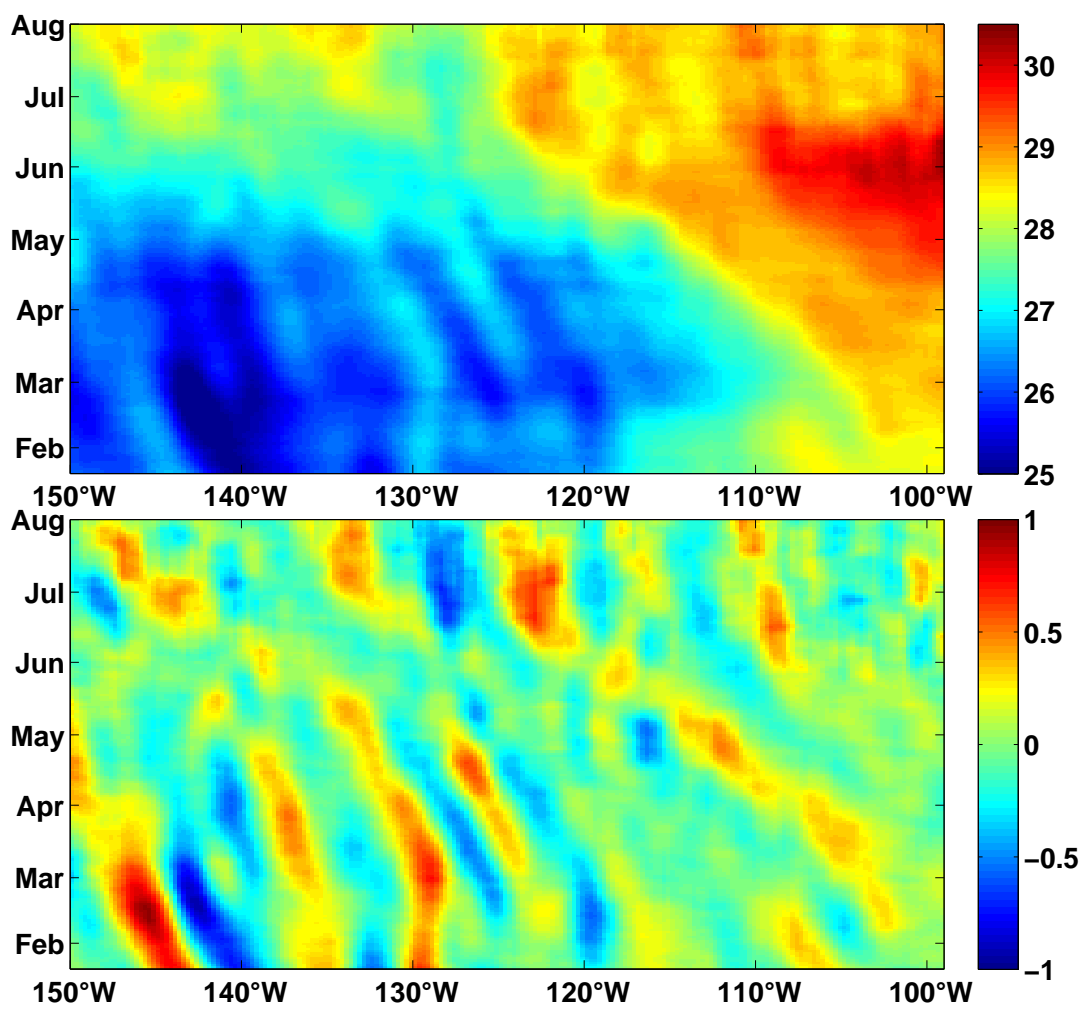Figure 5-3: Upper panel: Longitude-time diagram of SST (°C) along 10.125°N during 1998 from the TMI instrument. Lower panel: The same, except a 10° longitude zonal running average has been removed to emphasize the mesoscale SST variability.

spatial scale of the Rossby waves observed at the mooring is not well-resolved. However, measurements of outgoing visible radiation from the GOES-9 satellite should be closely related to the surface solar radiation, since the surface solar radiation is set by variations in the radiation reflected to space and that absorbed by the atmosphere.

The visible reflectivity, R, of clouds measured from space by the GOES satellite can be used to construct a crude estimate of the daily-average surface solar radiation Q_s as,

$$Q_s = Q_{clear}(1 - R - \alpha), \tag{5.1}$$

where Q_{clear} is the daily-average clear-sky incoming solar radiation and α is the sea surface albedo. This formulation assumes that, in the absence of clouds, the incoming solar radiation is Q_{clear}, and the primary effect of clouds is to reflect radiation to space. This formulation neglects the absorbtion of shortwave radiation by cloud droplets.

Under assumptions of a daily-average clear-sky incoming solar radiation of 310 W/m^2 and a daily-average surface albedo of 7% (e.g., Payne, 1972), the GOES-9 visible radiation (corrected for solar zenith angle) provides a reasonably good representation of the net solar radiation observed at the buoy (Figure 5-4). The daily-average surface clear-sky solar radiation is known to vary with, among other things, atmospheric aerosol, ozone, and water vapor distributions (e.g., Santamouris et al., 1999) and is thus likely to be time dependent, particularly as the local conditions shift from the dry trade-wind season to the much moister ITCZ season around June. Given the crude nature of this estimate, the correspondence between the buoy-based estimate of the daily-average surface solar radiation and that estimated from the GOES-9 visible radiation is remarkable, and it seems likely that much of the signal in insolation observed at the buoy is due to variations in cloud reflectivity.

With only a few cycles of intraseasonal variations in SST and insolation observed at the buoy, it is not possible to confidently ascribe the variations in insolation to the SST variations. Intraseasonal variations of planetary scale (e.g. the Madden-Julian oscillation) are known to contribute prominently to the variance of atmospheric properties and convection. Thus, a reasonable null hypothesis would be that the SST variations, which have zonal scale of less than 10° longitude, are merely coincidental in time with larger scale atmospheric variations that happen to have a similar periodicity.

Examination of visible reflectivity and SST in longitude and time allows a reliable as-
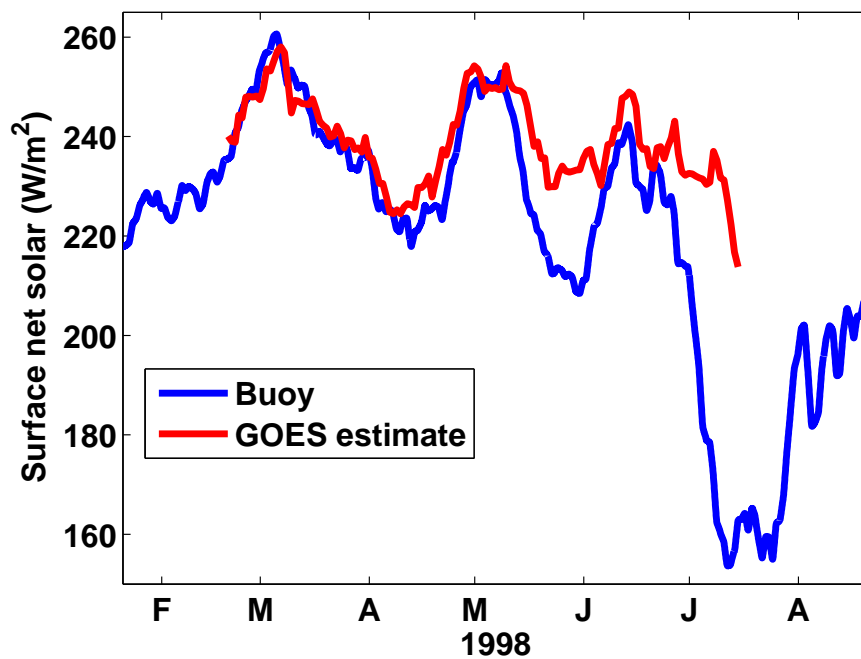
Figure 5-4: Daily-average net surface solar radiation from the buoy measurements (blue line) and a crude estimate of the that obtained from once-daily GOES visible radiation observations (red line), made assuming a daily-average clear sky incoming radiation of 310 W/m^2 and a sea surface albedo of 7%. Both curves have been smoothed with a 21-day running average.

sessment of the extent to which the variations in reflectance are related to the short-scale SST variations at the buoy. Comparison of reflectivity, smoothed by a running average over three weeks and 2° longitude, to the mesoscale SST anomaly suggests that there may be a relationship between westward propagating SST anomalies and reflectivity, with relatively high reflectivity tending to occur over warm SST anomalies (Figure 5-5a). For example, there were three regions of relatively high reflectivity during late-June 1998 between 115°W and 150°W; all three of these regions also exhibited warm SST anomalies. However, large scale atmospheric variability at intraseasonal periods also appears to contribute to the intraseasonal variability at the mooring site. For example, the local temporal minimum in insolation observed at the buoy in late May 1998 (Figure 5-4) corresponds to a maximum in reflectivity during that time spanning about 30° of longitude (Figure 5-5). This maximum in reflectivity is apparently not related to westward propagating SST anomalies.

To separate the contribution of large-scale atmospheric variations in reflectivity from those resulting from mesoscale variations in SST, it is helpful to examine the zonally high-pass filtered reflectivity, which reveals the presence of co-propagating reflectivity and SST anomalies (Figure 5-5b). There is a clear tendency for higher reflectivity over warm SST anomalies. For example, the three well-defined westward propagating warm SST anomalies found on 120-140°W during March and April 1998 are accompanied by high reflectivity anomalies, and the reflectivity is relatively low to the east and west of each of these warm SST anomalies. Still, it is also clear that a substantial fraction of the variance of reflectivity in the filtered field (at periods greater than 21 days and wavelengths smaller than 10°) is unrelated to the local variation in SST.

Examination of cloud liquid water (CLW), another important cloud property, corroborates the notion that high wavenumber variability in convection is affected by SST signals of westward propagating oceanic mesoscale variability. Because the variance and amount of CLW are both much larger at 10°N during ITCZ conditions than during the trade wind season, longitude-time plots of CLW covering both of these seasons are best displayed on a logarithmic scale. For example, there is about a factor of ten increase in CLW along 10°N as local conditions transition from the trade-wind season to the deep-convection dominated ITCZ season around June/July 1998 (Figure 5-6). The base-ten logarithm of CLW, when filtered, exhibits a relation to SST anomalies similar to that of SST and cloud reflectivity (Figures 5-6 and 5-7). A variation, x', in the filtered logarithm of CLW indicates that the
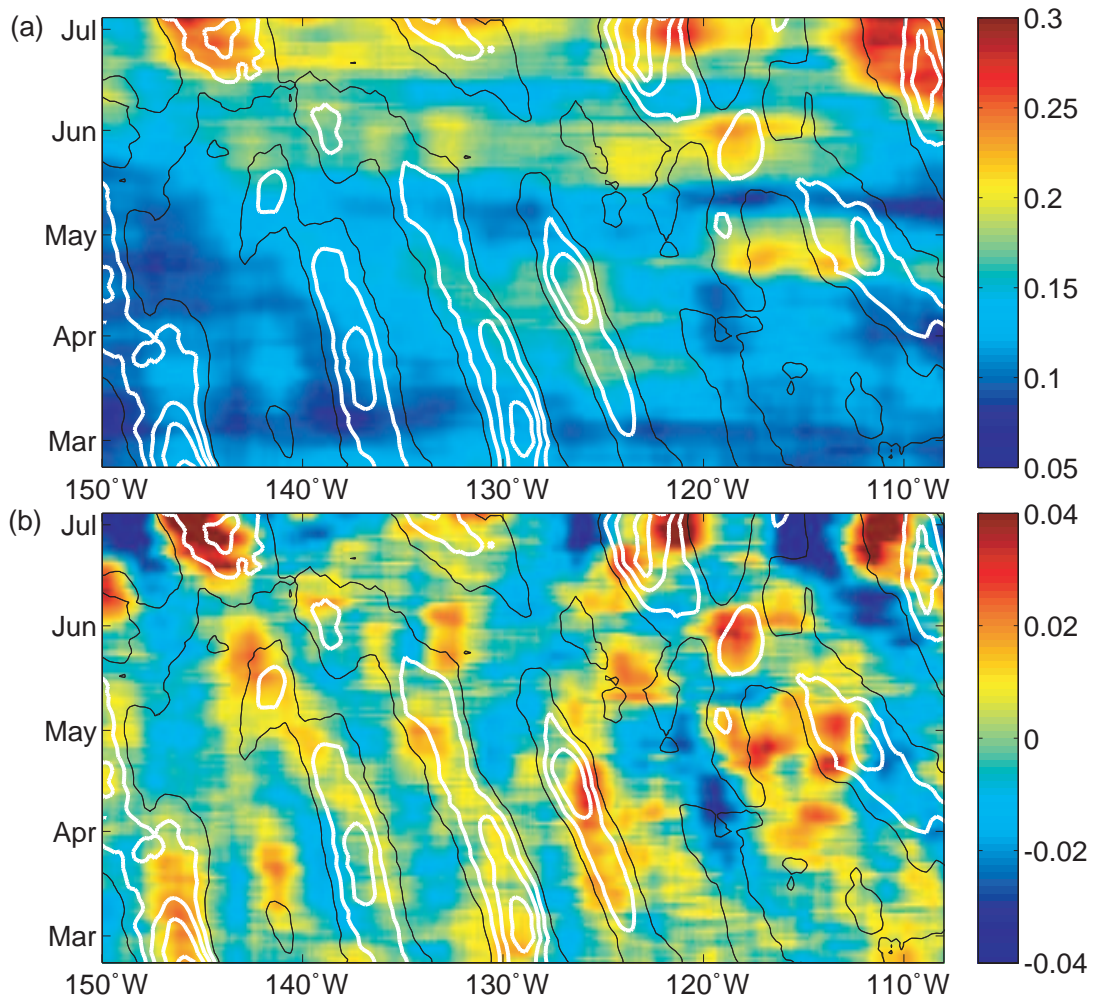
Figure 5-5: (a) Longitude-time diagram of cloud reflectivity (colored) along 10°N during 1998 (from the GOES visible channel). A 21-day running average and a 2° zonal running average have been applied to daily samples. A reflectivity value of 0.2 indicates that 20% of the incident radiation is reflected back to the satellite. Contours of filtered SST anomalies greater than zero (from Figure 5-3) are contoured in white at 0.2°C intervals, and the zero contour is black. (b) Spatially filtered cloud reflectivity (colored) along 10°N during 1998 (from the GOES visible channel). As in (a), warm mesoscale SST anomalies are indicated by white and black contours.

CLW varies by a factor of $10^{x'}$ relative to the $10°$ zonally smoothed representation of CLW[1]. For example, if $x' = 0.1$ at some location, then the CLW is about 1.26 times larger at that location than the value of CLW obtained by using the exponent averaged over the surrounding $10°$ of longitude.

There is a tendency for warm mesoscale SST anomalies to be accompanied by increased CLW; the correlation coefficient for the two filtered fields depicted in Figure 5-6 is 0.30, significant at 95% confidence (accounting for the reduction of degrees of freedom associated with the filtering). Since reflectivity depends not only on CLW, but on other cloud properties such as cloud thickness and the water droplet size distribution, the filtered CLW and reflectivity fields are not expected to be qualitatively identical. However, the similarity of the two fields gives increased confidence that the mesoscale SST variations affect the high wavenumber variability of convection at periods greater than 21 days.

Although it is apparent that a relationship exists between mesoscale SST variations and variations in cloud properties, the significance and quantitative nature of this relationship cannot be assessed by inspection of filtered longitude-time plots like Figures 5-5b and 5-6. In the next subsection, this relationship is quantified using cross-spectral techniques.

5.5 Wavenumber-frequency domain

We now examine in the wavenumber-frequency domain the relationship between SST variations and cloud signals, measured by CLW and ISCCP solar radiation. This allows a quantitative estimate of the coherence of SST with CLW and surface solar radiation in the Rossby wave band and will allow further inference about the cause-effect relationship.

The principal tool for this analysis is computation of the coherence amplitude and phase in wavenumber and frequency. This is accomplished by computing the two-dimensional fast Fourier transform (2DFFT) of the unfiltered longitude-time sections, after removing the mean and tapering the edges of each field to zero using a Hanning window. Then the autospectra and cross-spectrum are formed for the two fields being compared, and each

---

[1]Let $x = \log_{10}(< CLW >)$ where the angle brackets indicate smoothing over 21 days and 1.5° longitude. Then, the filtering applied to x can be expressed as $x = \bar{x} + x'$, where $\bar{x}$ is the zonally smoothed field and x' is the filtered field. So, $< CLW >= 10^{\bar{x}+x'}$. Thus, $< CLW >= 10^{x'}10^{\bar{x}}$ and the filtered field represents the power of 10 by which the smoothed representation of CLW ($10^{\bar{x}}$) must be multiplied by to obtain the unfiltered, original value of $< CLW >$.
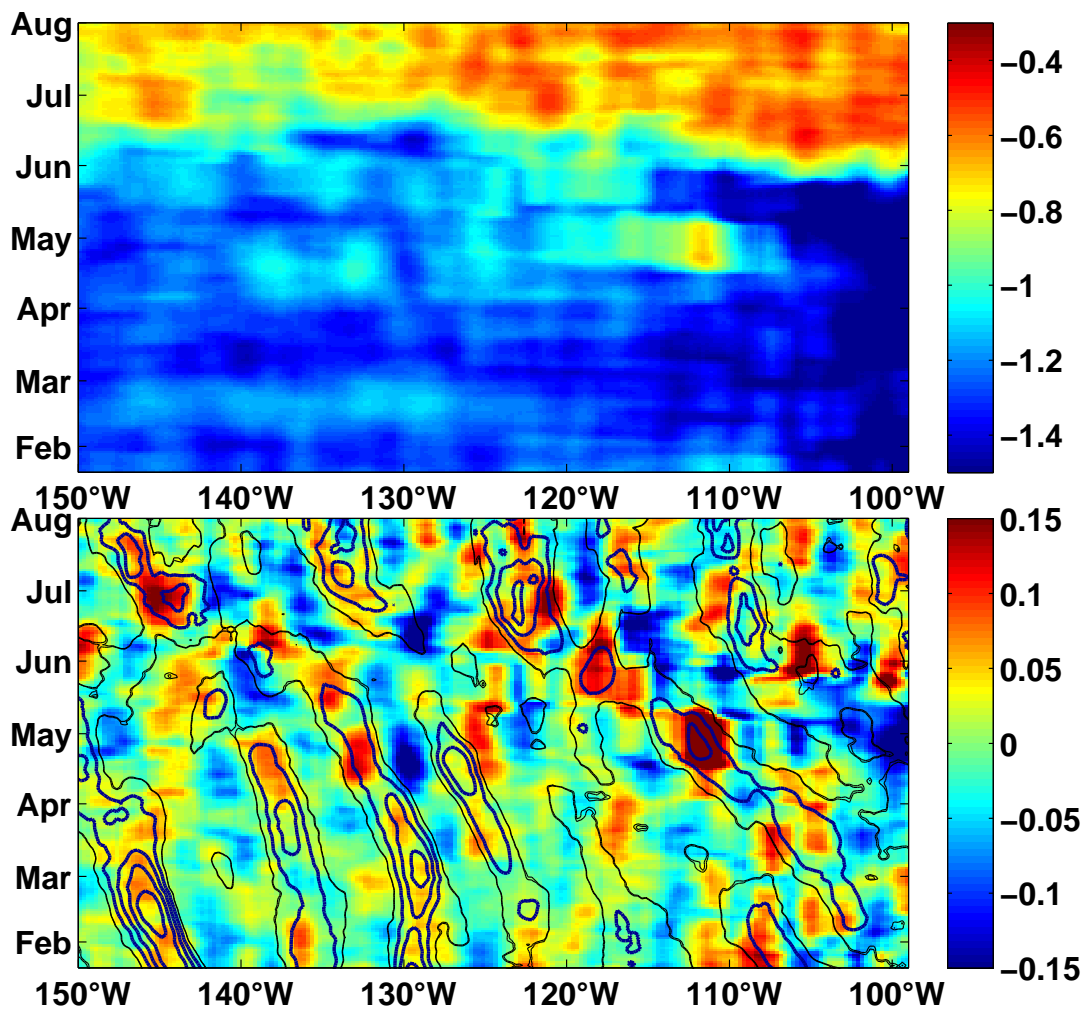
Figure 5-6: Upper panel: Longitude-time diagram of $\log_{10}$ of cloud liquid water (CLW; in mm before taking the logarithm) along $10.125°N$ during 1998. Lower panel: A zonally high-pass filtered version of the field in the upper panel (colored). Contours of positive mesoscale SST anomalies from Figure 5-3 are overlaid at $0.2°C$ intervals, starting from zero.
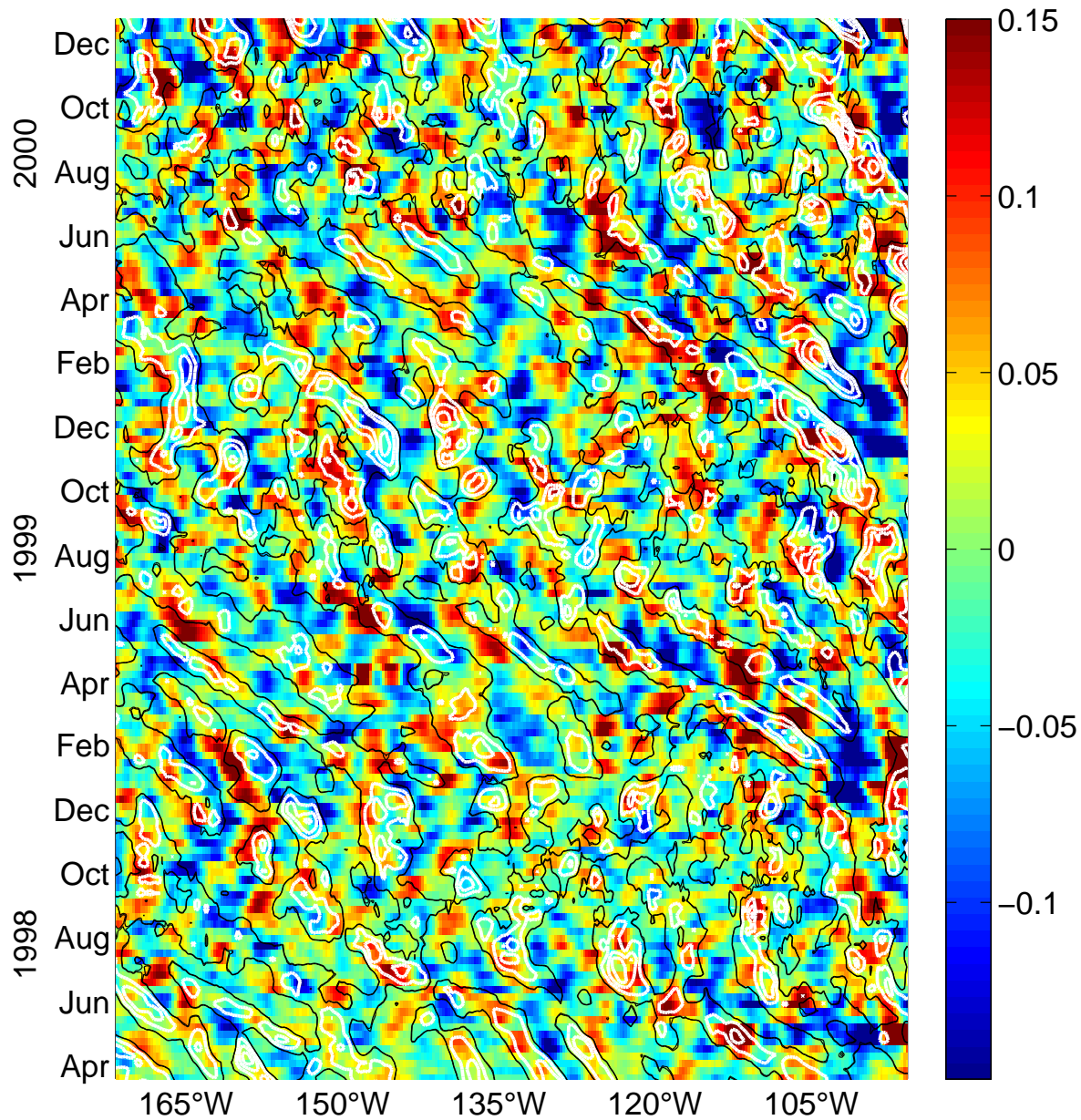
Figure 5-7: Longitude-time diagram of spatially filtered $\log_{10}$ of cloud liquid water (CLW; in mm before taking the logarithm) along $10.125°$N . Positive mesoscale SST anomalies are contoured in white at $0.2°$C intervals, and the zero contour is black. Three-week running averages of weekly data were used for both fields.

of these spectra is smoothed by non-overlapping averaging of adjacent wavenumber and frequency bands. (The band-averaging and taper-window widths are specified below.)

Following Bendat and Piersol (1986), let G_{xy} denote the smoothed estimate of the cross-spectrum and G_{xx} and G_{yy} denote the smoothed autospectra. Then the coherence amplitude is given by,

$$\gamma_{xy} = (\frac{G_{xy}G_{xy}^*}{G_{xx}G_{yy}})^{\frac{1}{2}} \tag{5.2}$$

where the asterisk denotes the complex conjugate. Given the number of degrees of freedom (DOF) for the spectral estimates, the coherence amplitude must exceed

$$\gamma_{1-\alpha} = (1 - \alpha^{\frac{2}{DOF-2}})^{\frac{1}{2}} \tag{5.3}$$

to be considered significant at $100 \times (1 - \alpha)\%$ confidence (e.g, Emery and Thomson, 1998). The coherence phase is

$$\phi = \arctan{(G_{xy})}. \tag{5.4}$$

The transfer function is

$$H_{xy} = |H_{xy}|e^{-i\phi} = \frac{|G_{xy}|}{G_{xx}}e^{-i\phi}, \tag{5.5}$$

where $|H_{xy}|$ is the gain factor. The coherence amplitude is a measure of the extent to which the two quantities covary linearly at each wavenumber and frequency, and the coherence phase expresses the phase of this relationship. For the covarying signal, the gain factor measures the amount of change in one variable that accompanies a unit change in the other variable. For example, if x denotes SST and y denotes surface solar radiation, then the gain factor has units of $W/m^2/°C$ and expresses the coherent change in radiation associated with a 1°C change in SST.

The coherence of SST and surface solar radiation was examined along 10.5°N over the 20 year period of 1984-2003 using the ISCCP radiation product and the Yu et al. (2004) SST product. The longitudinal domain was 129.5°E to 85.5°W, nearly the full width of the Pacific at this latitude. After removal of the time-space mean, the edges of the two-dimensional field were tapered to zero with half of a Hanning window over 1 year and 20° longitude. Spectra were smoothed by computing non-overlapping averages over 17 frequency bands and 3 wavenumber bands, giving the spectral estimates an estimated 102 degrees of freedom.
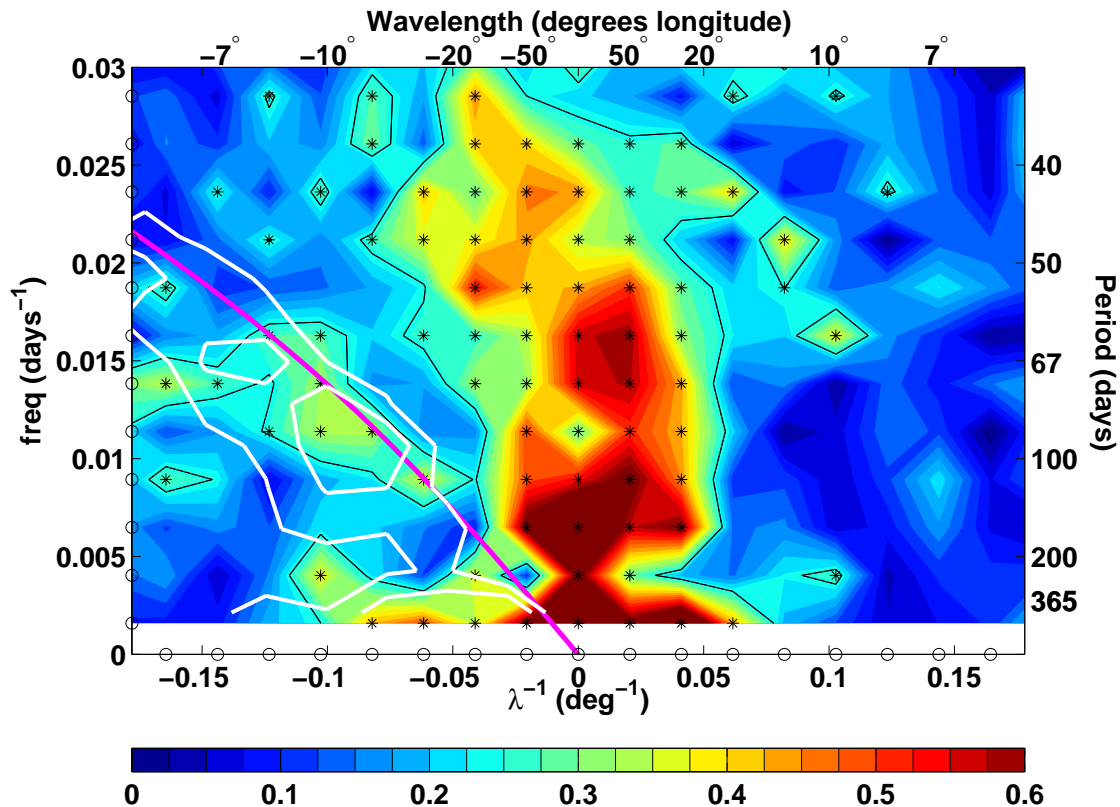
Figure 5-8: Coherence amplitude of surface solar radiation with SST. The black asterisks and black contours mark coherence amplitudes that are significant at 95% confidence. Contours of power spectral density in zonal slope of sea surface height from Figure 4-14 are overlaid in white, and the Rossby wave dispersion curve from Section 4.6 (Equation 4.5 and Figure 4-16) is shown in pink. The highest coherence occurs at low wavenumbers and periods exceeding 50 days, but the coherence is significant within the Rossby wave band defined by the spectral peak in sea surface slope.

SST and surface solar radiation are coherent at a statistically significant level in the intraseasonal Rossby wave band (roughly 60-100 day periods and 8-20° wavelengths; Figure 5-8). The peak coherence amplitude (about 0.33) in this band occurs at wavelengths of 10-16° and periods of 72-88 days and roughly coincides with the peak power spectral density in zonal slope of sea surface height (reproduced in Figure 5-8 from Figure 4-14).

There is also a broad region of higher coherence amplitude (exceeding 0.4) at wavelengths ranging from ±50° to the basin scale and periods greater than 60 days. At a given frequency, atmospheric variability tends to have a much larger spatial scale than oceanic variability[2], so it seems likely that the high coherence at larger scales might be the result of atmospherically-induced (and, at the annual period, astronomically-induced) variations in solar radiation
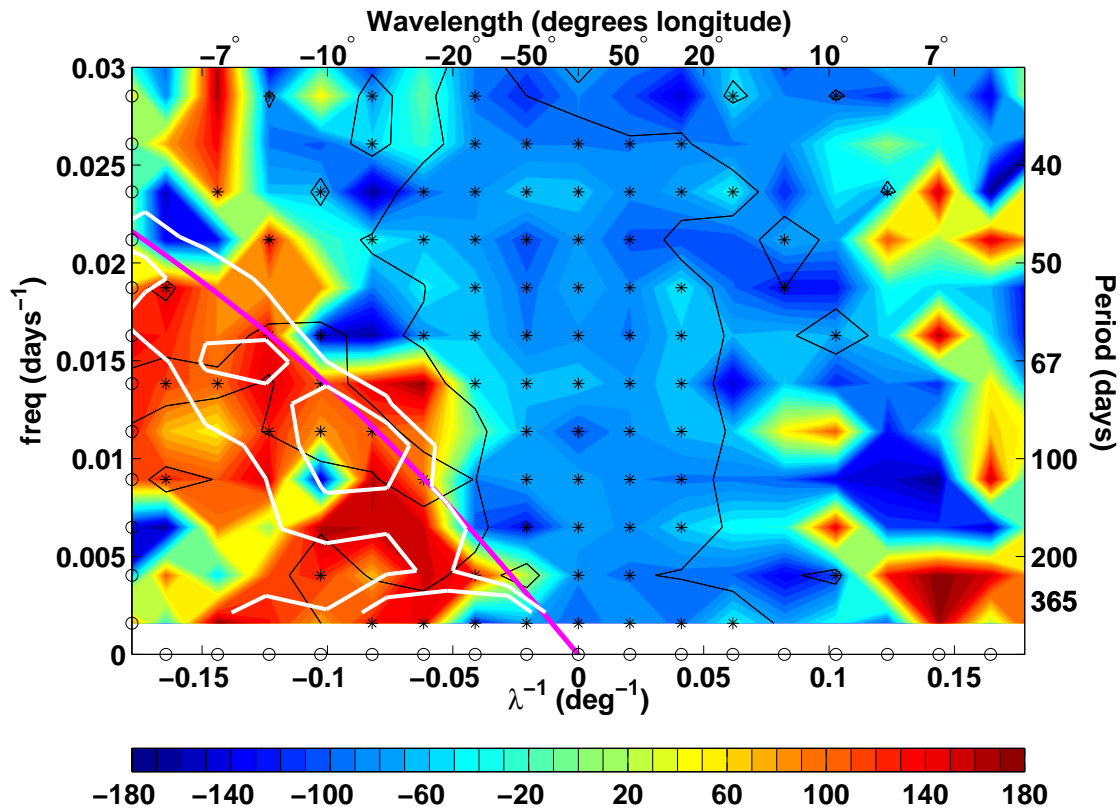
Figure 5-9: Coherence phase between surface solar radiation and SST. As in Figure 5-8, the black asterisks and black contours mark points where the coherence amplitude is significant at 95% confidence; phase estimates are not meaningful at points where the coherence amplitude is not significant. Contours of power spectral density in zonal slope of sea surface height from Figure 4-14 are overlaid in white, and the Rossby wave dispersion curve from Section 4.6 (Equation 4.5 and Figure 4-16) is shown in pink. As described in the text, if the coherence between SST and solar radiation reflects a response of SST to variations in the solar radiation, the phase angle is expected to be -90°. The phase angles in the Rossby wave band are inconsistent with a passive response of SST to variations in solar radiation.

causing large-scale SST variations. Conversely, the tropical atmosphere is not known to support any free dynamical modes in the wavenumber-frequency band corresponding to intraseasonal oceanic Rossby waves, so it seems likely that the coherence there is a result of an atmospheric response to the SST signal induced by oceanic variability. Examination of the coherence phase of SST and solar radiation will allow more quantitative inferences to be made about the cause-effect relationship that gives rise to the observed distribution of coherence amplitude.

---

[2]This can be viewed as being a result of the fact that the atmospheric deformation radius is much larger than the oceanic deformation radius.

Consider a simplified version of the heat equation for the oceanic mixed layer:

$$T_t + vT_y = \frac{Q}{\rho c_p H}, \qquad (5.6)$$

where H is the mixed layer depth and v is the meridional velocity. If meridional advection is negligible and the mixed layer temperature is purely a response to variations in the surface heat flux, then variations in mixed layer temperature should lag variations in surface heat flux by 90°. On the other hand, if the primary influence on SST is meridional advection and variations in Q are merely a result of variations in T, then there is no reason to expect SST to lag Q by 90°.

The coherence phase between SST and surface solar radiation at zonal scales exceeding 50° of longitude is mostly between -70° and -110° (Figure 5-9), indicating that variations in surface solar radiation lead those in SST by a phase close to 90°. This supports the idea that the high coherence of SST and solar radiation at large scales is a result of an SST response to variations in solar heating. (The 95% confidence interval for the phase estimate is less than ±22° for coherence amplitudes exceeding 0.35 and less than ±33° for all coherence amplitudes that are significant at 95% confidence.) In contrast, the phase angle in the Rossby wave band is markedly different (and significantly different in a statistical sense), with phase angles typically between +100° and values close to 180°, indicating that solar radiation ranges from being out of phase with SST to lagging by 80°. Notice that the Rossby wave dispersion curve in Figure 5-9 roughly separates the region where the phase relation is consistent with a passive response of SST to solar radiation from the region where SST variations lead variations in solar radiation[3].

In addition to the coherence amplitude and phase, the gain factor is a useful measure of the relation between SST and solar radiation because it can give additional clues as to the cause-effect relationship. In the Rossby wave band (roughly 60-100 day periods and 8-20° wavelengths), the gain factor is about 5-15 W/m^2/°C at points where the coherence amplitude is significant (not shown). (The range expresses the approximate 95% confidence interval given by Bendat and Piersol (1986, p. 255 and 314); at each of those points, the estimated gain was within 1 W/m^2/°C of 7 W/m^2/°C.) This is of comparable magnitude to,

---

[3]This dispersion curve also separates the region of wavenumber-frequency space where oceanic low-frequency, baroclinic motions are dynamically allowed from the region where they are not expected to exist (e.g., Section 4.6).

but smaller than, what might be expected from inspection of the the buoy data (perhaps 20 W/m²/°C). However, the gain factor estimated by the cross-spectral technique represents an average response over 20 years and the width of the basin. If there is significant spatial or temporal variation in the response amplitude or phase (e.g., there is a relation, but the response is spatially phase-shifted in different ways depending on variable factors like wind speed and direction), then the average gain factor is likely to be substantially lower than it might be in any individual case.

At larger zonal scales ranging from ±50° to the basin scale, the gain factor is substantially larger, having estimated values ranging from 25-70 W/m²/°C at periods less than 150 days (Figure 5-10). The gain factor can be used to provide an additional test of the idea that the coherence of SST and solar radiation at large zonal scales is a result of atmospheric forcing of SST by extending the argument used for interpretation of the coherence phase. If SST variations at these scales were solely the result of variations in insolation, then the mixed-layer heat equation would be,

$$T_t = \frac{Q_{solar}}{\rho c_p H}. \tag{5.7}$$

Computing the Fourier transform of this equation (and assuming ρ, c_p, and H are constant in time), the gain factor would be expected to be $|H_{xy}| = \omega \rho c_p H$. Taking $H = 75$ m to be a representative value of mixed-layer depth (and $\rho c_p = 1024 \times 4000$ Jm^{-3}/°C), this theoretical estimate of the gain factor is of comparable magnitude to the observed gain factor at large zonal scales (Figure 5-10). Although the theoretical estimate of the gain factor is within error bars (at 95% confidence) of the observed estimate, the error bars are large, and any constant value of the gain factor between 20 and 45 W/m²/°C would also be consistent with the observations. Note that the expected gain factor for a purely forced SST response for variability at 50-100 day periods is 35-70 W/m²/°C and is inconsistent with the gain factor observed in the oceanic Rossby wave band. Thus, the gain factor and phase are consistent with the interpretation of the high coherence amplitude at large zonal scales as an oceanic response to variations in solar radiation, but the gain and phase in the Rossby wave band are not consistent with this interpretation.

The ISCCP solar radiation product has a resolution of about 280 km, which is marginally adequate for examining variations at the oceanic mesoscale. Given this limitation, it is
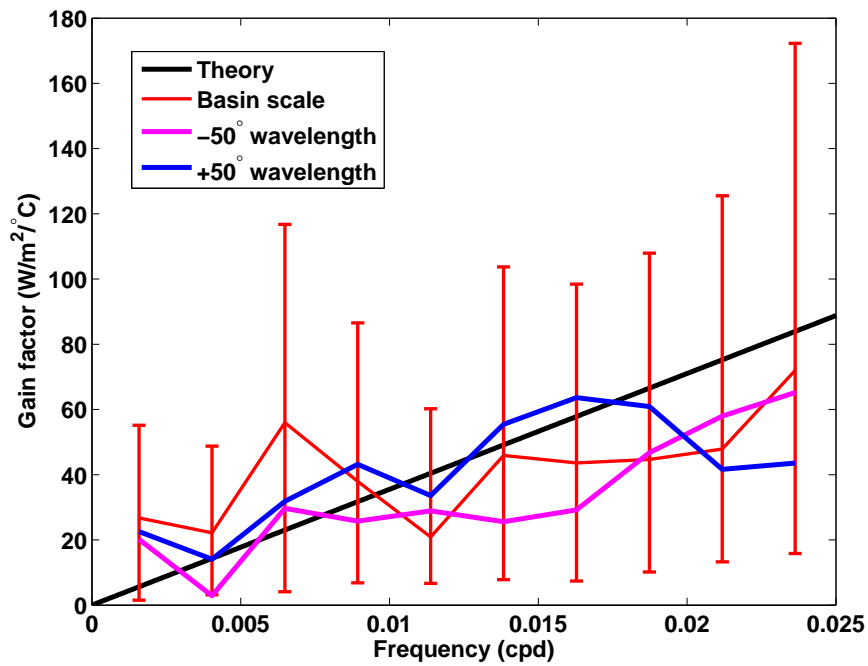
Figure 5-10: Comparison of the observed gain estimate for SST and solar radiation at large zonal scales to the theoretical estimate derived under the assumption that SST responds passively to large-scale, atmospherically-induced variations in the surface solar radiation (Equation 5.7). The theoretical estimate is evaluated for a mixed-layer depth of 75 m. For clarity, 95% confidence limits are shown only for the smallest wavenumber band; the error bars are similarly large for the other curves. While the gain factor and coherence phase are consistent with a passive oceanic response at large scales, the error bars are large enough that a more complex relationship between SST and surface solar radiation might exist.
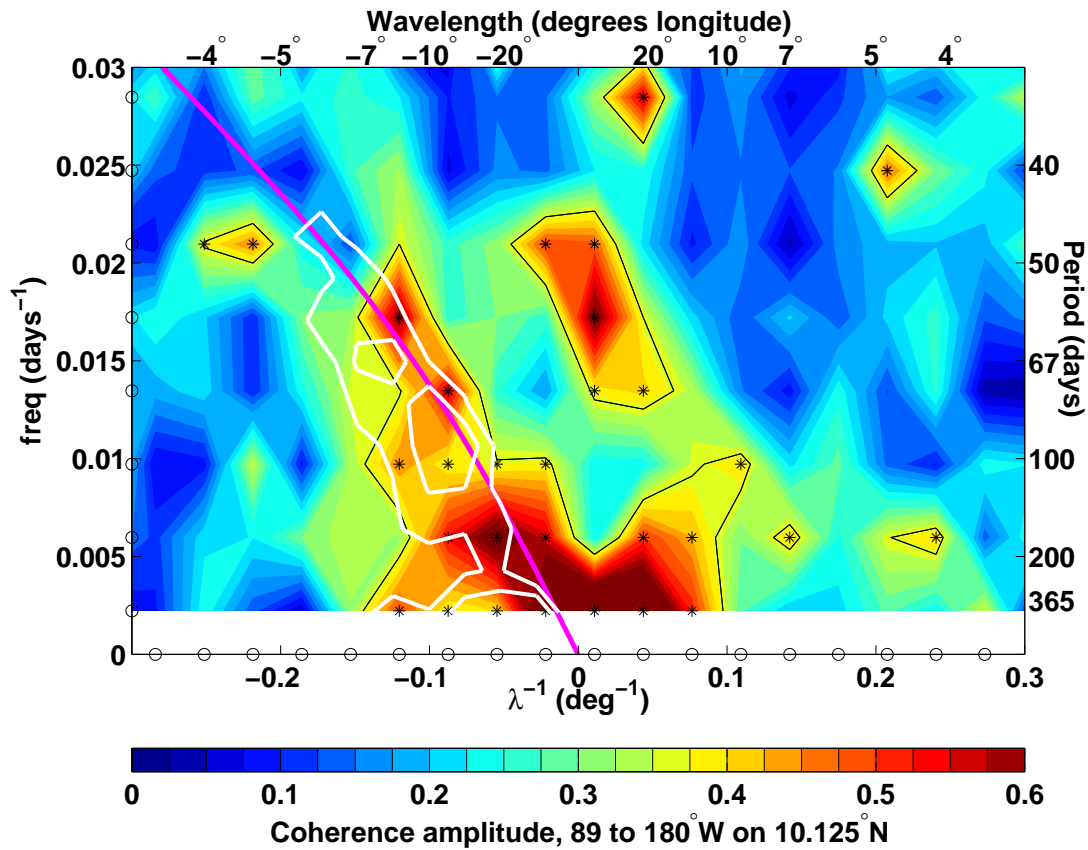
Figure 5-11: Coherence amplitude of $\log_{10}(\text{CLW})$ with SST (TMI). The black asterisks and black contours mark coherence amplitudes that are significant at 99% confidence. Contours of power spectral density in zonal slope of sea surface height from Figure 4-14 are overlaid in white, and the Rossby wave dispersion curve from Section 4.6 (Equation 4.5 and Figure 4-16) is shown in pink. SST and $\log_{10}(\text{CLW})$ are statistically significant in the oceanic Rossby wave band.

perhaps surprising that a relationship between SST and ISCCP solar radiation was detected in the mesoscale band. To reinforce the cross-spectral results for the relation of SST and solar radiation, and to ensure that the relationship between SST and cloud properties is investigated using data that adequately resolves the oceanic mesoscale, the relationship of SST and CLW was investigated using data from the TRMM and SSM/I satellites, which are available on a 0.25° spatial grid.

The relationship of SST and CLW on 10.125°N was examined over a domain spanning 89-180°W and 1998-2005. Inspection of filtered longitude-time plots (such as Figure 5-6) suggested that the relationship of SST to the logarithm of CLW is more nearly linear than the relation of SST to CLW, so the coherence between SST and the logarithm of CLW was examined. (The cross-spectral technique used here detects only linear relationships.

Cross-spectral results for linear variations of CLW with SST are similar and are presented in an appendix.) As in the computations using solar radiation, the edges of each time-space series were tapered to zero over 1 yr and 20° longitude using half-Hanning windows. Non-overlapping band-averaging of the spectra was carried out over 3 wavenumber bands and 11 frequency bands, giving a total of 66 degrees of freedom for the spectral estimates.

Consistent with expectations from the filtered longitude-time fields, log(CLW) is coherent with SST at wavenumbers and frequencies in the oceanic Rossby wave band (Figure 5-11). Coherence amplitudes at wavelengths of 7-18° and periods of 50-100 days are 0.37-0.6 (statistically significant at 99% confidence), indicating that 10-35% of the variance in log(CLW) at these wavenumbers and frequencies can be accounted for by SST variations. In the Rossby wave band, the region of wavenumber-frequency space where SST and log(CLW) are coherent is nearly the same region as where the variance of the zonal slope of sea surface height (a proxy for meridional velocity) is largest (Ch. 4 and Figure 5-11), which corroborates the notion that meridional advection causes SST fluctuations that induce variations in CLW.

The coherence of SST and log(CLW) is also high (exceeding 0.6) at larger zonal scales (Figure 5-11), particularly in the period band of 43-86 days days and in the lowest frequency band (periods exceeding 244 days). The peak coherence in the intraseasonal period band occurs in the 52-65 day period band with a wavenumber indistinguishable from zero (but encompassing eastward wavelengths as small as 36° longitude). This variability may be associated with the Madden-Julian oscillation (MJO), an eastward propagating tropical atmospheric wave of global zonal scale and periods of 30-90 days (e.g., Madden and Julian, 1994).

The coherence phase between $\log_{10}$(CLW) and SST is similar to that between solar radiation and SST, except the sign differs by 180°, as expected, since higher cloud liquid water should typically be associated with reduced insolation. Of the points in the Rossby wave band where SST and $\log_{10}$(CLW) are significant at 99% confidence, only two points have phase angles more negative than -40° (Figure 5-11). (95% confidence limits for these points are no larger than ±25°.) Excluding the one point at 58 days, 8° wavelength, the phase angles in the Rossby wave band indicate that the maximum CLW is shifted 1-2° of longitude westward of the maximum SST.

As was the case for solar radiation, the coherence phase for the large-scale intraseasonal variability in $\log_{10}$(CLW) is consistent with an SST response to atmospheric variability. In

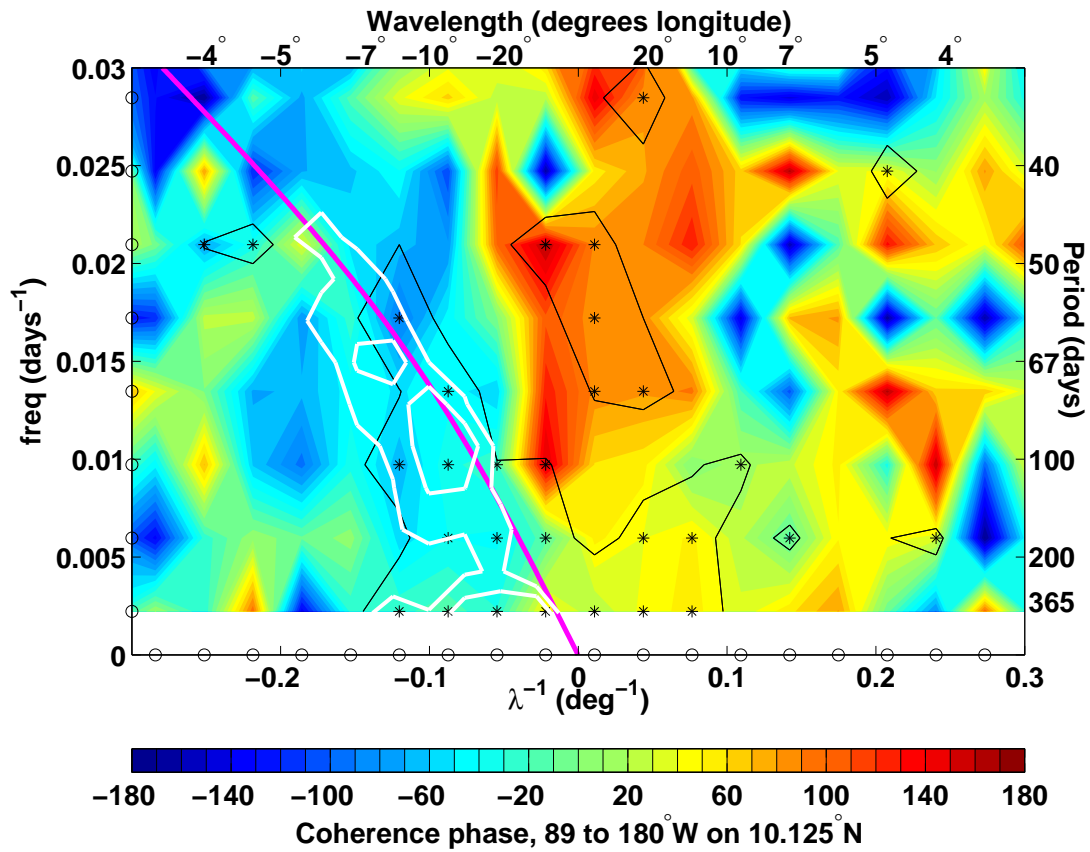Figure 5-12: Coherence phase between $\log_{10}(\text{CLW})$ and SST (TMI). The black asterisks and black contours mark points where the coherence amplitude is significant at 99% confidence. Contours of power spectral density in zonal slope of sea surface height from Figure 4-14 are overlaid in white, and the Rossby wave dispersion curve from Section 4.6 (Equation 4.5 and Figure 4-16) is shown in pink.

the wavelength band representing the largest zonal scales (centered at an eastward wavelength of about 90° longitude), the estimated coherence phase angle is between 90° and 100° in the three intraseasonal period bands that are significant at 99% confidence. This indicates that the rate of decrease (increase) of SST is largest when CLW is at a maximum (minimum). This suggests that the high coherence of SST and $\log_{10}(CLW)$ reflects an SST response to variations in clouds by the MJO, consistent with recent results focusing on the SST response to the MJO in the eastern Pacific (Maloney and Kiehl, 2002).

5.6 Discussion

A variety of data sets show coherent variability between SST variations in the oceanic Rossby wave band and properties related to convection along 10°N in the eastern tropical Pacific. In the time-space domain, a relationship is apparent between the filtered SST field and the filtered cloud reflectivity and CLW fields. In the spectral domain, and without filtering, SST is coherent with surface solar radiation and the logarithm of CLW in the Rossby wave band. Each of the data sets has limitations, but the consistent results drawn from analysis of various independent data sets indicates that this relation is real, not a spurious result of sampling or measurement errors in any particular data set.

Interpretation of the relation between SST and convection

When inspecting high resolution satellite data, such as GOES infrared measurements, the most obvious characteristic of atmospheric convection is the presence of a variety of synoptic features, with atmospheric dynamics at timescales of days to weeks modulating the occurrence of short-lived convective events that last for hours. For example, over the western equatorial Pacific Ocean, the Madden-Julian Oscillation (MJO) modulates convection by creating conditions that are alternately favorable and unfavorable for convection (Chen et al., 1996). During the convectively active phase of the MJO, convection occurs in small embedded regions of frequent convection that propagate westward and have a period of about two days and a zonal scale on the order of a few degrees of longitude. These two-day disturbances are believed to be inertia-gravity waves, and embedded within them are even smaller "cloud clusters" that have their own distinct propagation characteristics and timescales of hours (Chen et al., 1996).

132
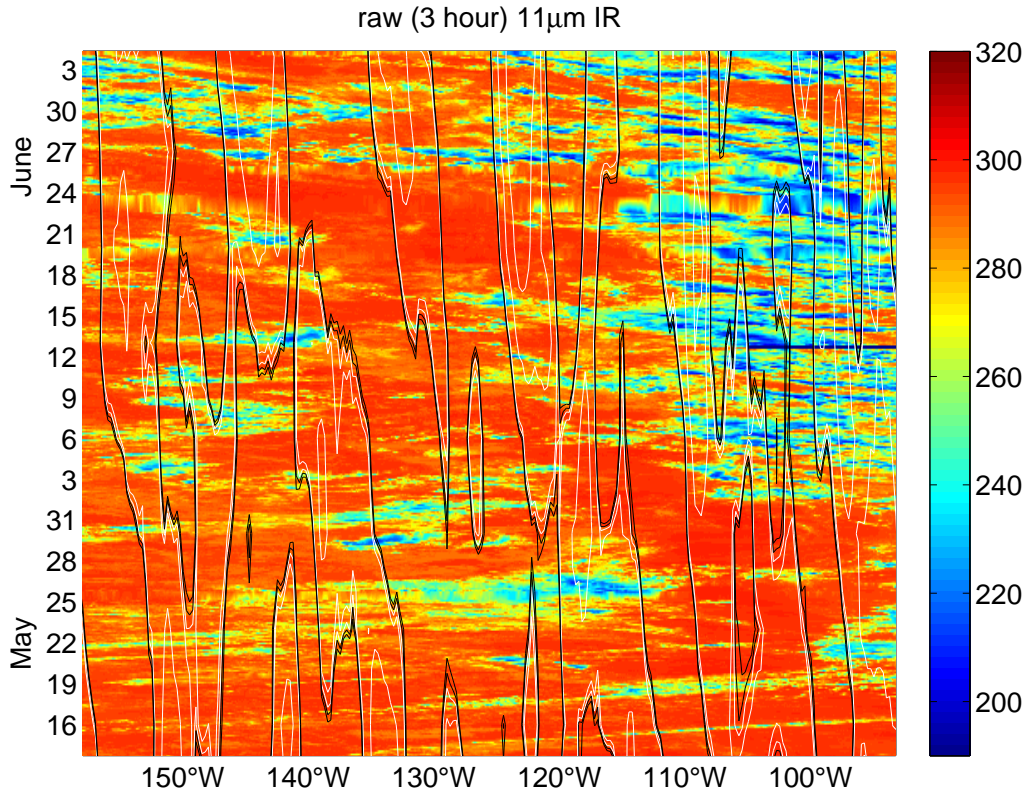
Figure 5-13: Infrared brightness temperature during parts of May and June 1998 from the GOES-9 satellite (colors; K). Very cold cloud-top temperatures (e.g., <220 K) are a reliable indication of deep convection. Warm mesoscale SST anomalies are contoured in white, and the zero contour is black. Four data gaps of about one day duration have been interpolated in time, and a small gap east of 110°W near June 13 remains.

The short-lived nature of clouds and the complex, multi-scale interactions that modulate their occurrence can be illustrated with high-resolution satellite measurements, such as GOES infrared measurements of cloud-top temperature, which give an indication of the depth of convection. Signals from many types of atmospheric tropical dynamical signals (easterly waves, MJO, Kelvin waves, Rossby waves, gravity waves, and mixed Rossby-gravity waves) have been observed in cloud-top temperature (e.g., Wheeler and Kiladis, 1999). Figure 5-13 shows about 1.5 months of cloud-top temperature at three-hour intervals from the GOES-9 satellite (11 μm infrared channel), in which the influence of myriad dynamical processes is apparent. Disturbances are seen to travel both eastward and westward with a range of timescales. Note that all of the atmospheric disturbances travel much faster than the mesoscale SST signals and that the cloud signals at periods longer than a few weeks studied here represent an average over a number of convective events.

133

While inspection of the filtered fields (Figures 5-5b and 5-6) gives the impression of atmospheric fields co-propagating with intraseasonal-timescale mesoscale SST anomalies, the coherence of cloud properties with mesoscale SST anomalies is probably best interpreted as a tendency of the SST field to modulate the likelihood and intensity of convection embedded within synoptic atmospheric disturbances. Clouds do not persist for weeks, but instead have lifetimes of hours. Thus, the relationship of SST and cloud properties at intraseasonal periods should not be interpreted as clouds that co-propagate with the SST anomalies, but rather as a tendency for warm mesoscale SST variations to contribute to conditions favoring convection.

Shallow vs. deep convection on 10°N in the eastern Pacific

The annual meridional migration of the ITCZ leads to local variations in convective regimes on 10°N in the eastern tropical Pacific. As measured by monthly climatological surface wind convergence (e.g., from the ERS-2 scatterometer), the ITCZ is farthest south during February-May (not shown)[4]. During this time, the northeasterly trades are strong at 10°N, and the clouds are, nominally, non-precipitating trade cumuli (e.g., Betts and Ridgeway, 1989). During about August to November, the ITCZ is farthest north (spanning roughly 9-13°N) and there is frequent deep convection and heavy precipitation. During the transitional phases (December/January and June), the central latitude of the ITCZ is south of 10°N, but there is still frequent deep convection, precipitation, and mean convergence. This annual meridional migration of the ITCZ is clearly reflected in the precipitation along 10°N (not shown) from the TMI and SSM/I microwave instruments (averaged and processed analogously to the CLW fields as described in Section 5.2), and there is some indication of a relationship between SST and precipitation (not shown) that is similar to the one shown here between SST and CLW[5].

Shallow clouds have important consequences for local and global radiation budgets, but

---

[4]There is some longitudinal variation in the latitude-time position of the ITCZ in the eastern Pacific. These statements about the climatological position of the ITCZ are based on the latitude-time evolution of the climatological ITCZ on 125°W.

[5]The linear relationship of precipitation and SST is qualitatively similar to that shown in Figure 5-15 in the appendix but is statistically significant at 95% confidence at only two points in the mesoscale band, both points being near periods of 75 days and wavelengths of 10° longitude. The coherence of the logarithm of precipitation to SST is quantitatively almost identical to the relationship between the logarithm of CLW and SST depicted in Figure 5-11, but this relationship is not dwelt on here because examination of the logarithm of precipitation requires substitution of small nonzero values of precipitation when the precipitation is zero.

precipitating deep convection plays a more direct role in driving the general circulation of the atmosphere (because latent heat is irreversibly released in the process of precipitation). The quantitative results of the spectral analysis in Section 5.5 represent the relationship between mesoscale SST variability and (the log of) CLW in the longitude-time average only and do not allow direct insight into the extent to which mesoscale SST variations influence deep convection in the ITCZ. The linear relation of SST to CLW (Appendix A) is expected to be dominated by the deep convective regime because the variance of CLW in the mesoscale band is much larger (i.e., on the order of 20 times larger; Figure 5-14) during the local ITCZ season. (This is as opposed to the logarithm of CLW, which has a relatively reduced seasonal variation in mesoscale-band variance.) This result, along with the results from the time-longitude domain (e.g., Figures 5-6 and 5-7), suggests that deep convection in the ITCZ is modulated by the mesoscale SST variability.

Given the mix of shallow and deep convection that occurs along 10°N in the eastern tropical Pacific, it seems likely that explanation of the relationship between mesoscale SST variations and CLW would require more than one model (e.g., trade-cumuli and deep convection models). However, convection is generally expected to be influenced by the local surface heat and moisture fluxes (and modulation of surface fluxes is ultimately the only way that SST variations can exert influence on the atmosphere). During the trade-wind season along 10°N (roughly February-May), the coherent signal in SST and CLW might be understood using a model of non-precipitating trade-cumulus convection that includes an explicit dependence on SST (e.g., Betts and Ridgway, 1989; Emanuel, 1994). For such shallow, boundary-layer convection, a large relative variation in CLW can result from a modest variation in the thickness of the shallow cloud layer (e.g., O'Neill et al., 2005). For precipitating convection, the dependence on local surface fluxes (or SST) is expected based on the "weak temperature gradient approximation" (e.g., Sobel and Bretherton, 2000; Bretherton and Sobel, 2002; Sobel and Gildor, 2003), which is likely to be valid on the time and space scales of oceanic mesoscale variability. While the weak temperature gradient approximation (e.g., as implemented in Sobel and Gildor, 2003) suggests a direct influence on deep convection by oceanic mesoscale variations in the local surface fluxes of heat and moisture, horizontal advection within the atmospheric boundary layer and troposphere would be expected to generally reduce the local coherence of SST and measures of deep convection.

Relation to previous work

In a 37-day field study of convection in the eastern Pacific near 10°N, 95°W during September and October, Raymond et al. (2003) found the surface entropy flux (closely related to surface heat flux) to be the most important factor influencing deep convection, while horizontal advection was the least important. Adiabatic vertical motions and surface fluxes accounted for about two thirds of the variance in cloud-top temperature in the study region. The study region of Raymond et al. (2003) was part of the domain studied here, but it is not obvious that conclusions of the 37 day study during a deep convective regime can be applied directly to the multi-year data set considered here, with its range of ITCZ and trade-wind conditions. In addition, the timescale of the convection signals studied here is not resolved in the 37-day study. Still, the results of Raymond et al. (2003) may be relevant to the relationship between mesoscale SST variability and convection seen here. If so, those results suggest that the idealized model of the previous subsection contains the most important convective forcing mechanism (i.e., surface fluxes) but is missing essential physical processes (i.e., horizontal advection and adiabatic vertical motions). For example, the Raymond et al. (2003) results indicate that about one third of the variance in cloud-top temperature can be ascribed to horizontal advection.

O'Neill et al. (2005) detected a relationship between meanders in the SST front near the Agulhas Return Current and CLW that is in some ways similar to the one found here. They considered the possibility that variations in the surface wind divergence induced by the SST field's effect on boundary layer stability and/or boundary layer pressure gradients (as described in the introduction to this chapter) modulated the propensity for convection. However, they found variations in wind-stress divergence were actually uncorrelated with variations in CLW and inferred that the CLW signal must result from the surface fluxes rather than from the wind divergence.

Signals in visible reflectivity and CLW have been detected in association with SST variations caused by tropical instability waves (Deser et al. 1993; Hashizume et al., 2001). In the tropical instability wave region, these signals are associated with shallow, boundary layer convection (Xie et al., 1998; Hashizume et al., 2002). However, Hashizume et al. (2001) found indications that the tropical instability waves induce a remote response in deep convection (i.e., precipitation) within the ITCZ, several hundred kilometers to the north,

consistent with earlier results from numerical simulations (Xie et al., 1998). Hashizume et al. (2001) suggest that this remote influence on ITCZ convection may be caused by the boundary-layer wind convergence associated with the tropical instability waves, but it might also be due to modulation of the temperature and moisture of the boundary-layer air as it flows past the instability waves and into the ITCZ. In any case, such nonlocal influence of mesoscale SST variations on convection in the ITCZ would not be detected in the present analysis and would degrade the coherence between coincident SST and convection signals.

In this study, CLW variations in the Rossby wave band were found to be shifted, on average, 1-2° of longitude in the downwind direction (westward) of warm SST anomalies. A phase shift between SST and cloud has also been noted in previous studies that have detected a relationship between mesoscale SST variations and cloud properties (Deser et al., 1993; O'Neill et al., 2005; Hashizume et al., 2001). The phase shift found here is comparable with the findings of Deser et al. (1993) and O'Neill et al. (2005) of downwind phase shifts of about 1.25° and 0.5°, respectively. (In contrast, by regressing the CLW field against SST at one point in the tropical instability wave region, Hashizume et al. (2001) found an upwind zonal phase shift. This result may be regarded as suspicious since the inferred phase shift appears to vary with distance from the chosen regression point.) In studies of oceanic frontal regions, downwind phase shifts of clouds have also been noted (e.g., Wai and Stage, 1989; Raymond et al., 2004).

The observed phase shift between SST and clouds may give further insight into the causal chain connecting SST variations to cloud variations, but there are a host of reasons why the phase relation might vary. Xie (2004) pointed out that boundary layer destabilization by the SST field tends to make cloud be in phase with SST and suggested that the resulting wind speed variations would cause convergence patterns that might shift the convection to the downwind side of warm SST anomalies. A more direct mechanism that might cause a phase shift of clouds and SST variations has to do with horizontal advection and the finite adjustment time of the ABL. In the admittedly oversimplified case where temperature controls the stratification of the ABL and convection controls the exchange of heat at the top of the ABL, the onset of static instability as air moves from cool to warm water would depend on the strength of the stratification at the top of the boundary layer, the speed of the wind and its orientation to the SST gradient, the boundary layer depth, and the magnitude and spatial scale of the mesoscale SST signal. Depending on these factors, convection could

occur either upwind or downwind of the peak mesoscale SST anomaly. In addition, the cloud signal is expected to feed back onto the SST signal (Appendix B), and this could also modify the phase relation.

This study differs from previous studies in that a broadband relationship is detected between mesoscale SST variations and variations in the logarithm of CLW, with a reasonably high coherence amplitude (>0.4) detected at the wavenumbers and frequencies corresponding to the spectral peak in oceanic meridional velocity (i.e., zonal slope of sea surface height). Perhaps more importantly, part of the coherent signal reflects an influence of mesoscale SST variability on variability of deep convection in the ITCZ, which is located over $10°$N for about six months of each year. Since 15% or more of the variance in the logarithm of CLW at the periods and wavelengths of oceanic mesoscale variability (here, on the order of 70 days and $10°$ longitude) is related to the mesoscale SST field, it is likely that adequate resolution of the mesoscale SST field would improve the fidelity of convection in atmospheric numerical models. This has already been shown to be the case for simulation of the surface wind field (Maloney and Chelton, 2006). Remote influence of the mesoscale SST field on convection in the ITCZ (Xie et al., 1998; Hashizume et al., 2001) means that adequate resolution of the SST field in numerical simulations may lead to a larger improvement than the local relationship detected in this study would suggest.

Appendix A: Linear variations of SST and CLW

The strong annual cycle in CLW on $10°$N leads to a marked annual variation in the variability of CLW at zonal scales smaller than $10°$ longitude (e.g., Figure 5-14). Like $\log_{10}(\text{CLW})$ and SST, the filtered CLW and SST fields depicted in Figure 5-14 are correlated at a statistically significant level ($r=0.26$), but it is clear that the anomaly in CLW associated with a given anomaly in SST is more variable than the anomaly in $\log_{10}(\text{CLW})$ (Figure 5-6). Thus, the coherence amplitude between SST and CLW is expected to be lower than that between SST and $\log_{10}(\text{CLW})$. While this proves to be the case (Figure 5-15), SST and CLW are still coherent in the Rossby wave band at a statistically significant level. Because the signal in filtered CLW is much larger during the summer when the ITCZ is near $10°$N, it is expected that the coherence amplitude and phase are dominated by the summer season. The estimate of the coherence phase between SST and CLW (Figure 5-16) is essentially the same as for

SST and $\log_{10}(\text{CLW})$, which is expected to some extent since the phase of $\log_{10}(\text{CLW})$ should be the same as that of CLW, in the sense that an increase in CLW implies an increase in $\log_{10}(\text{CLW})$.

Appendix B: Potential implications for the ocean

Several investigators have noted that the nearly out-of-phase relationship between SST and solar radiation, along with the variations in surface sensible and latent heat flux that are ultimately responsible for those variations, should be expected to damp the mesoscale SST anomalies (Deser et al., 1993; Thum et al., 2002; Xie, 2004). However, there is another potential effect of this tendency for surface heat flux variations to damp mesoscale SST anomalies. This effect involves the competition of the oscillatory advection and damping in setting the phase of the SST anomaly with respect to the oscillatory velocity signal and can lead to a down-gradient eddy heat flux. Consider a simplified model of temperature fluctuations in the oceanic mixed layer associated with oscillatory advection and damping of SST by the surface heat flux:

$$T'_t + v\bar{T}_y = -\sigma T', \tag{5.8}$$

where T' is the temperature signal driven by the oscillatory velocity signal v, $\bar{T}_y$ is the meridional temperature gradient (assumed constant), and σ is an inverse damping timescale for the SST anomalies ($-\sigma T' = Q/(\rho c_p H)$) and is also taken to be constant. (This is the same equation used by Small et al. (2005), except that vertical mixing at the base of the mixed layer is ignored here.) Seeking an oscillatory solution with frequency ω, we find

$$T' = Re(\frac{-v_o\bar{T}_y e^{i\omega t}}{i\omega + \sigma}) = \frac{-v_o\bar{T}_y[\sigma cos(\omega t) + \omega sin(\omega t)]}{\sigma^2 + \omega^2}. \tag{5.9}$$

When $\sigma = 0$ (no damping), T' is in perfect quadrature with v (which is proportional to $cos(\omega t)$). However, when $\sigma \neq 0$, T' and v are no longer in quadrature; the presence of the surface heat flux feedback modifies the phase relationship between T' and v.

The vertically integrated meridional eddy heat flux in this idealized scenario is

$$\rho c_p H \overline{v'T'} = \frac{-\rho c_p H v_o^2 \sigma \bar{T}_y}{2(\sigma^2 + \omega^2)}. \tag{5.10}$$
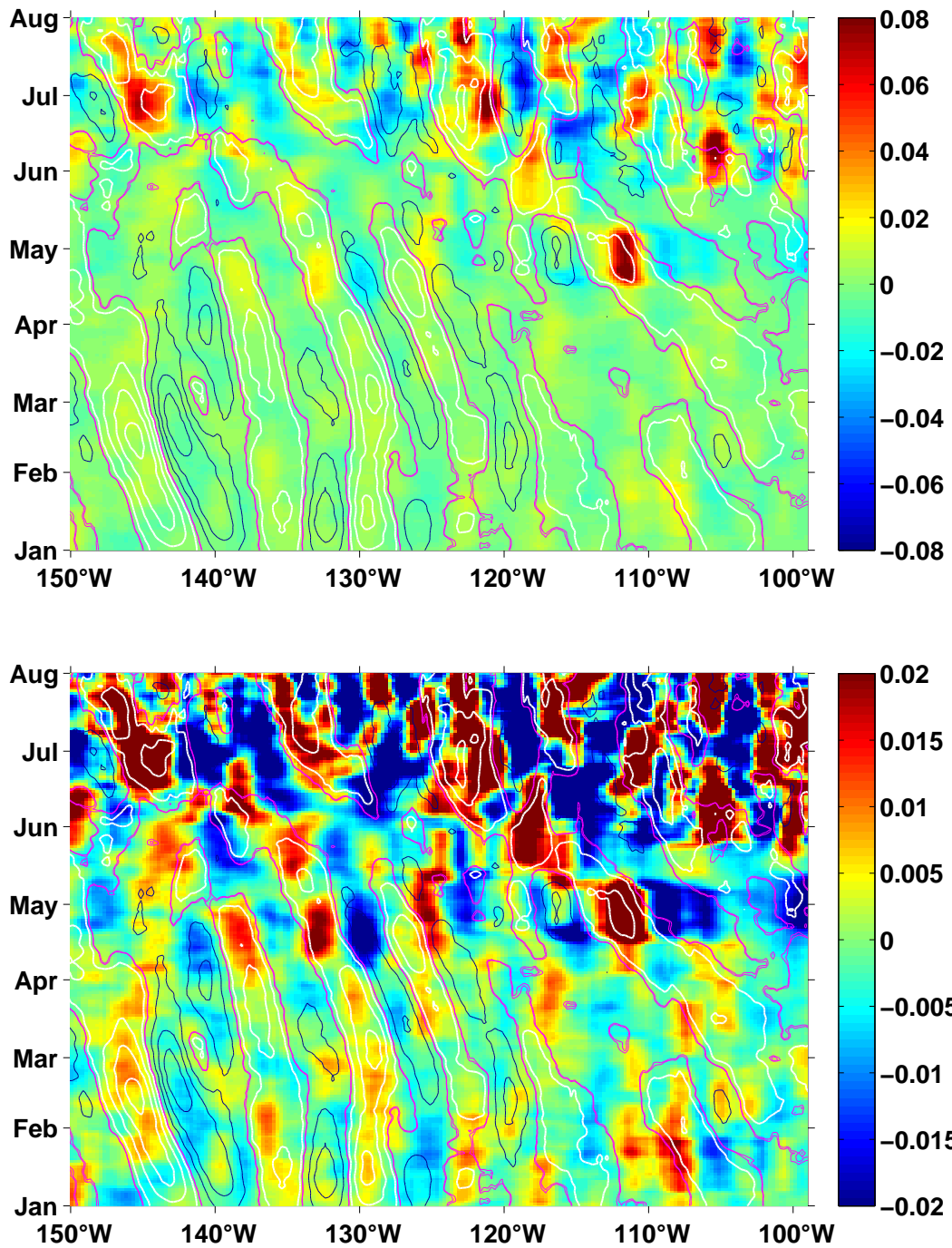
Figure 5-14: Both panels show filtered CLW (mm; colored) and filtered SST (white contours for warm anomalies, black contours for cool anomalies) along 10.125°N during 1998. The difference between the two panels is in the color scale. Note that CLW anomalies are about 10 times larger during the ITCZ season (June onward) than during the trade wind season (before April).
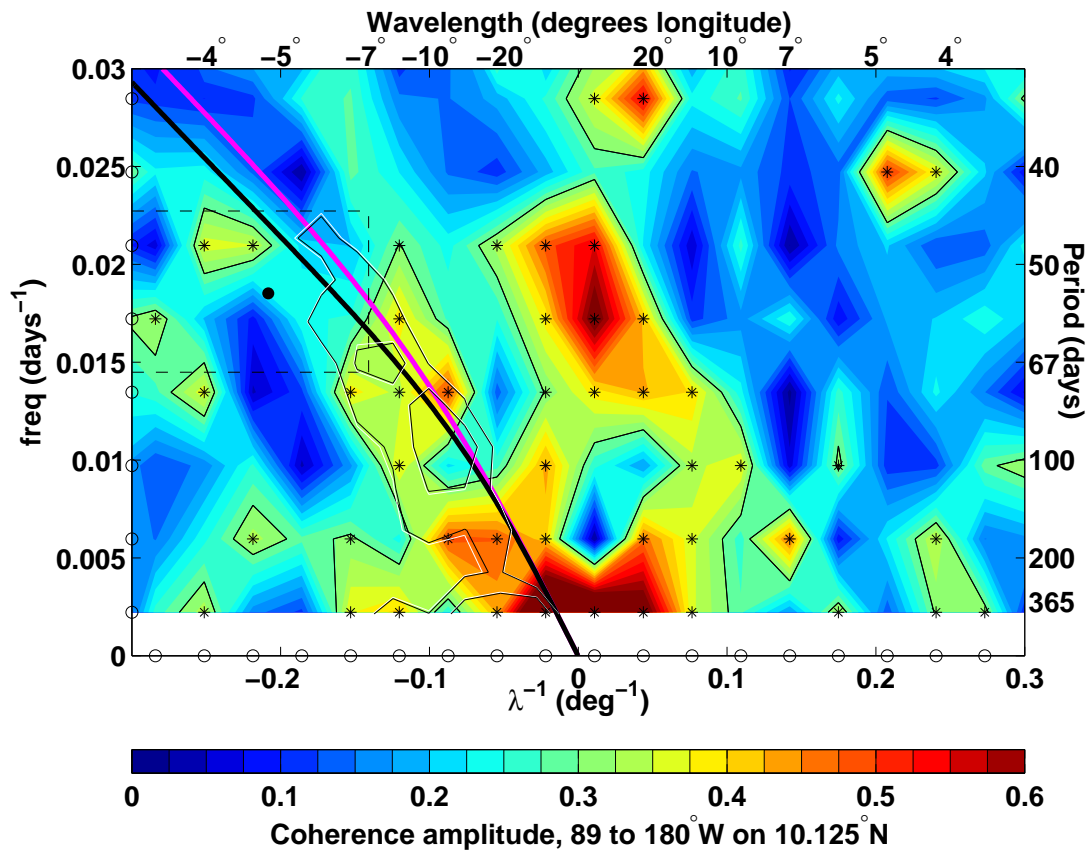
Figure 5-15: Coherence amplitude of CLW with SST (TMI). The black asterisks and black contours mark coherence amplitudes that are significant at 95% confidence. Contours of power spectral density in zonal slope of sea surface height from Figure 4-14 are overlaid in white, and the Rossby wave dispersion curve from Section 4.6 (Equation 4.5 and Figure 4-16) is shown in pink.

Figure 5-16: Coherence phase between CLW and SST (TMI). The black asterisks and black contours mark points where the coherence amplitude is significant at 95% confidence. Contours of power spectral density in zonal slope of sea surface height from Figure 4-14 are overlaid in white, and the Rossby wave dispersion curve from Section 4.6 (Equation 4.5 and Figure 4-16) is shown in pink.

Since the horizontal heat flux is proportional to $-T_y$, this is a down-gradient heat flux. The diffusivity associated with this down gradient heat flux is
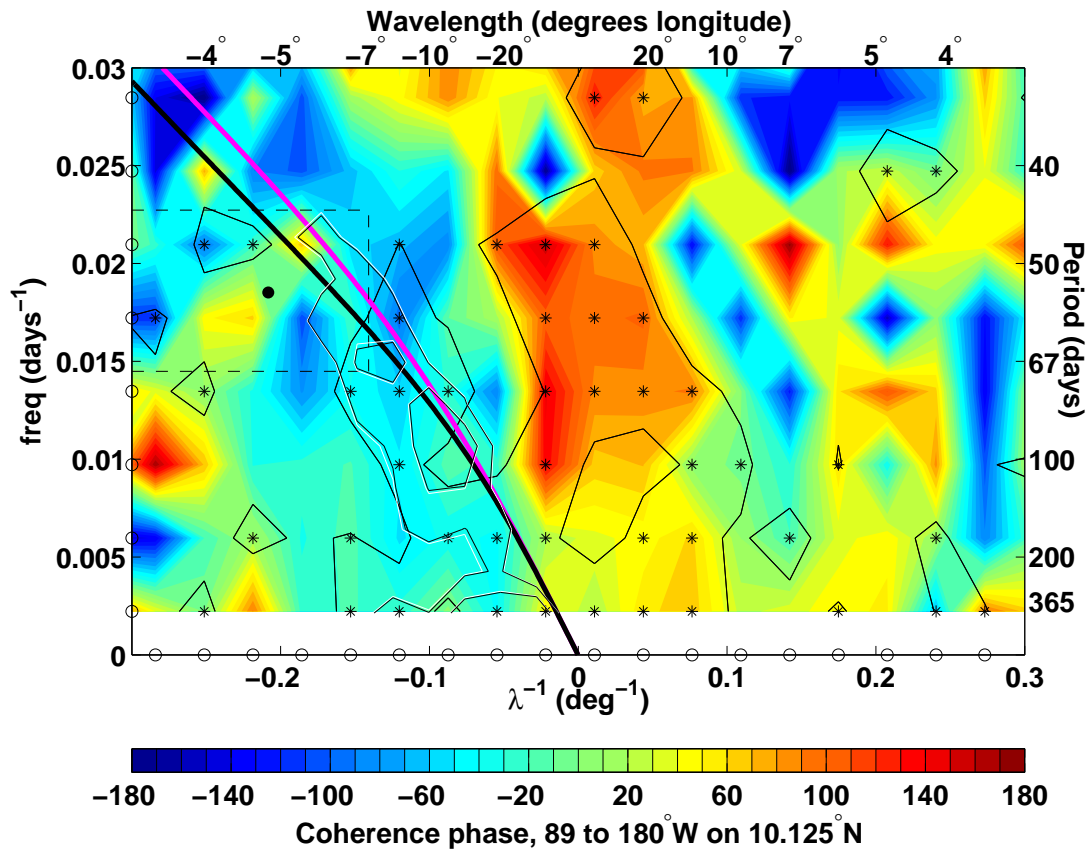
$$\kappa = \frac{-\overline{v'T'}}{T_y} = \frac{v_o^2 \sigma}{2(\sigma^2 + \omega^2)}. \tag{5.11}$$

This eddy diffusivity depends on the damping timescale and the frequency and kinetic energy of the velocity fluctuations. Assuming an inverse damping timescale of 120 days, an oscillatory velocity signal with an amplitude of 15 cm/s and a period of 60 days would lead to a horizontal diffusivity of about 740 $\mathrm{m}^2\mathrm{s}^{-1}$, a value that is certainly large enough to be non-negligible in the mean heat balance of the eastern Pacific warm pool or other regions with strong temperature gradients. Although the PACS mooring record is too short to make a meaningful estimate of the eddy heat flux in the Rossby wave band, the relation between surface heating, horizontal advection, and the rate of change of mixed-layer temperature (Figure 3-11) is consistent with the basic premise of Equations 5.8 and 5.9, that the phase of the temperature signal is determined by a competition between horizontal advection and a covarying surface heat flux signal.

The observations presented here indicate that the damping solar radiation signal is phase shifted with respect to the SST anomaly, and in the case of tropical instability waves, at least, surface sensible and latent heat flux anomalies are also phase shifted (Thum et al., 2002). An imposed phase shift could be incorporated into the simple scenario described by Equation 5.8, but a more complete treatment would require modeling the coupled ocean-atmosphere boundary layers. Still, this simple model illustrates the potential for heat flux feedbacks on the oceanic mesoscale to cause horizontal eddy heat fluxes, and such an effect could prove important to the mean heat balance of climatically important regions such as the eastern Pacific warm pool and the equatorial cold tongue. A mechanism that may be similar to the one described here has been implicated in the warming of the equatorial cold tongue in the Pacific by tropical instability waves (Jochum et al., 2005).

Chapter 6

Conclusion

The research presented here has focused on the role of ocean dynamics (i.e. horizontal advection) in influencing SST and air-sea interaction, drawing on in situ observations from two contrasting sites and several satellite data products. This chapter presents a brief summary of the thesis and closes with a discussion of the lessons learned by the author in carrying out this research.

Summary

Using the in situ mooring data from 1997-1998 and satellite SST data, the temperature balance for the upper-layer (water above an isopycnal near the top of the pycnocline) was examined, and estimates were made of the terms representing surface heating, horizontal advection, and the rate of change of layer-averaged temperature. At the southern mooring site, the results showed that during the local onset of the equatorial cold tongue at the end of the 1997-1998 El Niño event (May-July 1998), cooling by horizontal advection, mostly due to wind-driven meridional flow, was partially compensated by increased surface heating. The residual (which could include contributions from mixing, entrainment, stratified dynamics, and possibly also from horizontal eddy-flux divergence), was also an important cooling influence during this transition, particulary during later stages (July-August 1998) as the main thermocline shoaled to 30-40 m depth.

At the northern site, a large ($\sim 0.035°$C/day amplitude), quasi-periodic signal was found in the rate of change of upper-layer temperature at intraseasonal periods (nominally 60 days) during about the first half of 1998. This signal was primarily a result of meridional

advection by the velocity signal associated with a passing Rossby wave. There was an apparently related signal in the surface heating term, but its contribution to the upper-layer temperature was smaller than the advective contribution. In addition, the intraseasonal signal in surface heating was phase-shifted by about 90° from the signal in the rate of change of upper-layer temperature. These facts suggested that the signal in surface heating was a response to the surface temperature variations driven by horizontal advection. A signal in surface latent and sensible heat fluxes resulting from variations in the surface temperature could be anticipated, since bulk formulas for these fluxes have a nearly linear dependence on SST (e.g., Haney, 1971). However, there was also a signal in surface solar radiation that was unanticipated and suggested a possible relationship between the Rossby-wave SST signal and atmospheric convection.

Additional attention was focused on the intraseasonal velocity signal at the northern site because of its importance in modulating SST and potential importance for mesoscale air-sea interaction. Previous work by others suggested that mesoscale intraseasonal variability is a prominent feature of the eastern Pacific warm pool region, and, although a number of hypotheses had been put forward for the existence of the variability, no consensus had been reached about the basic characteristics or generating mechanisms of the variability. An effort to develop a more comprehensive description of the intraseasonal variability on 10°N in the eastern tropical Pacific showed that the oscillations have zonal wavelengths of 550-1650 km and propagate westward in a manner consistent with the dispersion relation for first baroclinic mode, free Rossby waves in the presence of a mean westward flow. A novel technique for using observations to examine the potential for baroclinic instability showed that the oscillations likely draw energy from the North Equatorial Current. This mechanism helps to explain the annual cycle in the strength of the intraseasonal variability and the fact that the North Equatorial Current typically weakens between January and June, even as the wind continues to put energy into the current.

Having developed a more complete dynamical and statistical description of the mesoscale variability on 10°N in the eastern tropical Pacific, attention was focused on air-sea interaction associated with this variability. At the same zonal wavenumbers and frequencies associated with the mesoscale variability in meridional currents, a statistically significant relationship was detected between SST and some measures of cloud properties (specifically, cloud liquid water, its base-ten logarithm, and surface solar radiation). On average, the signal in cloud

properties was shifted slightly to the west (by 1-2° of longitude) of the SST signal, with more 'cloud' being found over warmer water.

While a few studies have identified systematic relationships between mesoscale oceanic variability and clouds (Deser et al., 1993; Hashizume et al., 2001; O'Neill et al., 2005), this is the first study to show a broadband coherence of SST and cloud properties in the wavenumber-frequency band corresponding to oceanic Rossby waves. Discussion focused on the interpretation of this relationship as an increased tendency for convection over warm mesoscale SST features (as opposed to over cool SST features) and on the variable factors that might influence the phase shift between SST and cloud properties. In an appendix, new hypothesis was presented for how such a systematic relationship between periodic mesoscale SST variability and surface heat fluxes might contribute significantly to time-mean horizontal heat fluxes in the upper-ocean. Besides having implications regarding the oceanic scales and dynamics that need to be resolved for realistic simulations of convective variability, the systematic air-sea interaction described here should motivate further study of oceanic mesoscale motions and their influence on SST and the overlying atmosphere.

Lessons learned

The final paragraphs of a Ph.D. thesis are an appropriate place to pause to retrospectively consider the lessons learned about the topic and techniques that have occupied the author for some number of years. These lessons are described below with an organization mimicking that of the thesis: lessons drawn from the temperature balance calculation (Chapter 3) are described first, those from the chapter on intraseasonal mesoscale variability on 10°N (Chapter 4) are described second, and those from the chapter dealing with the relationship between SST and cloud properties are described last. These "lessons" include facts about the ocean-atmosphere system and analysis techniques that are not widely appreciated, facts that may be widely appreciated but have only recently been appreciated by the author, limitations of the methods applied in this thesis, and possible implications of this work.

Specific lessons learned in carrying out the temperature balance computation involved the importance of meridional velocity variability, acting along the mean surface temperature gradient, in modifying the local surface temperature. At the southern site, meridional advection was important in the local onset of the equatorial cold tongue (or, transition to

La Niña conditions), and the observed vertically averaged meridional velocity was consistent with classical Ekman flow. At the northern site, meridional advection played a dominant role in producing the largest rate of change of upper-ocean temperature (on timescales exceeding three weeks) and the meridional velocity signal was due to mesoscale oceanic Rossby waves. Variability in the surface heat fluxes at similar timescales was also present but was of secondary importance in setting upper-ocean temperature. The relative importance of meridional advection over zonal advection might be viewed as a simple consequence of the fact that, on average, the meridional temperature gradient is much larger than the zonal temperature gradient.

A more general lesson from this calculation, noted previously by others for this region (e.g., Kessler et al., 1998), is that all of the terms (horizontal advection, surface fluxes, and the residual that represents mixing, entrainment, stratified dynamics, and may include a contribution from horizontal eddy-flux divergence) are important some of the time in setting the rate of change of the layer-averaged temperature. Contributions to these terms come from varied types of dynamics including modes of oceanic variability spanning scales from mm (e.g., turbulent mixing) to thousands of km (e.g., baroclinic Rossby waves, the equatorial current system, and atmospheric waves), and this range of scales and the temporal variations in the importance and intensity of these dynamics pose a challenge to simulation and prediction of SST.

A procedural lesson from the temperature balance computation is that the way the calculation is carried out has a qualitative effect on the nature of the inferred balance and the accuracy of the result. Although not a major focus of this thesis, the qualitative nature of the balance of terms in the temperature balance is affected by the choice of a boundary for the vertical integration. This should not be surprising (and is made mathematically explicit in Equation 3.3) since the action of the surface fluxes and subsurface turbulent fluxes and entrainment on the rate of change of layer-averaged temperature is much greater when the layer under consideration is thin (because these terms are inversely proportional to the layer depth) whereas the horizontal advection term does not depend explicitly on the layer depth. Thus, choosing a deeper integration depth will tend to make horizontal advection seem more important.

More importantly, though, the errors in such a budget are sensitive to the choice of integration depth, in large part because the integration is carried out to a depth near the main

thermocline, where a small uncertainty in the depth (in this study, an isopycnal) can lead to a large uncertainty in the vertical averages. Thus, even with the accurate and well-resolved measurements from the PACS moorings (e.g., compare to Cronin and McPhaden, 1997; Wang and McPhaden, 1999, 2001), the time rate-of-change of the layer-averaged temperature is often indistinguishable from zero. Aside from this study, the author is unaware of any study that has explicitly accounted for this type of uncertainty in similar computations.

The energetic intraseasonal variability in meridional velocity at the northern site (Chapter 4) was a manifestation of variability that is prominent and commonly observed in the latitude band of 9-13°N in the eastern tropical Pacific. A number of mechanisms have been proposed for the existence of this variability, and it was argued here that the most often cited of the hypothesized mechanisms, in which the variability results from intraseasonal wind fluctuations at the eastern boundary (Giese et al., 1994), cannot explain the observed intensification of the variability in the North Equatorial Current (NEC) nor can it explain the presence of similar variability in GCM simulations forced by climatological winds. The analysis in Chapter 4 was published before this thesis was complete (Farrar and Weller, 2006), and, fortuitously, a paper presenting additional evidence against the wind-forcing hypothesis appeared in the same issue of that journal (Zamudio et al., 2006). In Chapter 4, some evidence was presented suggesting that baroclinic instability of the NEC contributes energy to the mesoscale intraseasonal disturbances after they are generated farther east by the wind or other mechanisms. There may be other mechanisms contributing to the mesoscale intraseasonal variabiltiy in the region and further study, perhaps using a numerical model, will be necessary to determine the relative contributions of the various hypothesized mechanisms.

Because oceanic mesoscale variability influences local SST by horizontal advection and, although not seen or emphasized here, possibly also by creating signals in entrainment and vertical mixing, mesoscale variability can be imprinted in atmospheric fields. Oceanic mesoscale signals in surface wind speed have been well documented (see references in Chapter 5), but the influence of oceanic mesoscale variability on atmospheric properties related to convection is less well studied. In Chapter 5, it was shown for the first time that there is a broadband signal in cloud liquid water that is coherent with mesoscale SST variability in the wavenumber and frequency bands corresponding to mesoscale velocity variability.

This result suggests two obvious directions for future research. First, it would of course be desirable to assess the geographical extent of this relationship, and data are available to

do this. A preliminary investigation of the relationship at other latitudes suggests that there may be a similar relationship at other latitudes where the background convective conditions are much different (e.g., 20°S), but the significance of these preliminary results is unknown. Second, the fact that signals induced by the mesoscale SST field are present in both surface winds and cloud liquid water strongly suggests that these atmospheric signals may both be part of a single phenomenon. Although the surface wind signal associated with mesoscale SST variability has been a subject of intense study, consensus has not been reached on the details of the mechanism connecting the SST field to the surface wind field. If the signals in cloud liquid water and other cloud-related properties are due to the same mechanism as the wind signal, considerable progress might be made by attempting to test extant or new hypotheses against observations of both wind and clouds. At the same time, establishing that the wind and cloud signals result from the same process may prove to be tantamount to verifying the mechanism for either of the signals individually.

It is the author's opinion that the most significant result of this research is the finding that rather modest oceanic mesoscale variability in SST ($O(0.5°C)$) can influence atmospheric deep convection, which is a driving force of the atmospheric general circulation. Because this is a novel finding, it is not yet clear whether the influence of mesoscale SST variability on atmospheric convection could have a net climatic impact. Given the inherent nonlinearity of precipitating deep convection, even a weak modulation by mesoscale SST variability could conceivably influence the mean state of the atmosphere. Most atmospheric general circulation models used for weather and climate prediction do not resolve mesoscale variations in SST, either because the models are run at too coarse a resolution or because the SST fields used to drive the models are too smooth (e.g., Maloney and Chelton, 2006). For example, the atmospheric reanalysis of the European Centre for Medium Range Weather Forecasts, known as "ERA40" (Uppala et al., 2005), uses a very smooth representation of the SST field (Figure 6-1, lower panel). Comparison to a more well-resolved (or less smooth) estimate of the SST field (Figure 6-1, upper panel) for the same time period (a week centered on July 3, 1998) shows very clearly that nearly all of the mesoscale SST variations addressed in Chapter 5 are absent in the SST field used for the reanalysis. Around the time period shown in Figure 6-1, which is during the local ITCZ season, the analysis in Chapter 5 (e.g., Figures 5-6 and 5-14) shows a local relationship between mesoscale SST variations and variations in CLW. In fact, the peak-to-peak variations in the spatially filtered CLW (Figure 5-14) are

MCSST (AVHRR)

ERA 40 SST ("NCEP 2D var")
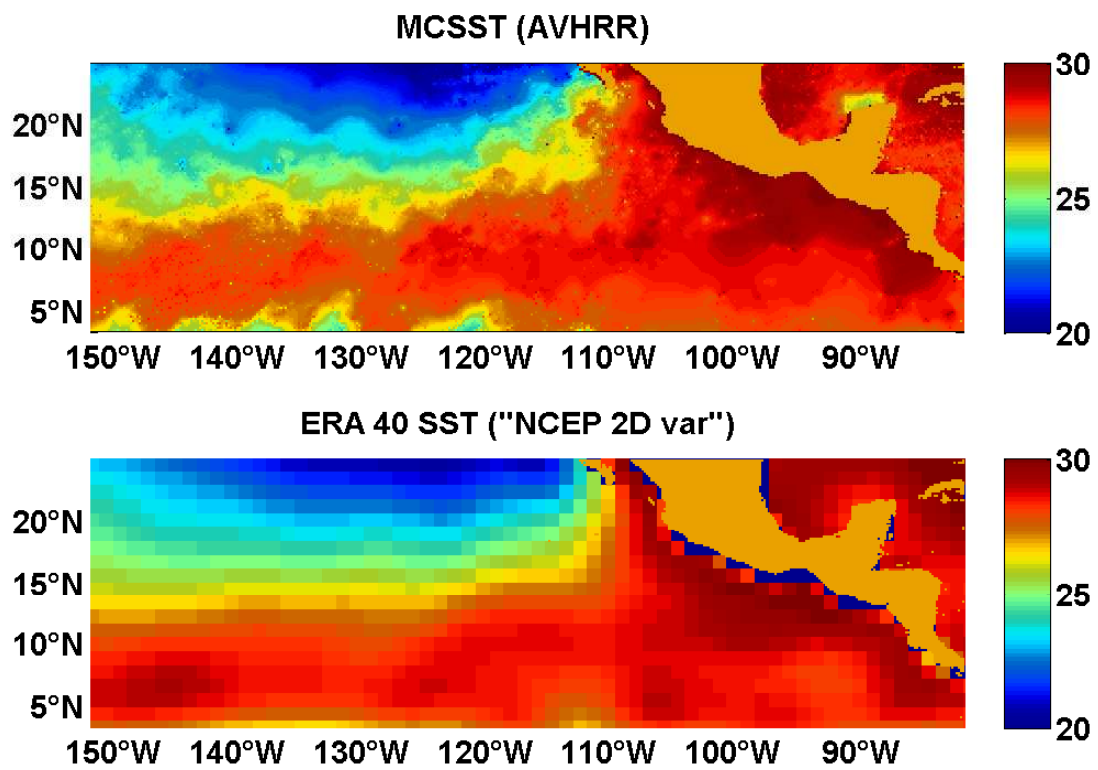
Figure 6-1: SST estimates for the week centered on July 3, 1998 from the U. Miami multi-channel SST estimate (Smith, 1992; upper panel) and from the field used in the ERA40 reanalysis (Fiorino, 2004; lower panel).

on the order of 50% of the total amount of 21-d averaged CLW during this time. To put it conservatively, these results suggest that the simulation of atmospheric convection could be improved by ensuring that the models and the SST fields that drive them adequately resolve the oceanic mesoscale.

Bibliography

[1] G. Alory and T. Delcroix. Interannual sea level changes and associated mass transports in the tropical Pacific from TOPEX/Poseidon data and linear model results (1964-1999). *J. Geophys. Res.*, 100:doi:10.1029/2001JC001067, 2002.

[2] S.P. Anderson, K. Huang, N.J. Brink, M.F. Baumgartner, and R.A. Weller. Pan American Climate Study data report. Technical report, Woods Hole Oceanographic Institution, 2000-03, Woods Hole, MA, 2000.

[3] D. Ballestero and J.E. Coen. Generation and propagation of anticyclonic rings in the Gulf of Papagayo. *Int. J. Remote Sensing*, 25:2217–2224, 2004.

[4] J.S. Bendat and A.G. Piersol. *Random Data: Analysis and measurement procedures.* Wiley-Interscience, New York, 1971.

[5] J.S. Bendat and A.G. Piersol. *Random Data: Analysis and measurement procedures (revised and expanded).* Wiley-Interscience, New York, 1986.

[6] J.S. Bendat and A.G. Piersol. *Atmospheric convection.* Oxford University Press, New York, 1994.

[7] A.K. Betts and W. Ridgway. Climatic equilibrium of the atmospheric convective boundary layer over a tropical ocean. *J. Atmos. Sci.*, 46:2621–2641, 1989.

[8] F. Bonjean and G.S.E. Lagerloef. Diagnostic model and analysis of the surface currents in the tropical Pacific Ocean. *J. Phys. Oceanogr.*, 32:2938–2954, 2002.

[9] C.S. Bretherton and A.H. Sobel. A simple model of a convectively coupled Walker circulation using the weak temperature gradient approximation. *J. Clim.*, 15:2907–2920, 2002.

[10] J.W. Brown, O.B. Brown, and R.H. Evans. Calibration of AVHRR infrared channels. *J. Geophys. Res.*, 98:18257–18268, 1993.

[11] M.A. Cane. A role for the tropical Pacific. *Science*, 282:59–60, 1998.

[12] C. Cassou and C. Perigaud. ENSO simulated by intermediate coupled models and evaluated with observations over 1970-98. Part II: role of off-equatorial ocean and meridional winds. *J. Climate*, 13:1635–1663, 2000.

[13] D.B. Chelton, R.A. DeSzoeke, M.G. Schlax, K. El Naggar, and N. Siwertz. Geographical variability of the first baroclinic Rossby radius of deformation. *J. Phys. Oceanogr.*, 28:433–460, 1998.

[14] D.B. Chelton, M.G. Schlax, M.H. Freilich, and R.F. Millif. Satellite measurements reveal persistent small-scale features in ocean winds. *Science*, 302:978–983, 2004.

[15] D.B. Chelton, M.G. Schlax, J.M. Lyman, and G.C. Johnson. Equatorially trapped Rossby waves in the presence of a meridionally sheared baroclinic flow in the Pacific Ocean. *Prog. Oceanogr.*, 56:323–380, 2003.

[16] M.F. Cronin and M.J. McPhaden. The upper ocean heat balance in the western equatorial Pacific warm pool during September-December 1992. *J. Geophys. Res.*, 102:8533–8553, 1997.

[17] M.F. Cronin, S.-P. Xie, and H. Hashizume. Barometric pressure variations associated with eastern tropical Pacific tropical instability waves. *J. Climate*, 16:3050–3057, 2003.

[18] C. Deser, J.J. Bates, and S. Wahl. The influence of sea surface temperature gradients on stratiform cloudiness along the equatorial front in the Pacific Ocean. *J. Climate*, 6:1172–1180, 1993.

[19] W.J. Emery. The role of vertical motion in the heat budget of the upper northeastern Pacific Ocean. *J. Phys. Oceanogr.*, 6:299–305, 1976.

[20] W.J. Emery and R.E. Thomson. *Data analysis methods in physical oceanography.* Elsevier, New York, NY, 1998.

[21] D.B. Enfield. The intraseasonal oscillation in eastern Pacific sea levels: How is it forced? *J. Phys. Oceanogr.*, 17:1860–1876, 1987.

[22] C.W. Fairall, E.F. Bradley, D.P. Rogers, J.B. Edson, and G.S. Young. Bulk parameterization of air-sea fluxes during TOGA COARE. *J. Geophys. Res.*, 101:3747–3764, 1996.

[23] C.W. Fairall, J.S. Bradley, E.F. Godfrey, G.A. Wick, J.B. Edson, and G.S. Young. The cool skin and warm layer in bulk flux calculations. *J. Geophys. Res.*, 101:1295–1308, 1996.

[24] J.T. Farrar. The evolution of upper ocean thermal structure at 10°N, 125°W during 1997-1998. Master's thesis, Massachusetts Institute of Technology, Cambridge, MA, 2003.

[25] J.T. Farrar and R.A. Weller. Intraseasonal variability near 10°N in the eastern tropical Pacific Ocean. *J. Geophys. Res.*, 111(C05015), 2006.

[26] M. Fiorino. A multi-decadal daily sea surface temperature and sea ice concentration data set for the ERA-40 reanalysis. Technical report, European Centre for Medium Range Weather Forecasts, ERA-40 Project Report Series No. 12, Reading, England, 2004.

[27] A.S. Fischer, R.A. Weller, D.L. Rudnick, C.C. Eriksen, C.M. Lee, K.H. Brink, C.A. Fox, and R.R. Leben. Mesoscale eddies, coastal upwelling, and the upper-ocean heat budget in the Arabian Sea. *Deep-Sea Res. II*, 49:2231–2264, 2002.

[28] N.P. Fofonoff. The Gulf Stream system. In B.A. Warren and C. Wunsch, editors, *The Evolution of Physical Oceanography*, pages 112–139. The MIT Press, Cambridge, MA, 1981.

[29] P. Gent and M.A. Cane. A reduced gravity, primitive equation model of the upper equatorial ocean. *J. Comput. Phys.*, 81:444–480, 1989.

[30] B.S. Giese, J.A. Carton, and L.J. Holl. Sea level variability in the eastern tropical Pacific as observed by TOPEX and the Tropical Ocean-Global Atmosphere Tropical Atmosphere-Ocean Experiment. *J. Geophys. Res.*, 99:24,739–24,748, 1994.

[31] A. E. Gill. *Atmosphere - Ocean Dynamics*. Academic Press, San Diego, California, 1982.

[32] A. Gonzalez-Silvera, E. Santamaria-del Angel, R. Millán-Nuñez, and H. Manzo-Monroy. Satellite observations of mesoscale eddies in the Gulfs of Tehuantepec and Papagayo (eastern tropical Pacific). *Deep Sea Res.*, 2004.

[33] R. L. Haney. Surface thermal boundary condition for ocean circulation models. *J. Phys. Oceanogr.*, 1:241–248, 1971.

[34] D.V. Hansen and G.A. Maul. Anticyclonic current rings in the eastern tropical Pacific Ocean. *J. Geophys. Res.*, 96:6965–6979, 1991.

[35] H. Hashizume, S.-P. Xie, T.W. Liu, and K. Takeuchi. Local and remote atmospheric response to tropical instability waves: a global view from space. *J. Geophys. Res.*, 106:10173–10185, 2001.

[36] S.P. Hayes, M.J. McPhaden, and J.M. Wallace. The influence of sea surface temperature on surface wind in the eastern equatorial Pacific: weekly to monthly variability. *J. Climate*, 2:1500, 1989.

[37] S. Hellerman and M. Rosenstein. Normal monthly wind stress over the world ocean with error estimates. *J. Phys. Oceanogr.*, 13:1093, 1983.

[38] K.L. Hill, S. Robinson, and P. Cipollini. Propagation characteristics of extratropical planetary waves observed in the ASTR global sea surface temperature record. *J. Geophys. Res.*, 105:21,927–21,945, 2000.

[39] X. Hong, S.W. Chang, S. Raman, L.K. Shay, and R. Hodur. The interaction between Hurricane Opal (1995) and a warm core ring in the Gulf of Mexico. *Mon. Wea. Rev.*, 128:1347–1365, 2000.

[40] D.S. Hosom, R.A. Weller, R.E. Payne, and K.E. Prada. The IMET (Improved Meteorology) ship and buoy systems. *J. Atmos. Oceanic Technol.*, 12:527–540, 1995.

[41] M. Jochum and P. Malonette-Rizzoli. On the generation of North Brazil Current rings. *J. Marine Res.*, 61:147–173, 2003.

[42] M. Jochum and R. Murtugudde. Internal variability of the tropical Pacific Ocean. *Geophys. Res. Lett.*, 31:L14309, doi:10.1029/2004GL020488, 2004.

[43] M. Jochum, R. Murtugudde, R. Ferrari, and P. Malonette-Rizzoli. The impact of horizontal resolution on the tropical heat budget in an Atlantic Ocean model. *J. Climate*, 18:841–851, 2005.

[44] M. Kanamitsu, W. Ebisuzaki, J. Woolen, S.-K. Yang, J.J. Hnilo, M. Fiorino, and G.L. Potter. NCEP-DOE AMIP-II reanalysis (R-2). *Bull. Amer. Met. Soc.*, 83:1631–1643, 2002.

[45] J. Kaplan and M. DeMaria. Large-scale charcteristics of rapidly intensifying tropical cyclones in the North Atlantic basin. *Wea. Forecasting*, 18:1093–1108, 2003.

[46] W.S. Kessler. Observations of long Rossby waves in the northern tropical Pacific. *J. Geophys. Res.*, 95:5183–5217, 1990.

[47] W.S. Kessler. Mean three-dimensional circulation in the northeast tropical Pacific. *J. Phys. Oceanogr.*, 32:2457–2471, 2002.

[48] W.S. Kessler, M.J. McPhaden, and K.M. Weickmann. Forcing of intraseasonal Kelvin waves in the equatorial Pacific. *J. Geophys. Res.*, 100:10613–10631, 1995.

[49] W.S. Kessler, L.M. Rothstein, and D. Chen. The annual cycle of SST in the eastern tropical Pacific, diagnosed in an ocean GCM. *J. Climate*, 11:777–799, 1998.

[50] C. Kummerow, W. Barnes, T. Kozu, J. Shiue, and J. Simpson. The Tropical Rainfall Measuring Mission sensor package. *J. Atmos. Oceanis Technol.*, 15:–817, 1998.

[51] O. Leeuwenburgh and D. Stammer. The effect of ocean currents on sea surface temperature anomalies. *J. Phys. Oceanogr.*, 31:2340–2358, 2001.

[52] S. Levitus and T. Boyer. Temperature. In *World Ocean Atlas 1994 Volume 4*. NOAA Atlas NESDIS 4, U.S. Department of Commerce, Washington, D.C., 1994.

[53] S. Levitus, G.I. Monterey, and T. Boyer. Seasonal variability of dynamic height and its fourier analysis. In *World Ocean Atlas 1994*. NOAA NESDIS Atlas 15, U.S. Gov. Printing Office, Washington, D.C., 1997.

[54] C.E. Lietzke, C. Deser, and T.H. Vonder Haar. Evolutionary structure of the eastern Pacific double ITCZ based on satellite moisture profile retrievals. *J. Climate*, 14:743–751, 2001.

[55] R.S. Lindzen and S. Nigam. On the role of sea surface temperature gradients in forcing low-level winds and convergence in the tropics. *J. Atmos. Sci.*, 44:2418–2436, 1987.

[56] E.D. Maloney and D.B. Chelton. An assessment of the sea surface temperature influence on surface wind stress in numerical weather prediction and climate models. *J. Climate*, 19:2743–2762, 2006.

[57] E.D. Maloney and J.T. Kiehl. MJO-related SST variations over the tropical eastern Pacific during the northern hemisphere summer. *J. Climate*, 15:675–689, 2002.

[58] S. Masina, S.G.H. Philander, and A.B.G. Bush. An analysis of tropical instability waves in a numerical model of the Pacific Ocean. *J. Geophys. Res.*, 104:29,637–29,661, 1999.

[59] T. Matsura and T. Yamagata. On the evolution of nonlinear planetery eddies larger than the radius of deformation. *J. Phys. Oceanogr.*, 12:440–456, 1982.

[60] J.P. McCreary, H.S. Lee, and D.B. Enfield. The response of the coastal ocean to strong offshore winds: with application to the Gulfs of Tehuantepec and Papagayo. *J. Mar. Res.*, 47:81–109, 1989.

[61] M.J. McPhaden. Variability in the central equatorial Indian Ocean, part II: oceanic heat and turbulent energy balances. *J. Mar. Res.*, 40:403–419, 1982.

[62] M.J. McPhaden. Monthly period oscillations in the Pacific North Equatorial Counter-current. *J. Geophys. Res.*, 101:6337–6359, 1996.

[63] M.J. McPhaden. Genisis and evolution of the 1997-98 El Niño. *Science*, 283:950–954, 1999.

[64] J.C. McWilliams and G.R. Flierl. On the evolution of isolated, nonlinear vortices. *J. Phys. Oceanogr.*, 9:1155–1182, 1979.

[65] C.S. Meinen and M.J. McPhaden. Interannual variabilty in warm water volume transports in the equatorial Pacific during 1993-99. *J. Phys. Oceanogr.*, 31:1324–1345, 2001.

[66] W.P. Menzel and J.F.W. Purdom. Introducing the GOES-I: the first of a new generation of Geostationary Operational Environmental Satellites. *Bull. Amer. Met. Soc.*, 75:757–781, 1994.

[67] J. Merle. Seasonal heat budget in the equatorial Atlantic Ocean. *J. Phys. Oceanogr.*, 10:464–469, 1980.

[68] L. Miller, D.R. Watts, and M. Wimbush. Oscillations of dynamic topography in the eastern Pacific. *J. Phys. Oceanogr.*, 15:1759–1770, 1985.

[69] J.R. Moisan and P.P. Niiler. The seasonal heat budget of the north Pacific: net heat fluxes and heat storage rates (1950-1990). *J. Phys. Oceanogr.*, 28:401–421, 1998.

[70] J. Molinari, D. Vollaro, S. Skubis, and M. Dickinson. Origins and mechanisms of eastern Pacific tropical cyclogenesis: a case study. *Mon. Wea. Rev.*, 128:125–139, 2000.

[71] D.L. Montroy. Linear relationship of central and eastern North American precipitation to tropical Pacific sea surface temperature anomalies. *J. Climate.*, 10:541–558, 1997.

[72] D.W. Moore and S.G.H. Philander. Modelling the tropical ocean circulation. In E.D. Goldberg et al., editor, *The Sea*, pages 319–361. Wiley-Interscience, 1977.

[73] F.E. Muller-Karger and C. Fuentes-Yaco. Characteristics of wind-generated rings in the eastern tropical Pacific Ocean. *J. Geophys. Res.*, 105:1271–1284, 2000.

[74] P.P. Niiler and J.W. Stevenson. The heat budget of tropical ocean warm water pools. *J. Mar. Res.*, 40:465–480, 1982.

[75] J.C. Ohlmann. Ocean radiant heating in climate models. *J. Climate*, 16:1337–1351, 2003.

[76] L.W. O'Neill, D.B. Chelton, and S.K. Esbensen. Observations of SST-induced perturbations of the wind stress field over the Southern Ocean on seasonal timescales. *J. Climate*, 16:2340–2354, 2003.

[77] L.W. O'Neill, D.B. Chelton, S.K. Esbensen, and F.J. Wentz. High-resolution satellite measurements of the atmospheric boundary layer response to SST variations along the Agulhas Return Current. *J. Climate*, 18:2706–2723, 2005.

[78] W.M. Ostrom, B.S. Way, S.P. Anderson, B. Jones, E. Key, and G. Yuras. Pan American Climate Study, Mooring Recovery Cruise Report, *R/V Melville*, cruise number PACS03MV. Technical report, Woods Hole Oceanographic Institution, Technical Report 99-01, Woods Hole, MA, 1999.

[79] R.E. Payne. Albedo of the sea surface. *J. Atmos. Sci.*, 29:959–970, 1972.

[80] J. Pedlosky. *Geophysical Fluid Dynamics*. Springer-Verlag, New York, NY, 1987.

[81] J. Pedlosky. *Ocean circulation Theory*. Springer, New York, NY, 1998.

[82] J. Pedlosky and J. Thomson. Baroclinic instability of time-dependent currents. *J. Fluid Mech.*, 490:189–215, 2003.

[83] C. Perigaud. Sea level oscillations observed with Geosat along the two shear fronts of the North Equatorial Counter Current. *J. Geophys. Res.*, 95:7239–7248, 1990.

[84] C. Perigaud, C. Cassou, B. DeWitte, and L.-L. Fu. Using data and intermediate coupled models for seasonal-to-interannual forecasts. *Mon. Wea. Rev.*, 128:3026–3049, 2000.

[85] C. Perigaud, F. Melin, and C. Cassou. Enso simulated by intermediate coupled models and evaluated with observations over 1970-98. Part I: role of off-equatorial variability. *J. Climate*, 13:1605–1634, 2000.

[86] S.G.H. Philander. Instabilities of zonal equatorial currents. *J. Geophys. Res.*, 81:3725–3735, 1976.

[87] N.A. Phillips. A simple three-dimensional model for the study of large-scale extra tropical flow patterns. *J. Meteorol.*, 8:381–394, 1951.

[88] J. F. Price, C.N.K. Mooers, and J.C. Van Leer. Observation and simulation of strom-induced mixed-layer deepening. *J. Phys. Oceanogr.*, 8:582–599, 1978.

[89] C.S. Ramage and A.M. Hori. Meteorological aspects of El Niño. *Mon. Wea. Rev.*, 109:1827–1835, 1981.

[90] D.J. Raymond and coautohors. EPIC2001 and the coupled ocean-atmosphere system of the tropical east Pacific. *Bull. Amer. Meteor. Soc.*, 85:1341–1354, 2004.

[91] W.B. Rossow and Y.-C. Zhang. Calculation of surface and top of atmosphere radiative fluxes from physical quantities based on isccp data sets: 2. validation and first results. *J. Geophys. Res.*, 100:1167–1197, 1995.

[92] M. Santamouris, G. Mihalakakou, Psiloglou, G. Eftaxias, and D.N. Asimakopoulos. Modeling the global solar radiation on the earth's surface using atmospheric deterministic and intelligent data-driven techniques. *J. Clim.*, 12:3105–3116, 1999.

[93] P.M. Saunders. The temperature at the ocean-air interface. *J. Atmos. Sci.*, 24:269–273, 1967.

[94] M.G. Schlax and D.B. Chelton. Aliased tidal errors in TOPEX/POSEIDON sea surface height data. *J. Geophys. Res.*, 99:24,761–24,775, 1994.

[95] L.K. Shay, G.J. Goni, and P.G. Black. Effects of a warm oceanic feature on Hurricane Opal. *Mon. Wea. Rev.*, 128:1366–1383, 2000.

[96] T. Shinoda and H.H. Hendon. Mixed layer modeling of intraseasonal variability in the tropical western Pacific and Indian Oceans. *J. Climate*, 11:2668–2685, 1998.

[97] T. Shinoda, H.H. Hendon, and J. Glick. Intraseasonal variability of surface fluxes and sea surface temperature in the tropical western Pacific and Indian Oceans. *J. Climate*, 11:1685–1702, 1998.

[98] J. Shukla. Predictability in the midst of chaos: A scientific basis for climate forecasting. *Science*, 282:728–730, 1998.

[99] R.J. Small, S. deSzoeke, S.-P. Xie, L. O'Neill, H. Seo, Q. Song, P. Cornillion, M. Spall, and S. Minobe. Air-sea interaction over ocean fronts and eddies. *Manuscript submitted to Dynam. Ocean. Atmos.*, 2006.

[100] R.J. Small, S.-P. Xie, and J. Hafner. Satellite observations of mesoscale ocean features and copropagating atmospheric surface fields in the tropical belt. *J. Geophys. Res.*, 110:doi:10.1029/2004JC002598, 2005.

[101] R.J. Small, S.-P. Xie, and Y. Wang. Numerical simulation of atmospheric response to Pacific tropical instability waves. *J. Clim.*, 16:3723–3741, 2003.

[102] E.A. Smith. A user's guide to the NOAA Advanced Very High Resolution Radiometer Multichannel Sea Surface Temperature (MCSST) data set produced by the University of Miami School of Marine and Atmospheric Science. Technical report, NASA Jet Propulsion Laboratory, 037-D001, Pasadena, CA, 1992.

[103] W.D. Smyth, D. Hebert, and J.N. Moum. Local ocean response to a multiphase westerly wind burst 2. thermal and freshwater responses. *J. Geophys. Res.*, 101:22513–22533, 1996.

[104] A.H. Sobel and C.S. Bretherton. Modeling tropical precipitation in a single column. *J. Clim.*, 13:4378–4392, 2000.

[105] A.H. Sobel and H. Gildor. A simple time-dependent model of SST hot spots. *J. Clim.*, 16:3978–3992, 2003.

[106] M.A. Spall. Mid-latitude wind stress/ sea surface temperature coupling in the vicinity of oceanic fronts. *Manuscript submitted to J. Clim.*, 2006.

[107] M.C. Spillane, D.B. Enfield, and J.S. Allen. Intraseasonal oscillations in sea level along the west coast of the Americas. *J. Phys. Oceanogr.*, 17:313–325, 1987.

[108] M.E. Stern. *Ocean Circulation Physics.* Academic Press, 1975.

[109] J.W. Stevenson and P.P. Niiler. Upper-ocean heat budget during the Hawaii-to-Tahiti Shuttle Eperiment. *J. Phys. Oceanogr.*, 13:1894–1907, 1983.

[110] H.G. Stumpf and R.V. Legeckis. Satellite observations of mesoscale eddy dynamics in the eastern tropical Pacific Ocean. *J. Phys. Oceanogr.*, 7:648–658, 1977.

[111] N. Thum, S.K. Esbensen, D.B. Chelton, and M.J. McPhaden. Air-sea heat exchange across the northern equatorial sea surface temperature front in the eastern tropical Pacific. *J. Climate*, 15:3361–3378, 2002.

[112] J.M. Toole, H.-M. Zhang, and M.J. Caruso. Time-dependent internal energy budgets of the tropical warm water pools. *J. Climate*, 17:1398–1410, 2004.

[113] C. Torrence and G.P. Compo. A practical guide to wavelet analysis. *Bull. Am. Met. Soc.*, 79:61–78, 1998.

[114] R.P. Trask, R.A. Weller, W.M. Ostrom, and B.S. Way. Pan American Climate Study, Mooring Recovery and Deployment Cruise Report, *R/V Thomas Thompson*, cruise number 73. Technical report, Woods Hole Oceanographic Institution, Technical Report 98-18, Woods Hole, MA, 1998.

[115] S. Umatani and T. Yamagata. Response of the eastern tropical Pacific to the meridional migration of the ITCZ: the generation of the Costa Rica Dome. *J. Phys. Oceanogr.*, 21:346–363, 1991.

[116] S.M. Uppala and coauthors. The ERA-40 re-analysis. *Q. J. Roy. Meteor. Soc.*, 131:2961–3012, 2005.

[117] W. Wang and M.J. McPhaden. The surface layer heat balance in the equatorial Pacific Ocean. Part I: mean seasonal cycle. *J. Phys. Oceanogr.*, 29:1812–1831, 1999.

[118] W. Wang and M.J. McPhaden. The surface layer heat balance in the equatorial Pacific Ocean. Part II: interannual variability. *J. Phys. Oceanogr.*, 30:2989–3008, 2000.

[119] W. Wang and M.J. McPhaden. The surface layer heat balance in the equatorial Pacific Ocean during the 1997-98 El Niño and 1998-99 La Niña. *J. Climate*, 14:3393–3407, 2001.

[120] B.S. Way, W.M. Ostrom, R.A. Weller, J.D. Ware, R.P. Trask, R. Cole, and J. Donovan. Pan American Climate Study, Mooring Deployment Cruise Report, *R/V Roger Revelle*, cruise number Genesis 4. Technical report, Woods Hole Oceanographic Institution, Technical Report 98-07, Woods Hole, MA, 1998.

[121] B.C. Weare. Interannual variation in net heating at the surface of the tropical Pacific Ocean. *J. Phys. Oceanogr.*, 13:873–885, 1983.

[122] P.D. Weidman, D.L. Mickler, B. Dayyani, and G.H. Born. Analysis of Legeckis eddies in the near-equatorial Pacific. *J. Geophys. Res.*, 104:7865–7887, 1999.

[123] M. Weinreb, M. Jamieson, N. Fulton, Y. Chen, J.X. Johnson, J. Bremer, C. Smith, and J. Baucom. Operational calibration of Geostationary Operational Environmental Satellite-8 and -9 imagers and sounders. *Applied Optics*, 36(27):6895–6904, 1997.

[124] R.A. Weller and S.P. Anderson. Surface meteorology and air-sea fluxes in the western equatorial Pacific warm pool during the TOGA Coupled Ocean-Atmosphere Response Experiment. *J. Climate*, 9:1959–1990, 1996.

[125] R.A. Weller, S.A. Baumgartner, S.A. Josey, A.S. Fischer, and J.C. Kindle. Atmospheric forcing in the Arabian Sea during 1994-1995: observations and comparisons with climatology and models. *Deep Sea Research II*, 45:1961–1999, 1998.

[126] R.A. Weller, F. Bradley, and R. Lukas. The interface or air-sea flux compontent of the TOGA Coupled Ocean-Atmosphere Response Experiment and its impact on subsequent air-sea interaction studies. *J. Atmos. Oceanic Technol.*, 21:223–257, 2004.

[127] R.A. Weller and R.E. Davis. A vector measuring current meter. *Deep Sea Res.*, 27, 1980.

[128] R.A. Weller, A.S. Fischer, D.L. Rudnick, C.C. Eriksen, T.D. Dickey, J. Marra, C.A. Fox, and R.R. Leben. Moored observations of upper-ocean response to monsoons in the Arabian Sea during 1994-1995. *Deep-Sea Res. II*, 49:2195–2230, 2002.

[129] F.J. Wentz. A well-calibrated ocean algorithm for special sensor microwave/imager. *J. Geophys. Res.*, 102:8703–8718, 1997.

[130] F.J. Wentz, C. Gentemann, D. Smith, and D. Chelton. Satellite measurements of sea surface temperature through clouds. *Science*, 288:847–850, 1999.

[131] F.J. Wentz and T. Meissner. Algorithm theoretical basis document, Version 2, AMSR ocean algorithm. Technical report, Remote Sensing Systems, 121599A-1, Santa Rosa, CA, 2000.

[132] C. Wunsch. The vertical partition of horizontal kinetic energy. *J. Phys. Oceanogr.*, 27:1770–1794, 1997.

[133] C. Wunsch. The work done by the wind on the oceanic general circulation. *J. Phys. Oceanogr.*, 28:2332–2340, 1998.

[134] K. Wyrtki. Fluctuations of the dynamic topography in the Pacific Ocean. *J. Phys. Oceanogr.*, 4:372–380, 1975.

[135] K. Wyrtki. Sea level during the 1972 El Niño. *J. Phys. Oceanogr.*, 7:779–787, 1977.

[136] K. Wyrtki. The response of sea surface topography during the 1976 El Niño. *J. Phys. Oceanogr.*, 9:1223–1231, 1979.

[137] S.-P. Xie. Satellite observations of cool ocean-atmosphere interaction. *Bull. Am. Met. Soc.*, 85:195–208, 2004.

[138] S.-P. Xie, M. Ishiwatari, H. Hashizume, and K. Takeuchi. Coupled ocean-atmosphere waves on the equatorial front. *Geophys. Res. Lett.*, 25:3863–3866, 1998.

[139] S.-P. Xie, H. Xu, W.S. Kessler, and M. Nonaka. Air-sea interaction over the eastern Pacific warm pool: gap winds, thermocline dome, and atmospheric convection. *J. Clim.*, 18:5–20, 2005.

[140] H.D. Young. *Statistical Treatment of Experimental Data*, chapter 13, pages 96–101. Waveland Press, Prospect Heights, IL, 1996.

[141] L. Zamudio, H.E. Hurlburt, J. Metzger, S.L. Morey, J.J. O'Brien, C. Tillburg, and J. Zavala-Hildago. Interannual variability of Tehuantepec eddies. *J. Geophys. Res.*, 111(C05001), 2006.

[142] X. Zang, L.-L. Fu, and C. Wunsch. Observed reflectivity of the western boundary of the equatorial Pacific Ocean. *J. Geophys. Res.*, 107, 2002.

[143] G.J. Zhang and M.J. McPhaden. The relationship between sea surface temperature and latent heat flux in the equatorial Pacific. *J. of Climate.*, 8:589–605, 1995.

[144] R. Zhang and S. Levitus. Interannual variability of the coupled tropical Pacific ocean-atmosphere system associated with the El Niño-Southern Oscillation. *J. of Climate.*, 10:1312–1330, 1997.

[145] Y.-C. Zhang, W.B. Rossow, and A.A. Lacis. Calculation of surface and top of atmosphere radiative fluxes from physical quantities based on ISCCP data sets, 1. Method and sensitivity to input data uncertainties. *J. Geophys. Res.*, 100:1149–1165, 1995.

[146] Y.-C. Zhang, W.B. Rossow, A.A. Lacis, V. Oinas, and M.I. Mischenko. Calculation of surface and top of atmosphere radiative fluxes from physical quantities based on ISCCP and other global data sets: refinement of the radiative transfer model and the input data. *J. Geophys. Res.*, 109:doi:10.1029/2003JD004457, 2004.

[147] V. Zhurbas and I.S. Oh. Drifter-derived maps of lateral diffusivity in the Pacific and Atlantic Oceans in relation to surface circulation patterns. *J. Geophys. Res.*, 109, 2004.